COLLOIDAL TRANSPORT AND ASSEMBLY UNDER ELECTRODIFFUSIOPHORESIS

By

Kun Wang

Dissertation

Submitted to the Faculty of the

Graduate School of Vanderbilt University

in partial fulfillment of the requirements

for the degree of

DOCTOR OF PHILOSOPHY

in

Chemical and Biomolecular Engineering

December 16th, 2023

Nashville, Tennessee

Approved:

Carlos A. Silvera Batista, Ph.D.

Kane Jennings, Ph.D.

Paul Laibinis, Ph.D.

Justus Ndukaife, Ph.D.

Dedication

To my mother (Hongyan Wang), and my father (Yingxiao Wang) who always love and support me.

ACKNOWLEDGMENTS

I would like to thank my advisor, Professor Carlos A. Silvera Batista. Dr. Silvera cares about all his students and respect us as independent researchers. Dr. Silvera is a pioneering leader in the field of colloidal electrokinetics. Dr. Silvera is an educator that always emphasizes the importance of diversity, equity, and inclusion. More importantly, Dr. Silvera is our mentor and provides an environment with encouragement and support. I am very happy and thankful that I have Dr. Silvera as my Ph.D. advisor. I also want to thank my committee, Professor Paul Laibinis, Professor Kane Jennings, and Professor Justus Ndukaife.

I would like to thank Behrouz Behdani, a good friend and lab mate who helped me not only in research but also in daily life. I want to thank Samuel Leville and Hannah Blake for their help with MATLAB coding and analysis. Lastly I would like to thank my Vanderbilt family for the love and support I received in the past 5 years: Zezhou Yang, Xiaomin Xu, Zhihao Shang, Xiaozong Fan, Ziqi Liu, Mario Ojeda Cuello, Dr. Vernon, Vivian Nwosu.

Chapter 2 is reprinted with permission from [Langmuir 2022, 38, 18, 5663–5673 Publication Date:April 25, 2022 https://doi.org/10.1021/acs.langmuir.2c00252]. Copyright [2022] American Chemical Society

Chapter 3 is reproduced from "K. Wang, S. Leville, B. Behdani, and C. A. Silvera Batista, "Long-range transport and directed assembly of charged colloids under aperiodic electrodiffusiophoresis.," Soft matter, vol. 18, no. 32, pp. 5949–5959, 2022" with permission from the Royal Society of Chemistry

TABLE OF CONTENTS

LIST OF FIGURES

CHAPTER 1

Introduction

1.1 Colloidal Assembly

1.1.1 Reconfigurable and Directed Assembly

Colloids are objects with size ranging from a few nanometers up to 10 microns. Two of the most commonly studied and used colloids are nanoscale and microscale droplets and particles. Colloidal objects are typically distributed throughout a liquid phase and this multiphase system is referred to as colloidal dispersions. Once dispersed in a liquid, an electric double layer (EDL) is formed near the particle's surface. The first layer is called the "Stern layer" which consists of immobile ions that are adsorbed onto the particle surface. The second layer is composed of ions that are attracted to the Stern layer and electrically screens the first layer. Unlike the Stern layer, the second layer is loosely associated with the particle's surface and can be dragged or deformed under external fields. This second layer is thus called the "diffuse layer". The EDL is not only important in terms of colloidal stability, but also in colloidal functionalization and assembly. Precise control over particle shape (15; 16), and colloidal forces (17; 18) has produced superlattices with sophisticated structures (19; 20; 21) in colloidal assembly. However, the traditional self-assembly of colloids has two major limitations. First, the static structures produced by the self-assembly process are hard to switch from one state to another. Second, the kinetic bottleneck may trap the assembly system far from the desired phase (22). To overcome the first limitation, an alternative approach called "reconfigurable assembly" which features a reversible transition between equilibrium states (23) was proposed. Colloidal reconfigurable assembly has been demonstrated in the forms of phase separation (24; 25), active colloidal molecules (26), and synchronization of large number of particles (27; 28). To bypass the kinetic bottleneck, directed assembly, which implies a form of control over the assembly process while still maintaining the advantages of self-assembly, can be applied. (29). For example, ac

electric fields can be applied to align the colloidal building block in diluted suspension. By taking this path before concentrating, the glassy arrest at higher volume fractions can be circumvented and the desired close packed crystals can be formed.

1.1.2 Tools for Reconfigurable Assembly

In principle, there are three major tools that can be exploited to control reconfigurable assembly of colloids: entropy, interaction potential and phoretic motion. Each are described below.

Reversible volumetric (30; 31), and shape change (32; 33) are good demonstrations of entropy-controlled reconfigurations. The changes in colloidal shape and size yield control in the number of available configurations in the system, which results in shift in system's phase boundaries. A phase transition may take place if this shift causes the system to move into a new region in the phase diagram. This phase transition is reconfigurable if the volumetric/size change of the building block is reversible. The expansion and contraction of colloidal volume change the lattice spacing in crystals, (Figure 1.1A) (1), while shape shifting of colloids induces reversible transitions between different crystal structures (1).

For charged colloids, the interaction potential can be adjusted by tuning the the Bjerrum length, the surface potential, and the Debye length (34). One way to control the interaction potential is through application of electric fields (35), as they induce dipolar interactions between polarizable colloidal particles. When isotropic particles are subjected to uniform electric fields, chain assembly (36) or colloidal crystals (37; 38) can be produced. For anisotropic colloids, the induced polar interactions can produce various assembly structures including staggered chains (39), chain-links (Fig.1.1B) (40), and sheets (41). For dielectric particles under high frequency ac electric fields, the dipolar interactions induce forces 5-10 times the thermal energy (38). These forces generate sheets and tubular structures (42).

Phoretic motion can be generated by transport phenomena like sedimentation, electrophoresis (EP) and diffusiophoresis (DP). These transport mechanisms can either exert forces directly on colloidal bodies (eg, sedimentation, radiation pressure, and dielec-

trophoresis) (34) or on EDL (eg, EP and DP) (43). EP acts that the application of electric field shears away the counterions in diffuse layer. This shear force leads to osmosis flow of liquid near the particle surface dragging particles moving towards the electrode of opposite charge (Figure 1.1C) (44). Dielectrophoresis (DEP) is present when a dielectric particle is subjected to a non-uniform electric field. Unlike EP, DEP does not require the colloidal particle to be charged. The non-uniform electric field polarizes the particle, and the induced poles experience a force which can be either attractive or repulsive depending on the orientation of the dipole. The orientation of the dipole is a function of the relative polarizability of the particle and medium. When the particle moves in the direction of higher electric field strength, the behavior is called positive DEP (pDEP). On the other hand, if particles move away from high field regions, the behavior is referred to as negative DEP (or nDEP). Since the relative polarizabilities of the particle and medium are dependent on frequencies, varying the signal frequencies can be an efficient way to control DEP forces. In contrast to EP and DP, which are induced by electric field, DP is the transport of colloids driven by a concentration gradient of solute (43). An example of the diffusiophoretic driven reconfigurable assembly is the segregation of platinum coated Janus particles. When dispersed in a fuel like hydrogen peroxide, the platinum side of the Janus particle catalyzes the decomposition reaction of the fuel giving rise to a concentration gradient. This induced concentration gradient drives particles active motion and ultimately causes particle segregation. (45).

1.1.3 Field Directed Assembly

To circumvent the kinetic bottleneck of colloidal self-assembly, external fields can be applied. These externally applied fields induce transport of colloidal particles and modulate interaction potential, driving colloids to the desired equilibrium phase. One of the most important fields to direct colloidal assembly are electric fields. Using electric fields has two major advantages. First, the electrochemical cell can be readily fabricated and modified by various techniques including thin film coatings, and lithographies (46). Second, the characterizing parameters of electric fields including magnitude, frequencies, waveforms

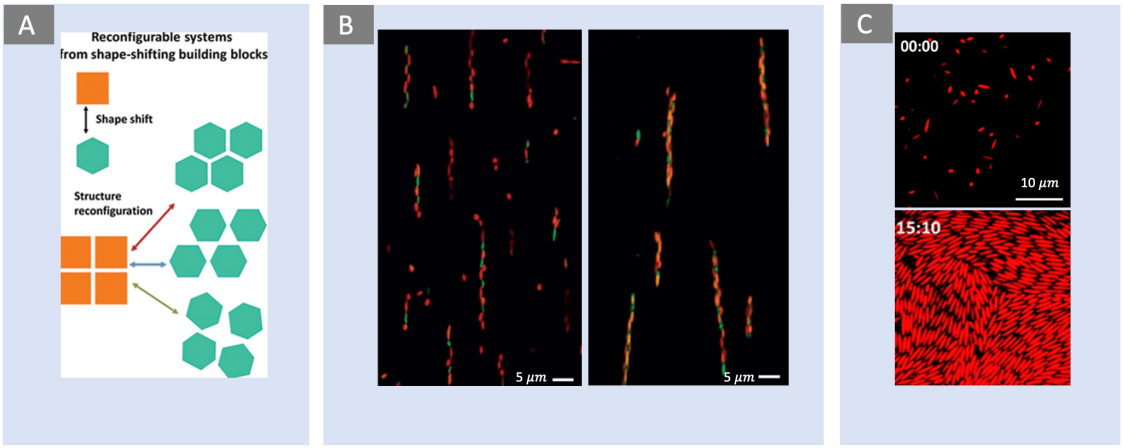

Figure 1.1: Classification of reconfigurable assembly by tools. (A) Entropy-induced reconfigurable assembly: particle shape variation generates reconfigurations from simple cubic (SC) to face centered cubic (FCC) crystals (1). (B) Interaction potential induced reconfigurable assembly: the length of Janus ellipsoid chains can be controlled by external ac electric fields (2). (C) Phoretic-induced reconfiguration: ellipsoids display a reversible order–disorder transition by light-assisted EP (3).

and phases allow a precise control over the forces exerted on the particle and the induced interparticle interactions. Depending on the frequencies of the applied fields, particles may present different assembly phases due to different responses to the applied fields, as in Figure 1.2.

When subjected to dc fields, charged particles experience EP, which drives them towards an oppositely charged electrode ultimately forming a deposition of particles. Once deposited on the electrode surface, the counterionic environment surrounding the particles disturbs the concentration polarization layer near the electrode surface. This disturbance results in electrohydrodynamic flows (EHD) around the particles that attract particles towards each other and form 2D crystals at the electrode surface (47; 48; 49). The 2D crystals can develop into 3D structures under EP deposition when the dc field strength increases. The formed 3D structures even appear in different colors based on the colloidal size (5). Under strong enough field, the deposition of particles can be permanently attached to the electrode surface. Barbee et al. reported a method of robustly binding protein-conjugated microbeads on electrode surfaces with the help of electrode-medium electrochemical reactions. The binded microbeads assemble into arrays on the electrode surface (50). By

introducing homogeneity on electrode surface, the unevenly distributed current densities on the electrode surface induces EHD flow towards the position where current density is higher. Rinstenpart et al. observed that particles accumulate around the scratches on the electrode surface which provides a possibility for guided assembly (4). The competition between EP and other phoretic motions like sedimentation provides a handle to control the speed of crystalline growth. Holgado et al. applied vertical dc fields in a cylinder with sedimenting spheres. The vertical electrophoretic mobility can add up to the Stokes sedimentation velocity to accelerate the growth of crystals. When the field direction is reversed, the electrophoretic mobility offset the sedimentation velocity. As a result, particles slowly assemble into ordered structures (51). Although EP has been used to form either 2D or 3D crystals after deposition, EP directed assembly has two major complications. First, the dielectric wall of devices almost always develops surface charges. These surface charges and associated conterionic double layer are attracted towards the oppositely charged electrode, dragging the liquid leading to electroosmotic flow. This electroosmotic flow drags the particles in random directions and may distort assembled structures. Another complication stems from the electrolysis of the medium. During the electrolysis, gas bubbles may be produced near the electrodes disturbing the colloidal assembly process. The application of ac fields (especially high frequencies) may prevent the above complications.

One of the most important tools of field directed assembly is DEP. Across different ac frequencies, DEP leads to different structures and can be used in distinct applications. At frequencies below 100 Hz, particles are patterned at the electrode surface in colloidal chains (6). At frequencies of 100-5000 Hz, gold nanoparticles have been reported to be assembled into microwires. The gold nanoparticles are attracted to the electrode edges where the field strength reaches its maximum. The attracted particles form porous cylindrical or semi-cylindrical structures with the length scale of a few micrometer diameters (8; 52). When the ac signal frequencies increase to 10^4- 10^5 Hz, colloidal particles display a transition from disordered monolayer to oriented monolayer to ordered 2D arrays (7). At frequencies

higher than 100k Hz, DEP can be used to separate streams of cells in flow-through devices. By precisely adjusting the frequencies, different types of cells can be efficiently seperated in the areas of minimum and maximum field strengths between electrodes (9).

In addition to DEP, the application of ac fields of different frequencies may induce other forms of manipulation of colloids. At low frequencies ($<$100 Hz), a long-range local electric field- asymmetric rectified electric field (AREF) will be induced provided that the ionic mobilities for cations and anions are unequal. AREF stems from the inharmonious oscillation of cations and anions. When the ac field is applied vertically, a force balance between AREF and gravity occurs promoting particles to levitate (53; 54). When two or more charged spherical particles are placed in an oscillating external electric field, the colloids will experience an induced polarization of their electric double layer, which induces positive or negative accumulation of charges on either side of the particle. In the case of identical colloids, whether the induced force is attractive or repulsive depends solely on the relative placement of the colloids with respect to the ac fields. When the particles are aligned parallel to the ac field, the partial positive accumulating charges will be attracted to the partial negative accumulating charges, thus, the induced dipole force is attractive. In contrast, when the particles are placed perpendicular to the applied field, the same particle charges on the neighbouring sides of the colloids result in a repulsion force. For systems with unlike particles, the attraction/repulsion determination can be complicated and depends on the zeta potential and the real part of the Clausius-Mossotti factor. Since the transition from repulsion and attraction is possible for binary particle systems, superlattice has been reported as in flower-like (3 kHz), triangle (10 kHz), and coloumnar structures (1 MHz) for particles placed align the electric field (11; 12).

In addition to electric fields, concentration gradients and the associated diffusiophoreis also haven shown great potential in directed assembly. One of the most studied topics is the self-propelled active colloids. Most active colloids require the synthesis of Janus particles having an asymmetric catalyst surface to generate a chemical gradient and propel the

colloids to migrate. However, a mixture of catalytic active and passive colloids may be a good alternative for self-propulsion. Yu et al. demonstrated that by mixing titanium dioxide colloids (catalytic active component) with silica particles (passive component), DP can be triggered under light illumination. The diffusiophoretic attraction between the two components leads to the formation of dimers. The self-propulsion of these dimers can be fully controlled by adjusting the illumination parameters (55). Additionally, externally applied chemical gradients can also be used in directed assembly. Ziemecka et al. demonstrated that a wave of propagating acids can cause the orientation and alignment of hydrogel fibers in a solution of dibenzoyl-L-cystine. Taking advantage of the known gelation of DBC below pH of 5, the hydrogel fibres can be assembled at the front of the acidic wave (56). Chiappisi et al. observed that nonconjugated π-donor π-acceptor monomer assemble into a rigid rods which is triggered by a NaCl gradient. The mechanical stiffness of these rods can be adjusted by controlling the local salt concentration (57).

Although the electric/chemical gradient directed assembly produces fruitful structures and phases, which have great potential in applications including polymeric porous membranes synthesis (56); biosensing (58) and consumer elecctronics (59), assembly solely triggered by electric fields is restricted by the cell geometry and mainly occurs on the electrode surface (50; 60; 61; 62). On the other hand, concentration gradient assisted assembly usually presents slower kinetics (56). In recent years, a new phoretic motion electrodiffusiophoresis (EDP) (which can be seen as the coupling of EP and DP) has attracted extensive attention since it may lead to assembly states that are not available in assembly systems directed by single field (63).

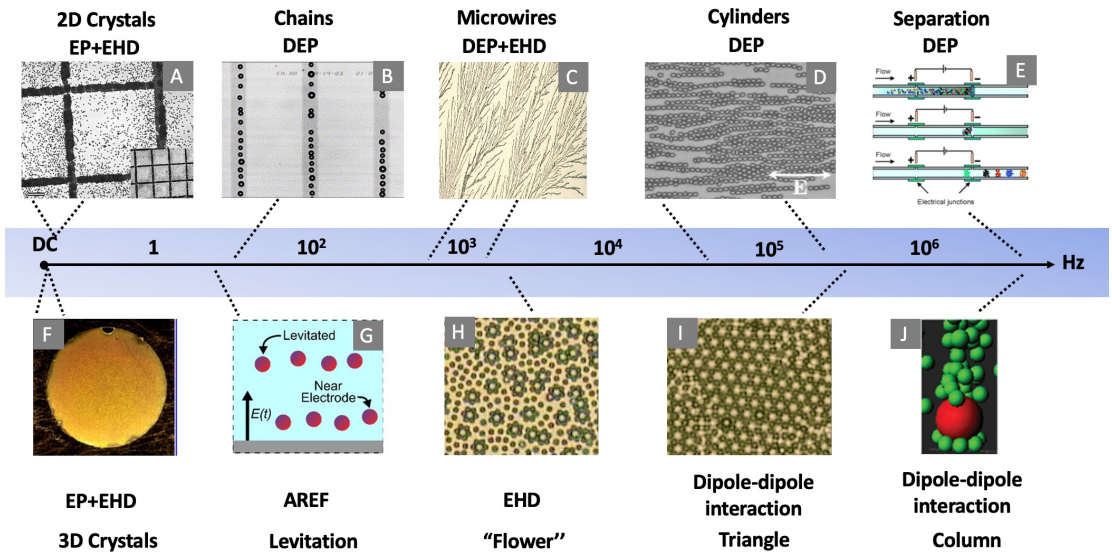

Figure 1.2: Summary of directed assembly induced by electric fields as a function of field frequencies. Under dc field, EP promotes particles to deposit on the oppositely charged surface and EHD attracts particles and assemble them into 2D (A), (4) and 3D (F), (5) crystals. Under ac field, DEP drives particles forming chains under low frequencies(B) (6), microwires (C) , (7) and cylinders (D), (8) at intermediate frequencies and can be used for bioseperations at really high frequencies. (E), (9). Besides DEP, ac fields can also induce AREF at really low frequencies, EHD at intermediate frequencies and dipole-dipole interactions at high frequencies. These mechanisms make particles levitate (G), (10), and form different superlattices (H-J), (11; 12).

1.2 EDP and its Potential in Particle Assembly

1.2.1 Theoretical Studies of EDP

The current density (i_d) in an electrochemical cell results from the convection, diffusion and electromigration of ionic species,

$$I_d = Fu\sum z_i n_i - F\sum z_i D_i \nabla n_i + \sigma \nabla \phi, \tag{1.1}$$

where F, u, ϕ and n_i are the Faraday constant, the fluid velocity, electrical potential and concentration of ions; z_i, D_i and σ are the valence, diffusivity of ionic species and conductivity, respectively (64). In the absence of chemical gradients and convection, the passage of an electrical current through a liquid electrolyte results in uniform electric fields ($E = -I_d/\sigma$) that drive the motion of charged particles under EP. The slip velocity for a thin double layer with small zeta potentials is given by the Smolowchowski equation

($V_{EP} = \frac{\varepsilon\zeta E}{\eta}$), in which the velocity of the particles (V_{EP}) is proportional to the zeta potential (ζ) and the electric field (E) (65; 66); η and ε are the viscosity and dielectric constant of the medium. On the other hand, even in the absence of a current, gradients of ionic species of different diffusivity produces an electric field whose magnitude is given by $\nabla\phi = E = -\frac{F}{\sigma}\sum z_i D_i \nabla n_i$. Charged particles respond to such electric field by moving up or down the chemical gradients under DP. In the case of a binary electrolyte and thin double layer, the slip velocity under DP (V_{DP}) is given by,

$$V_{DP} = \frac{3}{2} D_B \left[\tilde{\zeta}_p \beta + 4 \ln \left(cosh \frac{\tilde{\zeta}_p}{4} \right) \right] \nabla ln(n_0), \tag{1.2}$$

where $\tilde{\zeta}_p = (ze/k_b T)\zeta_p$ is the zeta potential scaled to the thermal voltage and $\beta = \frac{D^+ - D^-}{D^+ - D^-}$. D^+ and D^- are diffusivities of the positive and negative ions in the solution, and D_B is the diffusivity of a sphere with radius equal to the Bjerrum length (67; 68). The first term within brackets in eq 1.2 accounts for electrophoresis, whereas the second term is due to chemiphoresis. Ultimately, a charged particle can move up or down a gradient depending on the sign of $\tilde{\zeta}_p \beta$ and the magnitude of the chemiphoretic term. In the presence of direct (or alternating) currents and concentration gradients, a charged particle will experience a combination of electrophoresis and diffusiophoresis: electrodifussiophoresis (EDP).

There have been significant advances in the study of EDP, especially in theoretical fields (69; 70; 71). For example for a thin double layer colloidal particle in binary electrolyte under dc fields, the EDP velocity can be calculated as (63):

$$U_{EDP} = \left[U(\alpha + \beta)\tilde{\zeta}_p + 4 \ln \cosh \left(\frac{\tilde{\zeta}_p}{4} \right) \right] \left[\frac{12\tilde{C}_g + (9{\tilde{C}_g}^2 - 16)\tanh^{-1}\frac{3\tilde{C}_g}{4}}{9{\tilde{C}_g}^2} \right] \tag{1.3}$$

where $\tilde{C}_g = \frac{2ag_0}{C_0}$, $\alpha = \frac{(1-\beta^2)j_0}{2g_0 D_{eff}}$, $U = \frac{\varepsilon_r \varepsilon_0}{a\eta}\frac{k_B T}{ze}$,$\varepsilon_r\varepsilon_0$,$\eta$, k_BT, Z and e are the permittivity, viscosity, thermal energy, valence of ionic species, and electron charge; a is the particle radius; and $D_{eff} = \frac{2D^+ - D^-}{D^+ + D^-}$;$\tilde{\zeta}_p = \frac{ze}{k_B T}\zeta$ is the zeta potential scaled to the thermal voltage, j_0 is the current density (flux of ionic species), g_0 is the ion concentration gradient, and c_0 is the background concentration of ionic species.

Although extant theories describe EDP for a single particle under different conditions (69; 70; 71; 72), possibilities for fundamental contributions exist in the context of dynamic assembly and manipulation of colloids within electrochemical cell.

1.2.2 Potential of EDP in Colloidal Assembly

The coupling of electric field and concentration gradients may give rise to a closely related phenomenon -ion concentration polarization (ICP). ICP refers to a local redistribution of ions, with a region of depleted concentrations of ions (the ion depletion zone, IDZ) and another region of enriched concentration of ions (the ion enrichment zone, IEZ). This ion distribution can be achieved by either including a permselective membrane that transits only cations or by Faradaic reactions (FICP). Figure 1.3A shows a typical FICP setup in microfluidic channels with bipolar electrodes (BPE). During the continuous flow of solutions, a neutral species like water is reduced producing OH^- (red circle in Figure 1.3A) at the cathode. If the solution contains a buffer cation (blue circle), the produced OH^- will be neutralized, thereby forming an IDZ near the BPE cathode. The loss of ions in the IDZ increases the solution resistance, thus a corresponding electric field gradient will be generated. As a result of this local electric field gradient, colloids experience electromigration. Figure 1.3B shows how particles interact with opposing electromigration and flow convection in the microfluidic channel. At position A, the local electric field is at its peak, electromigration dominates convection, thus the negatively charged particle moves from left to right. When the particle reaches position B, the field strength decreases dramatically. Therefore there is an force balance between electromigration and convection, and the particle is focused at this position. If the particle should move to position C where the field strength is the lowest, then convection dominates and particle moves back to position B. Based on this scheme, (ICP) has been used in microfluidics to focus, sort, and concentrate synthetic colloids (73; 74; 75; 76; 77) as well as biomolecules, such as DNA and proteins (78; 79).

Recently, some studies have shown directly the potential of EDP in controlling parti-

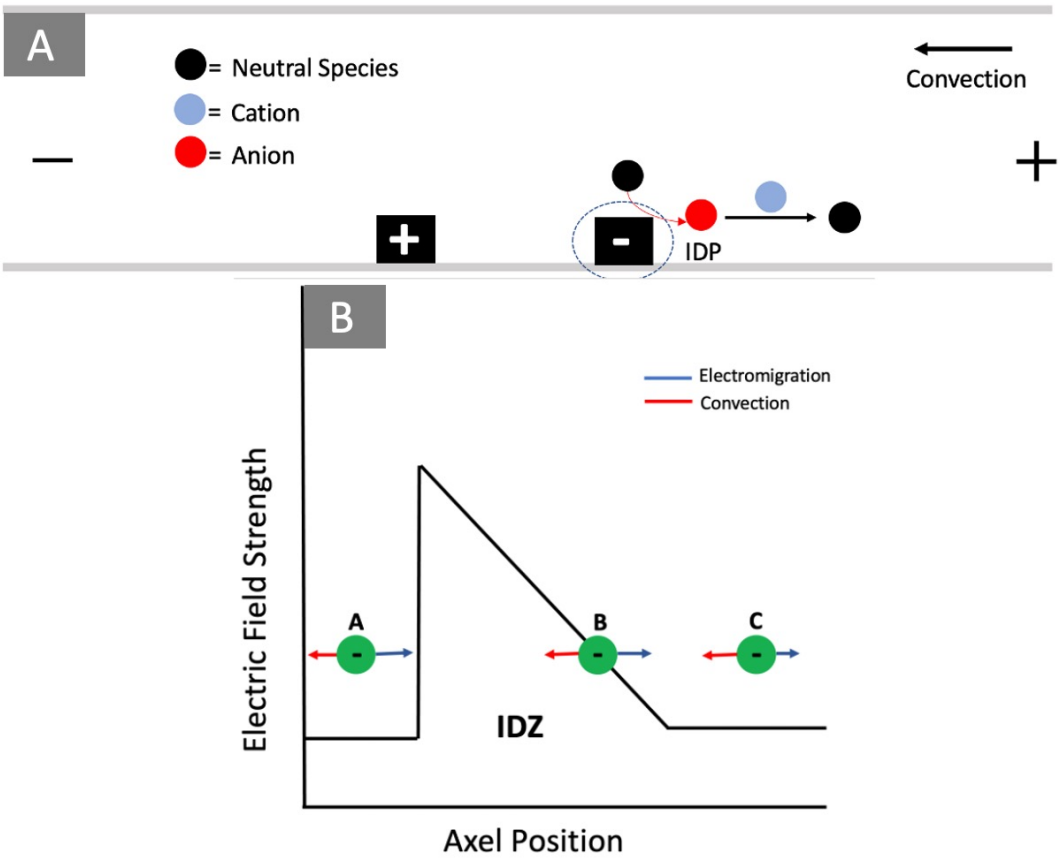

Figure 1.3: (A) Scheme of how the IDZ is formed near the BPE cathode in microfluidic channel. (B) The competition between convection and electromigration leads to particle's focusing at the IDZ.

cle's motion. In 2015, Sidelman et al. found that by dropping an aqueous liquid suspension between two circular gold electrodes, particles surprisingly accumulate near the surface of the cathode (Figure 1.4A). Preliminary qualitative analysis supported the author's hypothesis that accumulation of particles results from the applied dc fields and the pH gradients induced by electrolysis of water (13). In 2017, Silvera Batista et al. observed levitation of particles between two planar electrodes under dc fields (Figure 1.4B). Preliminary calculations based on eq 1.3 successfully predict the particle levitation. Based on that, the authors hypothesized that particles experience EDP because of the applied dc fields and the induced concentration gradients through electrolysis of DMSO (14).

Although the above studies suggest that EDP may result in unexpected particle motion that is normally not available under either EP or DP, there are important limitations in these

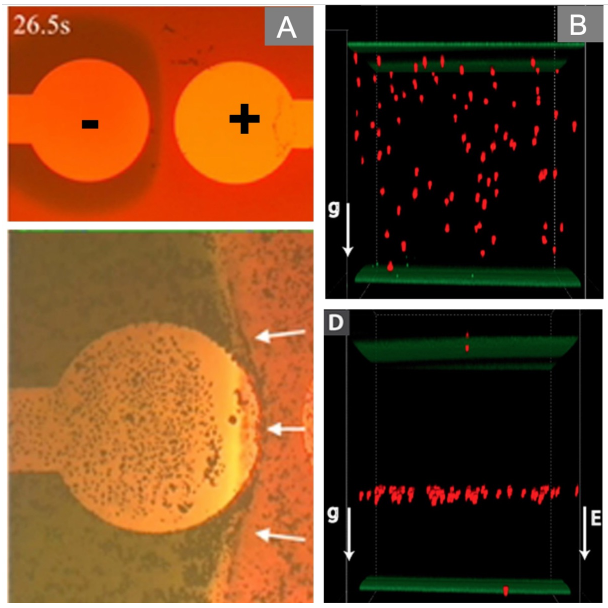

Figure 1.4: (A) Top: The formation of two pH zones at 2.0 V due to water electrolysis. A basic, green region is produced near the cathode and an acidic orange zone is observed near the anode. Bottom: Particles patterning near the pH transition zone as indicated by the white arrow (13). (B) Colloidal particles levitating between two plannar electrodes (green slabs) after only dc field is applied. Top row and bottom row show 3D confocal images of the device before and 60 s after the application of dc filed of 0.82 kV/m (14).

studies:

1. In both studies, direct quantitative evidence of the resulting concentration gradients was not provided. The authors of the first paper used a universal pH indicator which is only able to distinguish between acidic and basic conditions (Figure 1.4A) (13). The authors in the second paper did not provide mapping of the ionic concentration profiles due to complex reactions of the medium used (14). Since the concentration gradients cannot be mapped in both studies, the hypothesis could not be validated.

2. Prior studies mainly focus on EDP under dc fields, however, ac fields are more versatile in colloidal assembly due to the large number of adjustable parameters (eg, field amplitudes, phases, frequencies, and wave forms).

3. Recent studies mainly focus on studying particles electrokinetic response, the particle assembly under EDP is rarely discussed in literature.

Based on the above gaps of the literature in the field, the overall goal of this thesis includes:

1. Develop strategies to measure concentration gradients and study colloidal dynamics under EDP.

2. Using the developed strategies to study if concentration gradients are still produced under ac fields and how the particles respond to the aperodic EDP.

3. Investigate the assembly under EDP and understand the mechanical mechanisms of interparticle interactions.

1.3 Objectives and Outline

In this thesis, I studied the concentration gradients induced by both dc and ac electric fields and how the particles respond to the combination of electric fields and concentration gradients.

In Chapter 2, I report a strategy to quantitatively map the pH profiles induced by water electrolysis reactions. By using a ratiometric pH indicator, we are able to calculate the pH distribution accurately throughout the electrochemical cell. We then study the electokinetic response of collodial particles to the induced pH profiles through simultaneous visualization of both the ratiometric dye and particles using laser-scanning confocal microscope (LSCM). We discovered that particles migrate and focus at the position of maximum pH gradient. The results in Chapter 2 suggest that the induced pH profile governs the electrokinetic response of particles.

In Chapter 3, we study the particle's behavior under low frequency ac fields using the same strategy. A steep pH gradient can be produced even at low frequency ac fields and particles accumulate at the maximum pH position. I also performed a transport based simulation that supports the hypothesis that the pH gradient is produced from water electrolysis. Velocity calculations based on EDP theory agree with the experimental results, which provides further support for EDP as the dominant mechanism. I also observed that particles show an outstanding transition from disorder to ordered structures at the focusing position

In Chapter 4, we study the mechanism behind aggregation and assembly of particles. The results reveal that EDP at low frequency induces pairwise interparticle potential in the

scale of a few K_BT. More interestingly, the charged colloidal particles induce a local pH gradient surrounding the particle's surface giving rise to an EDP force in the XY plane. This EDP force determines the rate of assembly.

Finally, this dissertation concludes with a proposal of future directions based on the findings in Chapters 2-4.

CHAPTER 2

Visualization of Concentration Gradients and Colloidal Dynamics under Electrodiffusiophoresis

2.1 Abstract

In this chapter, I present a study of the dynamics of charged colloids under EDP at dc fields. The approach simultaneously visualizes the development of concentration polarization and the ensuing dynamics of charged colloids near electrodes. With the aid of confocal microscopy and fluorescent probes, I found that the passage of current through water confined between electrodes, separated about a hundred microns, results in significant pH gradients. Depending on the current density and initial conditions, steep pH gradients develop, thus becoming a significant factor in the behavior of charged colloids. Furthermore, I show that steep pH gradients induce the focusing of charged colloids away from both electrodes. The results provide the experimental basis for further development of models of electrodiffusiophoresis and the design of non-equilibrium strategies for materials fabrication.

2.2 Introduction

Gradients in electrical potential (electric fields), along with gradients in concentration of ionic species, are a principal way to control the motion of colloids. The surface and body forces (80; 81) that electric fields exert on anisotropic colloids have opened new applications in self-propulsion (81), transport of cargo (82), dynamic assembly (83), and directed assembly (5; 84). Similarly, DP —the motion of colloids induced by gradients of chemical species—has catalyzed the field of active colloids (85; 86) with profound implications in our understanding of the collective behavior of colloidal materials (24; 87; 88; 89; 90). More specifically, strategies involving chemical gradients currently underlie efforts to purify water (91; 92), separate colloidal particles (93), deliver drugs effectively (94), and improve flow through porous media (95; 96). In biology, concentration gradients determine

cellular communication, quorum sensing and chemotaxis (97; 98; 99; 100). Independently, motion via these two gradients, EP and DP, is well understood. However, motion generated from the combination of these two gradients is considerably less studied and offers another potentially useful mode of transport for the manipulation of colloidal systems (69; 70; 71).

Recently, pH gradients generated in the vicinity of planar electrodes led to the patterning of particles (13). Similarly, Silvera Batista et al. proposed EDP as the mechanism behind the levitation of charged colloids in DMSO (14). However, the use of DMSO as a medium imposed an important limitation due to its complex electrochemical behavior, and raised questions on the generality of the observed focusing phenomenon. Therefore, from an experimental point of view, the ability to visualize and quantify the gradients of electroactive species, as well as the ensuing response of charged particles, becomes a crucial element in the study of EDP.

As a medium, water offers the possibility to study many known electrochemical reactions. An interesting subset are those reactions that result in pH gradients due to the production or consumption of hydronium or hydroxide ions, such as the electrolysis of water. Monitoring products of electrochemical reactions or pH—simultaneously with the electrokinetic response of charged particles—requires high temporal and spatial resolution in systems with fast dynamics. In this sense, Laser Scanning Confocal Microscopy (LSCM) becomes a powerful tool. LSCM has enabled the visualization of electrochemical systems in-operando, to study mechanisms of reactions as well as transport phenomena (101; 102; 103; 104; 105). However, the fast scanning needed for high temporal resolution leads to low signal-to-noise ratios, complicating analysis, and the transition from visualization to quantification.

In this chapter, I present an experimental study of the dynamics of charged colloids under electrodiffusiophoresis. The approach relies on the ability to simultaneously visualize the development of concentration polarization (gradients of pH in this case) and the ensuing dynamics of charged particles through LSCM. Ratiometric analysis offers a reliable

strategy to map local pH with high spatiotemporal resolution by accounting for inherent variability in emission intensity, caused by scattering, probing depth, and photobleaching of fluorescent probes. We study the response of fluorescent particles with tunable surface charge, under different current density, initial pHs and concentration of background electrolyte. The results demonstrate that the passage of current through water confined between transparent electrodes, separated by ≈ 120 μm, results in significant pH gradients. These large gradients, I argue, alter the forces experienced by charged particles and induce their focusing away from both electrodes. Qualitative analysis, based on the theory of diffusiophoresis for multicomponent systems, offers insight into the origin of the forces leading to focusing. These results provide the experimental basis for the development of models of electrodiffusiophoresis that can enable the design of non-equilibrium strategies for materials fabrication.

2.3 Methods

2.3.1 Model Systems

The model systems used to study EDP were fluorescent polystyrene particles with carboxylate surface groups (CB-PS) and nominal diameter of 1.0 μm (Bangs Lab, FCGB006). All particles were initially dispersed in ultrapure deionized water (18 MΩ·cm) with a volume fraction of approximately 1×10^{-3} %. Measurements of ζ were performed in a Litesizer 500 (Anton Paar) through electrophoretic light scattering. The CB-PS particles were negatively charged, with an average zeta potential (ζ) of -46.8 ± 1.1 mV. To change the ζ, particles were modified by cross-linking PEG chains (Sigma Aldrich) of different molecular weights (5, 10, 20 and 30 kDa) to the carboxylate groups (PEG modified particles, PEG-PS), following the same procedure as in Reference 14. The attachment of PEG results in particles with less negative ζ, with the magnitude of the change modulated by the molecular weight of the PEG. For example, the ζ for the 30 kDa PEG-PS particles was -29 ± 1.1 mV in contrast to -43.2 ± 2.3 mV for 5 kDa PEG-PS particles.

2.3.2 Experimental Set-up

The electrochemical cells were built by confining $\approx 20\mu$L of suspension between two ITO-coated glass slides (SPI supplies, 70-100 Ω) that are separated by a dielectric spacer with nominal thickness of 120 μm (9 mm, Grace Biolabs, Cat. # 654002), as in Figure 2-1. The ITO coatings are positioned so as to be in contact with the water. The slides were cleaned by sequentially sonicating in acetone, isopropanol and DI water for 10 min in each solvent. Then, right before assembly of the devices, the slides were exposed to a UV-ozone treatment (UVO Cleaner Model 30, Jelight) for 5 min. The electric fields were applied by connecting the device to a potentiostat operated in galvanostatic mode. Current densities ranged from 0.15 to 4.5 A/m^2. Imaging of the particles and the concurrent pH gradients was performed using a Leica SP8 confocal laser scanning microscope (CLSM) with 40×, 1.10 NA, water immersion objective and the pinhole set to 1 Airy unit. Multi-channel detection enabled the simultaneous imaging of the emission from particles and pH indicator, as well as the reflection from the bottom and top electrodes. Nonetheless, reflection mode was mainly used to check the exact position of the electrodes. The optical properties of the particles and ratiometric dye (SNARF™-1) were selected so their emission did not overlap. The particles were excited at 405 nm and their emission was collected between 420 and 450 nm. A high-speed resonant scanner (8 kHz) enabled high acquisition rates of up to 28 frames per second, at 512×512 pixel resolution.

2.3.3 Measurements of pH While in Operation

5-(and-6)-carboxy SNARF™-1 is an organic molecule whose fluorescence emission changes from yellow-orange at acidic pHs to deep red at basic pHs (ThermoFisher, C1270). The ratiometric capabilities of SNARF stems from the different emission properties of the protonated and deprotonated species. Deprotonation of the phenolic substituent of SNARF-1 changes the emission from 583 nm to 627 nm, which enables the measurement of the relative concentration of the protonated and deprotonated species. In the ratiometric method, the pH of the medium is linked to the dissociation equilibrium of the dye—characterized

by the dissociation constant (pKa)—using the following formula:

$$\mathrm{pH} = \mathrm{pKa} - log\left(\frac{R_b - R}{R - R_a} \cdot \frac{I_{b,2}}{I_{a,2}}\right), \tag{2.1}$$

where R is the ratio of intensities at two detection points, I_1 and I_2, while R_b and R_a are the ratios of intensities at the basic (I_b) and acidic (I_a) end points. Using the ratio of signals at two different wavelengths, minimizes the effect of fluctuations in focus, excitation intensities and concentration of the dye. In my experiments, SNARF (100 μm) was excited at 514 nm, while the emission windows for I_1 and I_2 were centered at 580 nm and 640 nm. All the experiments were performed with the same settings, using a detection window of 5 nm for the two detectors. To determine the value of the pKa of carboxy SNARF-1 and the acidic and basic end points, I measured the ratio R at different pHs. The solution pH was ajusted by adding 0.01 M NaoH or HCl solution. For the calibration, I measured a value for the pKa of carboxy SNARF-1 similar to those reported by the vendor ($\approx$ 7.3), whereas the acidic and basic end points were measured at approximately pH 9 and 4, respectively. The measurements of pH in my experiments were performed within the limits of the end-points. Images were converted to pH maps using an algorithm developed in Igor Pro. The algorithm relies on the calibration data and Equation 2.1. Experiments with sodium fluorescein, another pH sensitive dye, followed a similar procedure as when using SNARF-1, with the necessary adjustments for excitation and emission wavelengths.

2.3.4 Analysis: Transient pH under dc Fields.

A simplified model provides insight into the pH profile within the cell. I solve the Poisson-Nernst-Planck equations in the liquid domain for the OH^-, H^+, and SNARF-1 species,

$$\partial n_i/\partial t + \nabla j_i = R_i, \tag{2.2}$$

$$j_i = -D_i \nabla n_i - n_i \mu_i \nabla \phi + n_i u, \tag{2.3}$$

with the mobilities given by the Einstein-Smoluchowski equation, $\mu_\pm = D_\pm ez/k_BT$. The model solves the transient equation for conservation of ionic species. Diffusion, migration,

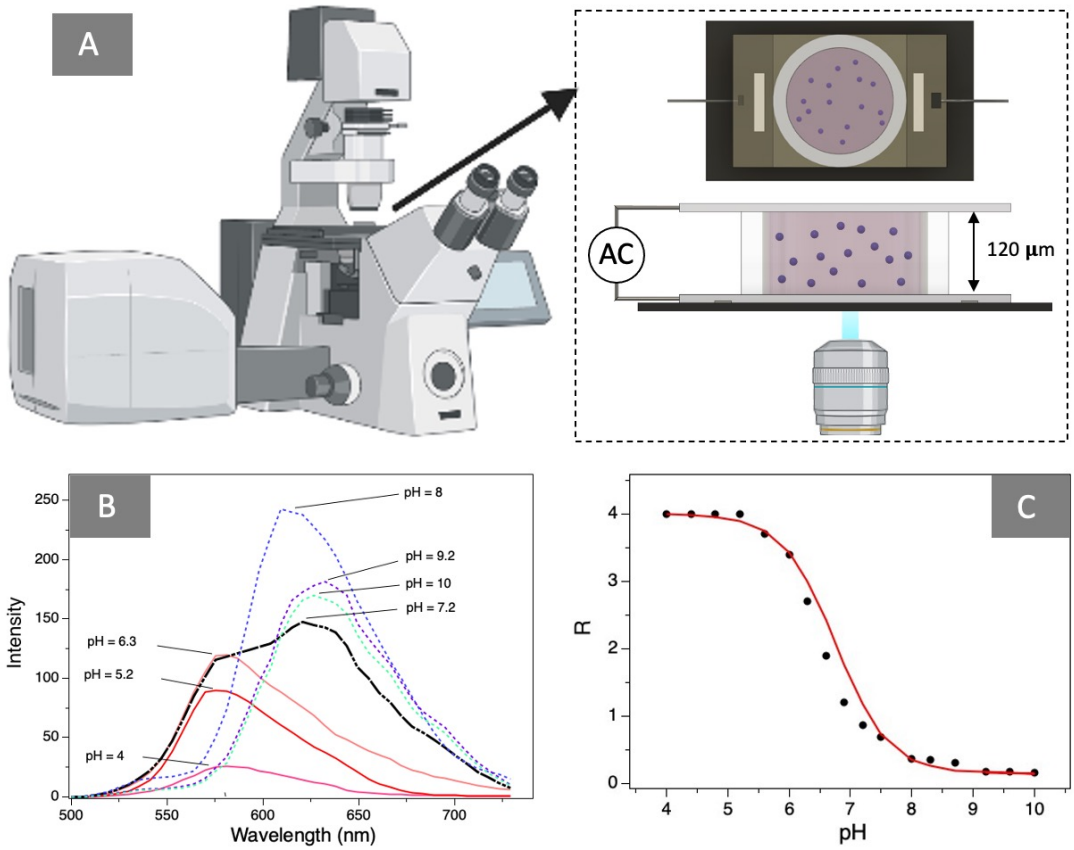

Figure 2.1: (A) Imaging the emission from SNARF-1 and fluorescent particles through confocal microscopy enables the simultaneous visualization of pH gradients and particle dynamics under dc fields. The device (electrochemical cell) consisted of two ITO slides separated by a dielectric spacer ($\approx 120\ \mu$m thick). Particles and SNARF-1 were excited at 405 nm and 514 nm, respectively. (B) Emission spectrum of SNARF-1 changes with pH; the graphs show the normalized emission intensity at different pH values. (C) Ratio R between emission at 580 and 640 nm decreases at higher pH; R provides the means to probe the pH in aqueous media.The red line represents the fit under the calibration equation

and convection determines the flux, j_i, of ionic species. The reaction term, R_i, accounts for the equilibrium reaction of water ($H_2O \rightleftharpoons OH^- + H^+$) and dissociation of SNARF ($HSNARF^{-1} \rightleftharpoons SNARF^{-2} + H^+$) within the liquid domain. The dissociation equilibrium of the SNARF molecules occurs between species holding either one or two net negative charges. The electroneutrality condition applies in the liquid domain because the size of the electrical double layer is of the order of tens of nanometers. As a first step, the model does not describe the electrode kinetics. Therefore, the exact potential drop at the electrode and, consequently, the potential within the electrolyte are not known. Instead of modeling the electrode kinetics, the voltage in the electrolyte is accounted as an externally imposed

parameter. Given the low conductivities in the experiments, it is necessary to include the migration term. On the other hand, constant fluxes at the boundaries account for the reactions at the electrodes. Water electrolysis constitutes the most dominant faradaic reaction in the system, which produces protons at the anode and hydroxyl ions at the cathode, when carried out at neutral pH values,

$$anode : 2H_2O \rightleftharpoons 4H^+ + O_2 + 4e^-, \tag{2.4}$$

$$cathode : 4H_2O + 4e^- \rightleftharpoons 4OH^- + 2H_2, \tag{2.5}$$

Therefore, the boundary conditions at the anode are: $j_{H^+} = I_d/F$ and $j_{OH^-} = 0$, while at the cathode, they are $j_{OH^-} = I_d/F$ and $j_{H^+} = 0$. Although it is not possible to keep current and potential constant in real experiments, this strategy provides approximations to the behavior of the system. The coupled equations were solved using the finite-element method as implemented in COMSOL Multiphysics, using the modules for the transport of dilute species and the tertiary current distribution.

2.4 Results and Discussion

2.4.1 Visualization of pH Gradients

The 3D confocal images in Figure 2.2A-C show the volume within the electrochemical cell before and after applying a current of 4.5 A/m^2 through an aqueous medium containing SNARF-1. The images show the view from the x-z plane of the volume between the electrodes. Although not shown, the electrodes are located immediately below and above the colored section, as illustrated in Figure 2.2D. The images combine the intensity collected at 580 nm (I_1, yellow) and at 640 nm (I_2, red). Initially, the color throughout the cell is uniform, indicating a constant pH at the value of ≈ 7.2. When the current is applied between the cathode (top electrode) and anode (bottom electrode) for 65 s, the ratio of intensity ($R = I_1/I_2$) from the two detection channels changes. The intensity collected at the red channel becomes much higher near the cathode ($R \approx 0.4$), while it decreases near the anode ($R \approx 2.6$), in comparison to an initial $R \approx 1$. The lower value of R near the

cathode indicates an increase in pH, while the opposite occurs near the anode. Analysis based on the calibration equation reveals the pH ranges from approximately 8.5 to 6.5. The system is dynamic since the zone of higher pH spans half the cell after 104 s. To summarize, the images demonstrate that significant and measurable pH gradients form within the electrochemical cell with the passage of current.

The qualitative results follow the trends expected from the electrolysis of water (Figure 2.2D). At the cathode, reduction of water occurs, resulting in the evolution of hydrogen and the formation of hydroxide ions. In contrast, at the anode, oxidation of water takes place, resulting in the evolution of oxygen and the formation of hydronium ions. Consequently, as the electrical current passes through the cell, the accumulation of hydroxide ions near the cathode and hydronium ions near the anode results in basic and acidic pHs, respectively. Experiments with another pH sensitive dye, fluorescein, also show two distinct zones, one where the emission is quenched (indicating lower pH) and another where the intensity increases (indicating higher pH). Although the pKa of SNARF-1 and fluorescein are different, the experimental results in Figure 2.2 and Figure A.1 in Appendix A suggest general features about the electrochemical behavior of the system.

2.4.2 Modulation of pH Gradients Through Current Density and Initial pH

Current density and initial pH are two readily available parameters to set the electrochemical conditions within the experimental cells. To better appreciate the evolution of the system, the first row in Figure 2.3 shows heat plots that condense the temporal and spatial distribution of pH during a single experiment, while the second row shows the pH profile for a single time (53 seconds), denoted by the black-dashed lines in the respective heat plot. The values of pH reported in the heat plots were calculated using calibration equation and the ratio of intensities from the two detection channels, after image analysis and processing of data through a routine in Igor Pro. The color scales in these plots range from bright red (pH 6) to bright blue (pH 9).

The panels in Figure 2.3 show the response of the system to different current densities

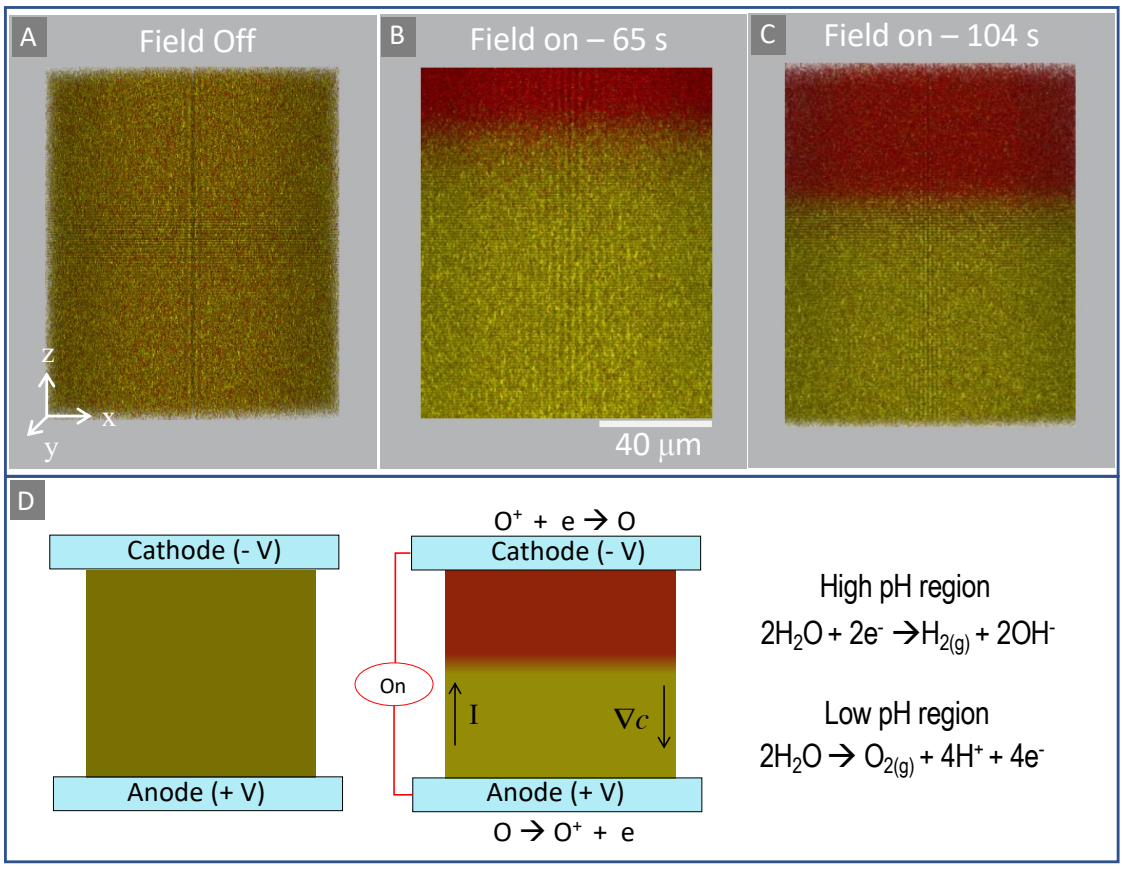

Figure 2.2: Imaging of the emission from SNARF-1 through confocal microscopy enables the visualization of pH gradients during electrolysis of water. (A-C) Confocal images of the volume between the electrodes before and after applying a current density of 4.5 A/m^2 for 65 and 104 seconds. (D) Schematic of the device (electrochemical cell) and accompanying reactions for a typical experiment. The reduction and oxidation of water leads to regions of higher and lower pH, respectively, in comparison to the initial value of ≈ 7.2. The images report volumes of cross section area equal to 106×106 μm^2, electrode gap of 120 μm and detection from two channels at 580 nm (yellow-orange) and 640 nm (red).

(0.15, 0.2, 0.5, 4.5 A/m^2). For the lowest current density (0.15 A/m^2), the map and profile at 53 seconds indicate the pH does not change significantly from the initial value (≈ 7.2) throughout an experiment. As the current density increases to 0.2 A/m^2 (Figure 2.3B,F), the pH remains relatively uniform during the first half of the experiment. However, after 53 s, the pH begins to increase rapidly near the cathode, and a clear region of basic pH develops, as evidenced by the light blue color. When 0.5 A/m^2 is applied, clear regions characterized by acidic and basic pHs develop soon after turning on the electric field (Figure 2.3C). The profile in Figure 2.3 G shows the pH decreases below 7 near the anode, but

it begins to increase slowly towards the cathode until there is a jump to values that plateau near 8. The process is dynamic; initially the basic region extents 50 μm into the cell, but it steadily decreases in size until becoming 20 μm in width, by the end of the experiment. At the current density of 4.5 A/m^2 (Figure 2.3D), the plot shows that two diffusion fronts, one acidic and the other basic, form from the anode and cathode, respectively. Interestingly, the position at which the two diffusion fronts meet results in a noticeable sudden change in pH that resembles a sigmoidal function (Fig 2.3H). These results demonstrate that, depending on the experimental parameters, significant concentration polarization occur within the whole electrochemical cell, not only close to the electrodes. It is important to notice that the Sigmoidal shape of the profile is not due to the limitations of the dye since the measured values were ensured to be safely between the acidic and basic endpoints. In addition

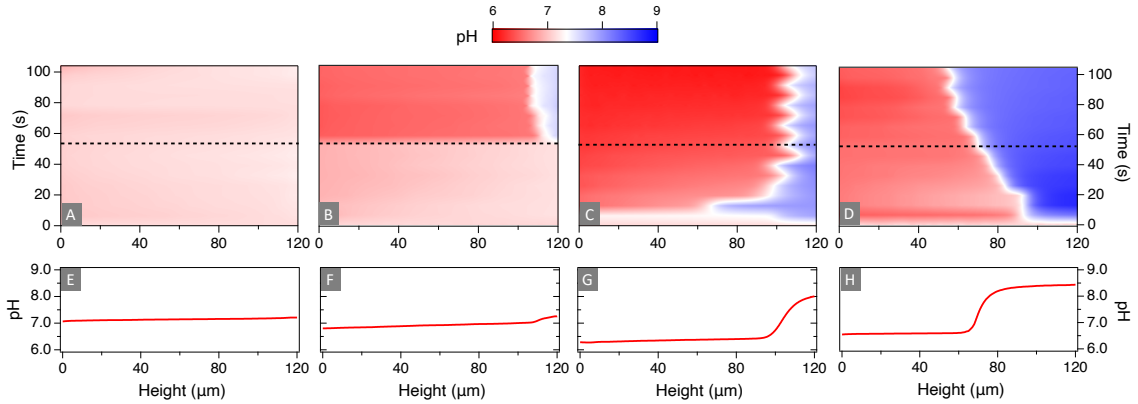

Figure 2.3: The value of current density impacts the observed pH profiles. Panels (A-D) are 2D heat maps that condense the pH profiles for all times in a single experiment, while panels (E-H) represent the pH profile for a single time (52 s), indicated by the dashed lines in panels A-D. The applied current densities were 0.15 (A,E), 0.2 (B,F), 0.5 (C,G) and 4.5 (D,H) A/m^2.

to current density, the formation of two distinct acidic and basic regions also depends on the starting pH of the solution (pH$_i$). While the maps for pH$_i$ 7.2 and 8.5 contain distinct regions of basic and acidic pHs, those for pH$_i$ 6.5 remain uniform throughout the experiments (Figure A.2-3 in Appendix A). Therefore, the trends in these experiments suggest the distinct regions of pH form more easily when the pH$_i$ is basic or close to neutral.

2.4.3 Response of Charged Particles under EDP

To study the behavior of charged particles under the generated electrochemical conditions, the fluorescence intensity from PEG-PS particles and from the SNARF-1 were recorded simultaneously, as a current density flows through the system. Particles were selected with emission and excitation that do not overlap with those of SNARF; therefore, the model system has an emission peak at 440 nm, with excitation at 405 nm. Experiments at different current densities illustrate the effect of pH gradients on the response of particles. Figure 2.4 compares maps of pH and fluorescence intensity from particles, for all times in a single experiment. The corresponding pH maps (Figures A.4-5 in Appendix A) resemble those already described in Figure 2.2, suggesting that at the low volume fraction used in these experiments, the pH profile is not significantly affected by the presence of the particles. However, the accumulation of particles does affect the emission from SNARF. For the maps describing the intensity from particles, the white color indicates the highest relative intensity—and consequently, concentration of particles—while the dark blue indicates the lowest relative intensity. At the lowest current density (0.15 A/m^2), the intensity from the particles progressively increases at the bottom, indicating unidirectional motion towards and accumulation at the anode. The profile in Figure 2.4C shows that, after 86 seconds, concentration of particles is 5$\times$ higher at the anode in comparison to the cathode.

The response of the particles under 4.5 A/m^2 is quite different; particles migrate away from both electrodes, and after 40 seconds, they focus in a narrow band (see intensity profile as well as the images in Figures 2.5B and D). Most importantly, comparing the pH and intensity maps (Figure 2.4) and the images (Figure 2.5), it is evident that particles accumulate exactly at the position where the steepest change in pH occurs. The peaks in the intensity maps trace the same trajectory as the boundary between the regions of basic and acidic pH. Also, particles move more easily down the gradient (from cathode to anode) than up the gradient (from anode to cathode). Consequently, the concentration of particles is usually higher near the anode. The data in Figure 2.4, and the corresponding

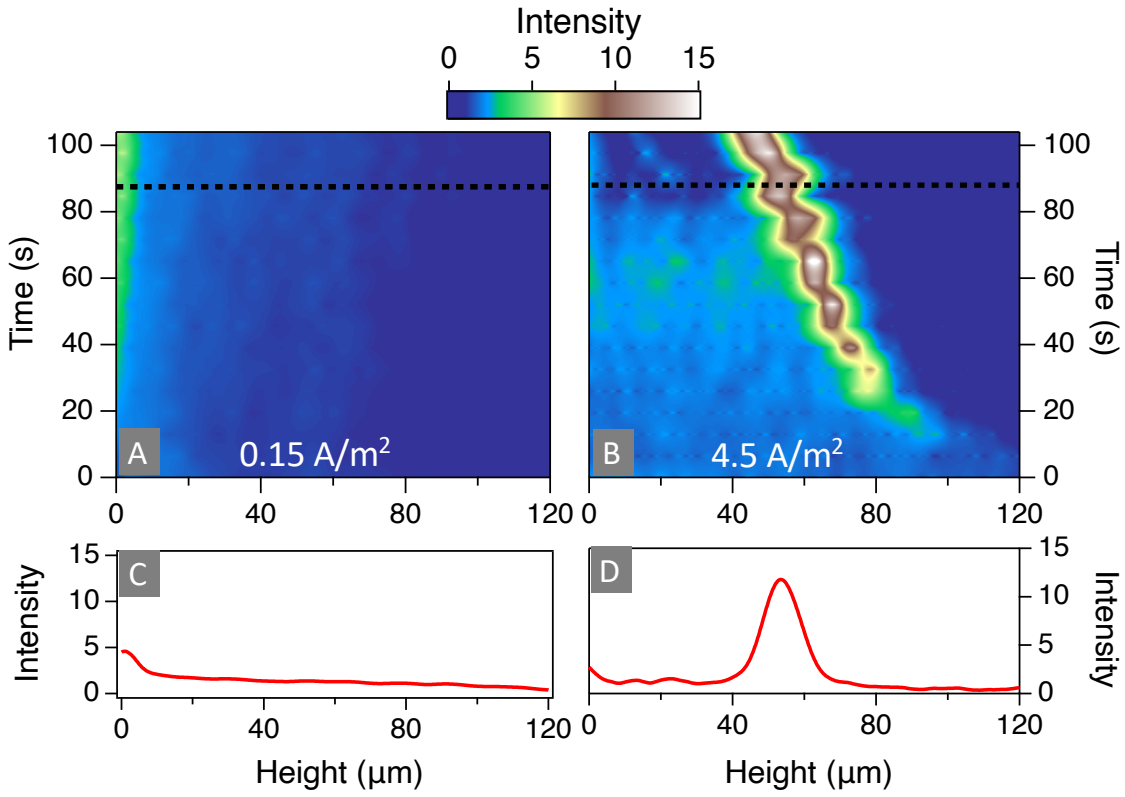

Figure 2.4: The current density and the accompanying pH gradients determine the response of charged particles. Panels (A-B) are 2D heat maps that condense the fluorescence intensity from the particles for all times in a single experiment, while Panels (C-D) represent the intensity profile for a single time (86 s). The applied currents were 0.15 (A,C) and 4.5 (B,D) A/m^2, while the average zeta potential of the particles (30 kDa PEG-PS) was -28.8 $\pm$ 1.0 mV.

images, suggest the focusing of particles results from the steep pH gradients produced by the electrolysis of water. Even at high currents, if a steep pH gradient does not form (see the case for pHi 6.5 in Appendix A Figure A.2), particles do not experience focusing. Focusing is generally observed when current densities above 0.9 A/m^2 are applied. Later, we will see that the presence of steep pH gradients is a necessary, but not a sufficient condition, to achieve significant accumulation of particles away from the electrodes. It is notable that the accumulation of particles does affect the emission from SNARF (Figure 2.5). Nonetheless, the ratiometric analysis accounts for those variations since it does not rely on absolute intensity to obtain local pH. These experiments show that particles respond appreciably to both the electric fields and the concentration gradients generated by the electrochemical reactions that sustain the passage of current.

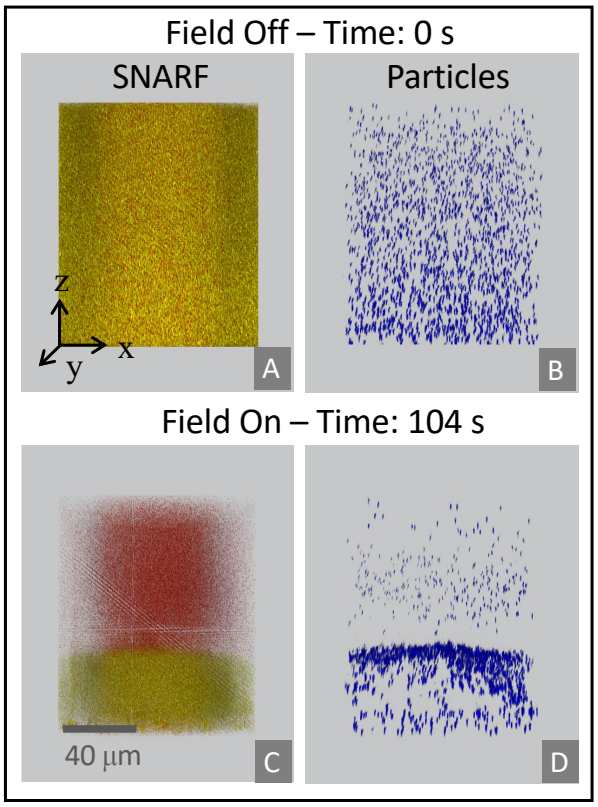

Figure 2.5: Simultaneous imaging of SNARF-1 and charged particles enables linking electrokinetic response to the developing pH gradients. The images correspond to the experimental data represented in Figure 4.4 at the beginning (A-B) and at the end of the experiment (C-D). The images report volumes of cross section area equal to $106 \times 106\ \mu m^2$, electrode gap of 120 μm and detection from three channels centered at 435 nm (blue), 580 nm (yellow-orange) and 640 nm (red).

The permanent surface charge of the particles strongly impacts their response under EDP. Figure 2.6 shows intensity maps for particles of different zeta potential under 4.5 A/m^2, and consequently, in the presence of pH profiles similar to those in Figures 2.2. The particles with the highest zeta potential (-46.8 $\pm$ 1.1 mV) rapidly accumulate away from the electrodes, but the focused band of particles drifts downwards and away from the point where the maximum gradient in pH occurs. Eventually, after 50 seconds, all particles deposit on the anode. As the zeta potential decreases to -43.2 $\pm$ 2.3 mV, particles do not move upwards as readily, but all particles deposit on the anode, as in the previous case. Once the zeta potential decreases to -34.6 $\pm$ 1.6 mV (10 kDa PEG-PS), particles accumulate at the position where the largest gradient in pH is taking place—that is, at the boundary between the basic and acidic zones—although a portion of them remained

dispersed in the region near the anode. As the zeta potential decreases further (-31.9 ± 1.0 mV, 20 kDa PEG-PS), particles move upwards more readily, and as a result, most of the particles join the focused band at the end of the experiment. Even when a high current is applied and a large pH gradient is induced, particles' response depends on the zeta potential, and their behavior falls in the spectrum from deposition to focusing far from the electrodes. If focusing is the desired outcome of an experiment, in addition to the presence of a large pH gradient, particles must have low enough zeta potential to move easily down and up the pH gradient.

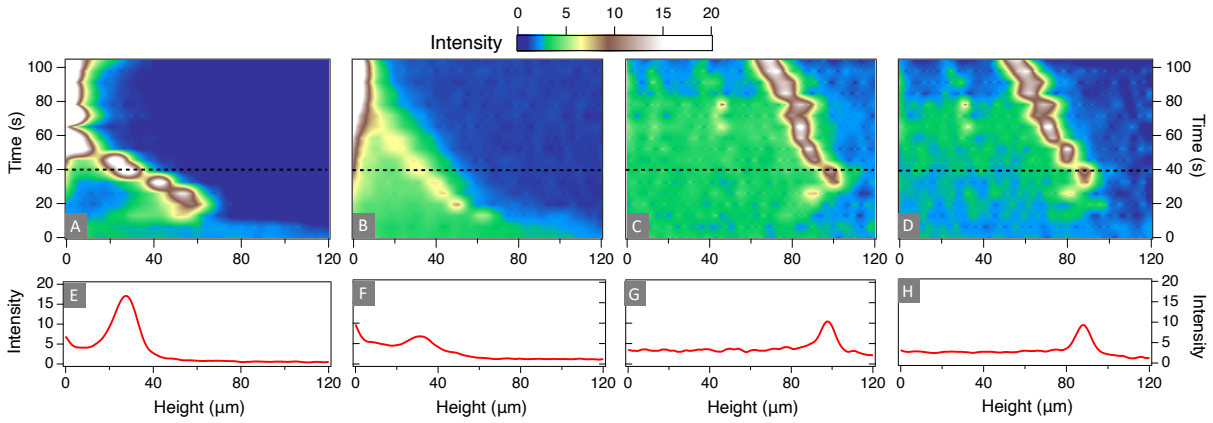

Figure 2.6: The rate of migration towards the position of steepest pH gradient increases as absolute zeta potential decreases. Panels A-D are 2D heat maps that condense the fluorescence intensity from the particles for all times in a single experiment, while Panels E-H represent the intensity profile for a single time (40 s). The average zeta potential for the samples was -46.8 ± 1.1 (A,E), -43.2 ± 2.3 (B,F), -34.6 ± 1.6 (C,G) and -31.9 ± 1.0 (D,H) mV. The applied current was 4.5 A/m^2.

Concentration of a background electrolyte constitute another important variable to control the response of particles. The background electrolyte affects both electrochemical conditions and electrokinetic response of the particles, first by changing the distribution of current among the ions, and second, by setting the Debye length. We chose NaSCN as a supporting electrolyte because, for the range of concentrations in the experiments, it did not change the zeta potential of the particles substantially, increasing from -28.8 ± 1.0 to -23.0 ± 1.1 from at 90 mM NaNO3. In contrast, NaNO3 adsorbs to polystyrene particles due to ion-specific effects, which leads to substantial changes in zeta potential (106). For example, the zeta potential of the PS particles changed from -46.8 ± 1.6 to -5.4 ± 1.0 when

the concentration of NaNO3 changed from 0 to 90 mM. At 0.9 mM NaSCN, which sets the Debye length to 10 nm, particles move rapidly from the cathode to the anode and accumulate at the position of maximum pH gradient (Fig. 2.7A). On the other hand, particles closer to the anode move upwards. As a result, Figure 2.7C shows the particles accumulate into one broad peak close to the anode, and on a another one, at the point where gradient is steepest. Increasing the concentration of NaSCN to 90 mM, which sets the Debye length to 1 nm, induces a significant change in the response of the particles; the velocity of the particles decreases substantially, to the extent that accumulation is minimal at any point within the cell, except at the anode. However, some particles do focus close to the cathode by moving downwards at a rate of approximately 0.4 μm/s. The slight accumulation of particles 20 μm below the cathode is a manifestation of the different distribution of pH at higher concentrations of NaSCN, see Appendix A Figure A.6 for the corresponding pH maps.

2.4.4 Insights on Generation of pH Gradients and the Motion of Particles

Ratiometric analysis and fast imaging with LSCM enables the visualization of local pH and particle distributions with high resolution in space and time. This approach overcomes important challenges related to changes in transmittance of the conductive slides, photobleaching of the dye, and changes in intensity due to scattering from the particles. For the range of applied current density (0.15–4.5 A/m^2), pH gradients are substantial. For example, when a current of 4.5 A/m^2 is applied, pH changes by more than two units from the anode to the cathode. Using LSCM and a variety of pH-sensitive dyes (fluorescein, LysoSensor, carboxynaphtho-fluorescein, and BCECF), other studies have reported similar changes in pH near electrodes after applying a wide range of current densities (0.1–1600 A/m^2) to affect water electrolysis (32; 107; 108). A distinctive feature of the results in Figure 2.3 is the shape of the pH profile; when current densities above 0.5 A/m^2 are applied, pH does not change smoothly from the anode to the cathode. Instead, there was a sharp transition from acidic to basic regions. Figure 2.8 shows the steady-state pH profile

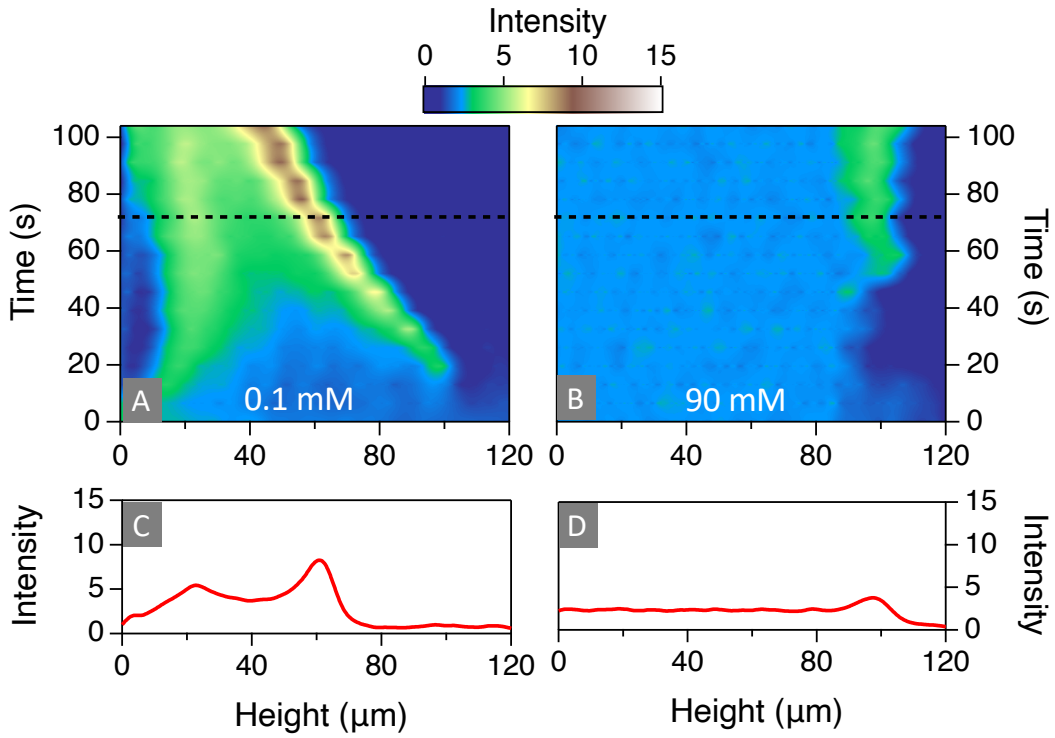

Figure 2.7: The concentration of background electrolyte dampens the effect of pH gradients. Panels A-B are 2D heat maps that condense the fluorescence intensity from the particles for all times in a single experiment, while Panels (C-D) represent the intensity profile for a single time (72 s). The applied current was 4.5 A/m^2, while the average zeta potential of the particles (30 kDa PEG-PS) was -28.8 $\pm$ 1.0 mV.

obtained by solving the transport model after applying current densities between 0.1 and 4.5 A/m^2. At low current densities, the pH increases toward the cathode, similar to what is observed in the experiments. As the current density increases, the sigmoidal shape of the pH profile emerges. When I_d = 0.5 A/m^2, the pH profile shows acidic and basic regions, with a sharp gradient at 90 μm. The model did not account for convection due to changes in buoyancy. However, low ionic conductivity and absence of dense ions limit the effects of buoyancy. In fact, convective transport due to changes in buoyancy throughout the cell will reduce the likelihood that such a profile will form, as detailed in the recent work by Obata et al (109). Therefore, the observed pH profiles result from the transport due to diffusion and migration. Nonetheless, there are noteworthy discrepancies between the experimental results and the predictions from the model. First, the range of values is wider in the model. The model predicts pH values near the anode that are at least one unit lower than the exper-

imental values. In the model, the steady state is reached rapidly, within 10 s. However, in the experiments, the profile continuously evolves and only levels off after 80 s. These differences presumably stem from not accounting for the electrode kinetics and other possible reactions.

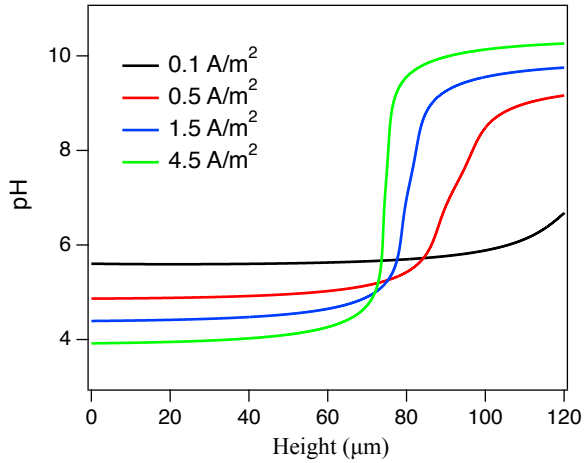

Figure 2.8: Solution of the Poisson–Nernst–Planck equations captures the dependence of the pH profile on current density. The graph shows the pH profiles at a steady state for each current density. The sigmoidal pH profile emerges when the current density reaches values close to 0.5 A/m^2, which is in agreement with the experimental observations in Figure 2.3

The experimental results in Figures 2.3 and 2.4 show that a reproducible point of zero velocity, and therefore focusing, occurs at the transition from acidic to basic regions. Consequently, the point of highest particle concentration coincides with the position at which the gradient in pH is the largest. The lack of focusing in the absence of pH gradients either when using a buffer or when the starting pH is highly acidic, (Appendix Figure A.2) confirms the hypothesis that electrochemically generated gradients of ionic species are needed to affect focusing of charged particles under uniform electric fields. When gradients of redox species are superimposed on electric fields, EDP governs the transport of particles (63). Focusing of charged particles under EDP has been reported using ion-selective membranes, although direct visualization of electroactive species was not presented. Ulberg and Dukhin observed that particles accumulated away from ion-selective membranes (71) and formed non-equilibrium structures, which they termed “fluid deposits” (71). In their

experiments, the fluid velocity tangential to the surface of the membrane sets the thickness of the diffusion layer and, therefore, the position of focusing.

An alternative mechanism to explain the behavior of particles is isoelectric focusing (IEF). In IEF, particles migrate under the influence of an electric field and across a pH gradient until they reach their point of zero charge. IEF requires that particles hold negative and positive charges. Although the carboxylate–polystyrene particles show zero charge at low pH (≈ 3), they do not acquire positive charges at any of the observed pH values, consequently ruling out IEF as the mechanism. Dielectrophoresis is another potential mechanism; however, because the applied electric field is uniform in our experiments, the dielectrophoretic force does not provide a significant contribution.

As a first approximation, EDP can be described by the addition of an electrophoretic and a diffusiophoretic term (71)

$$V_{EDP} = V_{EP} + V_{DP}, \tag{2.6}$$

For a thin double layer, V_{EP} is calculated using the Smoluchowski equation, so for negatively charged particles, V_{EP} points toward the anode. As a result, the upward velocity needed to observe focusing must stem from the V_{DP} term. V_{DP} can be directed toward the anode or the cathode depending on the zeta potential, as well as the diffusivity and gradients of ionic species. Because more than two ions are present in the system, the theories developed for binary electrolytes do not apply, but a qualitative analysis is possible using a theory recently developed by Squires and collaborators for multicomponent systems. The theory provides an expression for V_{DP} that depends on the fluxes (j_i), the diffusivity of the ions (D_i), and the zeta potential ($\tilde{\zeta}_p$)

$$V_{DP} = \frac{K_B T}{n_0^B}\left[M_+ \sum_+ \frac{j_i}{D_i} + M_- \sum_- \frac{j_i}{D_i}\right] with \tag{2.7}$$

$$M\pm = \frac{\varepsilon}{e\eta}\frac{K_B T}{2e}\left[\mp\tilde{\zeta}_p + 4ln(cosh\frac{\tilde{\zeta}_p}{4})\right] \tag{2.8}$$

where n_0^B represents the bulk electrolyte concentration. To calculate V_{DP}, the fluxes for all

species must be known.

The theory reveals that there are two important physical conditions that must be met in order to achieve focusing through pH gradients and DP. First, the concentration profile must be divergent. Particles accumulating away from the electrodes must experience positive and negative V_{DP}, which implies having different fluxes on either side of the focusing point, according to eq 2.6. A change of sign in V_{DP} is possible when divergent fluxes ($\bigtriangledown j_i \neq 0$) are established due to reactions ionic, dissociative, or aggregative. The Nernst–Planck equations provide the fluxes of charged species by adding contributions from diffusion, electromigration, and convection. Except near the electrodes, the electrical potential will vary linearly with distance, and therefore, its second derivative will be zero throughout the cell. Consequently, in the absence of convection, a finite divergence implies $\bigtriangledown j_i \sim \partial^2 n_i / \partial^2 t \neq 0$. The profiles for the experiments at 4.5 A/m^2 and pH_i 7.2 confirm that the fluxes for H^+ and OH^- are indeed divergent because the second derivatives of the concentration profiles are nonzero. The relevant reactions are the faradaic reactions at the electrodes and the dissociation of water. The second constraint involves the diffusivity for H+ and OH– as well as the zeta potential of the particles,

$$\frac{D_{OH^-}}{D_{H^+}} < \frac{\widetilde{\zeta}_p + 4ln\left(cosh\frac{\widetilde{\zeta}_p}{4}\right)}{\widetilde{\zeta}_p - 4ln\left(cosh\frac{\widetilde{\zeta}_p}{4}\right)}. \tag{2.9}$$

All of the particles used in the experiments comply with the second criterion. Although the particles with the highest zeta potential show a mixed behavior of focusing and deposition, experiments in Figure 2.6 follow the trends predicted, where focusing becomes less likely as the zeta potential increases. In addition, calculations of velocity (see Appendix A Figure A.7) using eqs 2.7 and 2.8 show that points of zero velocity do emerge far from both electrodes, leading to focusing. As a summary, the pH profiles that are produced electrochemically in our experiments fulfil the conditions necessary to induce focusing in charged colloidal particles, according to the theory of diffusioresis for multicomponent systems.

The experimental results demonstrate that measurable gradients in pH induce motion that balance and counteract traditional electrophoretic motion. Except for the seminal work of Dukhin and a few recent theoretical and experimental studies, most treatments of colloidal electrokinetics ignore the effects of electrochemically induced gradients. Therefore, by providing the means to simultaneously map concentration gradients and the ensuing colloidal dynamics, this work provides tools to further the understanding of charged particles under electric fields, especially near electrodes. On the other hand, EDP has potential for performing practical tasks in microfluidic devices such as focusing, trapping, and separations.

2.5 Conclusions

The strategy presented in this chapter allows the simultaneous visualization and quantification of local pH and colloidal dynamics within the electrochemical cells. Fast imaging with LSCM enables visualization of pH and particle distributions with high resolution in space and time. The measurements of pH reveals the formation of steep gradients when currents between 0.15 and 4.5 A/m^2 are applied to electrochemical cells with characteristic size of approximately 100 μm. Images of charged fluorescent particles and pH sensitive dye shows that particles accumulate at positions where the pH gradients are largest. Qualitative analysis supports the hypothesis that focusing of particles away from the electrodes is mainly due to the diffusiophoretic contribution through the shape of the electrochemically generated pH profiles.

CHAPTER 3

Long-range Transport and Directed Assembly of Charged Colloids under Aperiodic Electrodiffusiophoresis

3.1 Abstract

Faradaic reactions often lead to undesirable side effects during the application of electric fields. Therefore, experimental designs often avoid faradaic reactions by working at low voltages or at high frequencies, where the electrodes behave as ideally polarizable. In this chapter, I show how faradaic processes under ac fields can be used advantageously to effect long-range transport, focusing and assembly of charged colloids. Herein, I use confocal microscopy and ratiometric analysis to confirm that ac fields applied in media of low conductivity induce significant pH gradients below and above the electrode charging frequency of the system. At voltages above 1 V_{pp}, and frequencies below 1.7 kHz, the pH profile becomes highly nonlinear. Charged particles respond to such conditions by migrating towards the point of highest pH, thereby focusing tens of microns away from both electrodes. Under the combination of oscillating electric fields and concentration gradients of electroactive species, particles experience aperiodic electrodiffusiophoresis (EDP). The theory of EDP, along with a mass transport model, describes the dynamics of particles. Furthermore, the high local concentration of particles near the focusing point leads to disorder-order transitions, whereby particles form crystals. The position and order within the levitating crystalline sheet can be readily tuned by adjusting the voltage and frequency. These results not only have significant implications for the fundamental understanding of ac colloidal electrokinetics, but also provide new possibilities for the manipulation and directed assembly of charged colloids.

3.2 Introduction

Electric fields are useful external inputs of energy because of the large parameter space available—amplitude, frequency, wave form—to tune colloidal transport and interactions. Upon application of an ac electric field, the charges inside and outside particles shift with time, leading to multipoles and induced flows (110; 111; 112). Electric fields induce a variety of surface and body forces that have facilitated applications such as pumping (113), separations (114), and electrodeposition (115). Recently, electric fields have been instrumental in advancing new paradigms in directed (116; 117; 118), dynamic (83; 119),and reconfigurable assembly (40), as well as in colloidal propulsion (120; 121) and directed transport (122).

In directed assembly, external fields—usually of high frequency—are used to tune dipole-dipole interactions between particles to bias the system towards more favorable and desired configurations (29). Field-directed assembly of anisotropic building blocks has produced structures with attractive photonic and phononic properties (e.g., structural colors (5), anisotropic bandgaps(123)). On the other hand, tuning the temporal application of the fields, either through feedback control or toggling, produces colloidal crystals free of defects (124; 125; 118; 126; 127; 128). In addition to dipolar interactions, fields at lower frequencies induce electrohydrodynamic and electroosmotic flows (129; 113). In the vicinity of polarized electrodes, these flows mediate the assembly of particles into 2D structures. Moreover, if the symmetry of the particles is broken, such flows result in self-propulsion and dynamic assembly (80; 81; 120).

Faradaic reactions often lead to detrimental side effects, such as the formation of bubbles or the degradation of electrodes, when applying electric fields. Therefore, experimental designs often avoid faradaic reactions by using low voltages or high frequencies, so the electrodes behave as ideally polarizable (130; 131). Low voltages guarantee working within the electrochemical window of the solvent, whereas high frequencies do not provide enough time for the charging of the double layer. In this context, high frequencies refer

to values much higher than the electrode charging frequency (f_c). Typical values for f_c are in the order of hundreds of Hertz. However, studies have shown that even above f_c in water, faradaic reactions can still take place (132; 133). This finding has important implications for the field of colloidal electrokinetics, for two reasons. First, an increasing number of experiments use frequencies near 1 kHz, or combine steady and oscillating potentials, to control collective dynamics and propulsion (81; 120; 116; 119; 134). By balancing hydrodynamic and dipolar interactions, these experiments produce 2D colloidal materials with rich structural and dynamical behavior. Second, effects associated with faradaic reactions, such as gradients of electrolytes near electrodes caused by the depletion/generation of electroactive species, with some exceptions (69; 70) , do not feature extensively in the mechanistic description of colloidal electrokinetics. Take as an example the intriguing theory of asymmetric rectified electric fields (AREF) (135; 136).This theory predicts that an oscillating electric potential can induce a steady electric field within the liquid when ions have unequal mobilities. The long-range steady electric field has been proposed as the mechanism inducing the levitation of charged particles near planar electrodes (54). However, in its present form, the AREF theory assumes no flux for all ions at the electrodes; essentially, it does not account for faradaic reactions (electrochemistry), which will take place at frequencies below 1 kHz in water.

Recent experimental observations highlight the potential of coupling electric fields with induced gradients of electroactive species to control the assembly and transport of charged particles (13; 14; 134; 137). In chapter 2, we confirmed that electrodiffusiophoresis (EDP)—phoretic motion under diffusiophoresis and electrophoresis—was the mechanism responsible for the focusing and levitation of charged particles under uniform dc fields (138). With the aid of confocal microscopy and ratiometric analysis, we observed that the passage of current through water induces significant pH gradients. Under those conditions, the diffusiophoretic contribution becomes large enough to balance and overcome the electrophoretic contribution. Moreover, the experimental results affirm the generality of EDP

as an electrokinetic phenomenon that is not limited to a single solvent, as suggested by the initial experiments in DMSO (14). the goal in this chapter is to extend the experimental regime to low frequency ac fields. Andrei S. Dukhin and collaborators in the former Soviet Union established the framework for understanding EDP under ac fields (aperiodic EDP) (71; 139; 140). In aperiodic EDP, time-dependent electric fields and gradients of electrolytes lead to directional motion of charged particles. It is important to highlight that, in contrast to dielectrophoresis (110), a nonuniform electric field is not needed to achieve directional motion under aperiodic EDP; an important fact that was supported by the initial experimental results on the subject (71; 141). In this work, we will show how faradaic processes under ac fields, and the motion of particles induced by EDP, can be used advantageously to effect long-range transport, focusing and assembly of charged colloids.

Herein, we use confocal laser scanning microscopy (CLSM) and ratiometric analysis to confirm that ac fields of low frequency (below 1.7 kHz), and applied in media of low conductivity, induce significant pH gradients that can persist above the electrode charging frequency for the system. Charged particles respond to the electrochemical conditions within the cell by migrating and focusing tens of microns away from the surface of the electrodes. By measuring the velocity of migration, we deduce the potential landscape experienced by the particles. These measurements demonstrate that significant wells in potential energy ($\sim 100\ k_B$T) can be induced with moderate electric fields. On the other hand, transport analysis provides further insights on the dynamics of charged particles. Afterwards, we turn the attention to the structural features of the aggregates in the focusing position. The large local concentration of particles near the focusing point leads to a disorder-order transition, whereby particles form crystals. We show that frequency and voltage readily tune the position and crystalline order within the levitating crystalline sheet.

3.3 Methods

3.3.1 Model Systems

The model systems used to study aperiodic EDP were carboxylate-functionalized fluorescent polystyrene particles (CB-PS) of 1.75 μm nominal diameter (Polyscience, 17686-5). All particles were dispersed in ultrapure deionized water (18 MΩ·cm) with a concentration of approximately 0.05 w/v %. The zeta potential (ζ) of particles was measured via electrophoretic light scattering, using a Litesizer 500 (Anton Paar). The average ζ of the negatively charged CB-PS particles was -65.4 ± 3.1 mV.

3.3.2 Experimental Set-up

The same device was used in aperiodic EDP experiment, as disssued in Chapter 2. In a typical experiment, approximately 15 μL of suspension was confined in the device (electrochemical cell). The particles, the fluorescent dye Snarf, and the electrodes were simultaneously imaged using a Leica SP8 CLSM. Water (40×, 1.10 NA) and oil (100×, 1.47 NA) immersion objectives were used. The particles were excited at 405 nm and their emission was collected at wavelengths between 420 and 470 nm. A high-speed resonant scanner (8 kHz) enabled high acquisition rates of up to 28 frames per second, at 512×512 pixel resolution. Two imaging modes were adopted. XZYT mode was used when a high time resolution was desired, whereas XYZT mode was used to capture the motion of all particles within a given imaging volume. The accumulation of particles at the focusing position scatter or block a substantial amount of the excitation light. Therefore, the intensity of excitation was adjusted during a scan, according to the position within the device, using Z-compensation. Adjustment of the laser intensity was particularly useful when imaging in the XYZT mode. Nonetheless, the ratiometric analysis enables the reliable quantification of pH, even when the excitation and emission intensity vary throughout the cell.

The center of the particles in the images was found by using the circle detection function (imfindcircles) in MATLAB. To quantify the crystallinity of an ensemble of particles, we calculated the six-fold bond orientational order parameter, $\Psi_{6,j} = \frac{1}{N_j} \sum_{k=1}^{N_j} e^{i6\theta_{jk}}$. For each

spherical particle j, $\Psi_{6,j}$ is computed based on the number of nearest neighbors, N_j, where θ_{jk} is the angle between nearest neighbor spheres j and k, with an arbitrary reference direction. Using the center for each particle, we also calculate the Voronoi diagram for an image.

3.3.3 Analysis: Transient pH under Low Frequency ac Fields.

A transport model provides insight on the pH profile within the electrochemical cell. We solve the Poisson-Nernst-Planck equations in the liquid domain for the OH^-, H^+ and SNARF-1 species,

$$\frac{\partial n_i}{\partial t} + \nabla \cdot j_i = R_j, \tag{3.1}$$

$$j_i = -D_i \nabla n_i - n_i \mu_i \nabla \psi + n_i u, \tag{3.2}$$

with the mobilities given by the Einstein-Smoluchowski equation, $\mu_\pm = D_\pm ez/k_B T$. D_i and n_i stand for the diffusivity and concentration of ionic species; u and ψ are the velocity and electrical potential. The model solves the transient equation for conservation of ionic species (134; 142). Diffusion, migration and convection determine the fluxes, j_i, of ionic species. The reaction term, R_i, accounts for the equilibrium reaction of water ($2H_2O \rightleftharpoons H^+ + OH^-$) and dissociation of SNARF ($SNARF^{-1} \rightleftharpoons SNARF^{2} + H^+$) within the liquid domain. The dissociation equilibrium of the SNARF molecules occurs between species holding either one or two net negative charges (143). Due to the oscillations in the field, we assume the average displacement due to electromigration is insignificant. Essentially, this assumption simplify the physics to a diffusive mass transport problem. The oscillating voltage leads to an oscillating current at the electrodes. Therefore, the induced electrochemical reactions will be accounted using linearized Butler-Volmer kinetic expressions at the electrodes. Water electrolysis constitutes the most dominant faradaic reaction in the system, which produces protons at the anode and hydroxyl ions at the cathode, when carried out at

neutral pHs:

$$anode: 2H_2O \rightleftharpoons 4H^+ + O_2 + 4e^-, \tag{3.3}$$

$$cathode: 4H_2O + 4e^- \rightleftharpoons 4OH^- + 2H_2, \tag{3.4}$$

At the bottom electrode, the other boundary condition is an oscillating potential (versus reference), $V = V_0 \sin(2\pi t f_r)$, while the top electrode remains grounded. In these calculations, the equilibrium potentials (E_{eq}) for the anodic and cathodic reactions are 0.80 and -0.41; these values were estimated using a Pourbaix diagram for water. The anodic transfer coefficients are the same for both reactions ($\alpha_a = 0.5$). For the reference exchange current densities, we use values equal to 3.98×10^{-3} and 1.38×10^{-3} A/m^2. These values were measured using linear sweep voltammetry. We solved the coupled transport equations using the finite element method as implemented in COMSOL Multiphysics, as well as the respective modules for the transport of dilute species and the tertiary current distribution.

3.4 Results and Discussion

3.4.1 Low Frequency ac Fields Induce pH Gradients

Figure 3.1A-B shows 3D confocal images of the volume within the electrochemical cell before and after applying an ac signal of 5 V_{pp} and 100 Hz, through an aqueous medium containing SNARF-1 and with conductivity (σ) of approximately 2 mS/m. The images show the view from the x-z plane of the volume between the electrodes (green slabs). The images combine the intensity collected at 580 nm (I_1, yellow-orange) and at 640 nm (I_2, red). Initially, the color throughout the cell is uniform, indicating a constant pH of ≈ 7.1. However, after turning on the field, the color within the cell becomes non-uniform, with the intensity from the red channel increasing substantially near the bottom electrode. The changes in relative intensity indicate that significant and measurable gradients in pH are taking place within the electrochemical cell.

Figure 3.1C shows heat plots that condense the temporal and spatial distribution of pH during a single experiment, while Figure 3.1D shows the pH profile for a single time (220

seconds). The values of pH reported in the heat plots were calculated using the calibration equation and the ratio of intensities from the two detection channels near 580 and 640 nm. The color scales in these plots range from bright red (pH 6) to purple (pH 7.6). The pH maps show that a profile forms within 10 s. Once established and until the field is turned off, the pH profile remains steady. From Figure 3.1D, we can appreciate that the pH near the bottom electrode decreases to approximately 6.7. Moving further into the liquid medium, the pH rapidly increases until reaching a peak at 17 μm. At this position, the pH is 7.4. Then, the pH begins to decay linearly to reach values as low as 6.4 near the top electrode. Therefore, the pH near both electrodes decreases below the initial values, prior to the application of the ac signal.

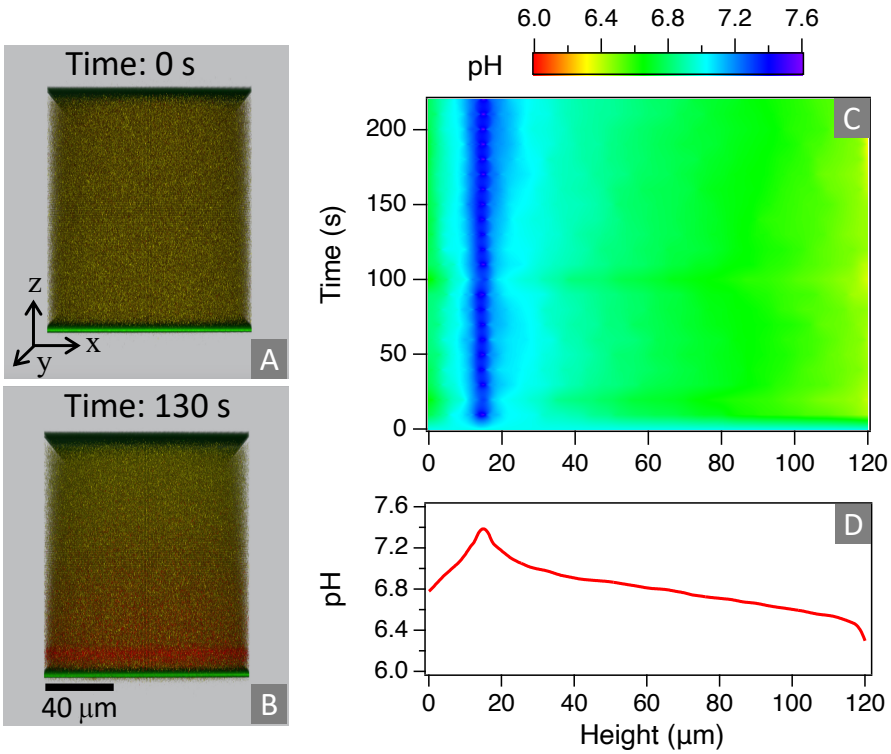

Figure 3.1: Application of low frequency ac fields leads to noticeable changes of pH in aqueous electrolytes of low conductivity. (A-B) Confocal images of the volume between the electrodes (green slabs) before and after applying the field (5 V_{pp}, 100 Hz) for 130 seconds. Notice how application of the ac signal leads to changes in the emission of SNARF-1, indicating changes in pH. Panel C is a 2D heat map that condenses the pH for the entire experiment and at all positions. Panel D shows the pH profile at 220 s. After 10 s, the pH profile becomes highly nonlinear, and a peak emerges at approximately 17 μm from the bottom electrode.

Figure 3.2 shows the steady state profiles for fields generated by applying different

voltages and frequencies. Although the pH profiles take similar times to reach steady state, their shape depends strongly on the parameters of the applied field. First, experiments performed at different voltages, but at the same frequency of 100 Hz, reveal that a threshold voltage is necessary to induce significant changes in concentration of H^+. A clear pH gradient emerges when 1 V_{pp} is applied. Below that threshold, there is only a small linear gradient in pH. As the voltage increases, the peak in pH, occurring at tens of microns from the electrode surface becomes more conspicuous. On the other hand, holding the voltage constant, while applying different frequencies, reveals that significant pH gradients persist at and above 1 kHz. Even at 10 kHz there is a small linear pH profile. Nonetheless, at higher frequencies, the peak in pH occurs closer to the bottom electrode. For example, at 1 kHz, the peak in pH occurs at approximately 7 μm from the bottom electrode, in contrast to 17 μm at 100 Hz.

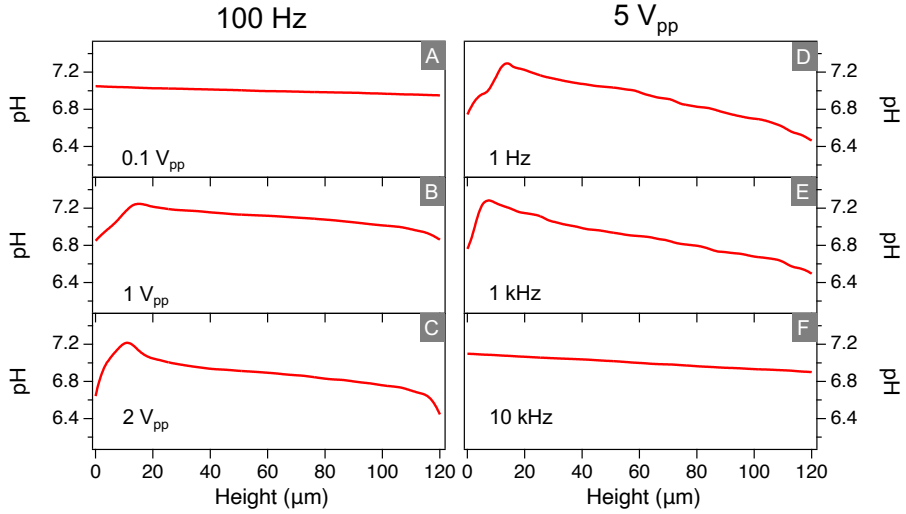

Figure 3.2: A threshold in voltage is needed to induced highly nonlinear pH profiles. Panels (A-C) show profiles for different voltages (0.1, 1 and 2 Vpp) at the same frequency, 100 Hz. Panels (D-F) show profiles for different frequencies (10^{-3}, 1 and 10 kHz) at the same voltage, 5 V_{pp}. Significant pH gradients persist at frequencies slightly higher than 1 kHz.

3.4.2 pH gradients Lead to Long-range Transport and Focusing of Charged Particles.

To study the behavior of charged particles under the oscillating potential, fluorescence intensities from particles and from pH probe (SNARF-1) are recorded simultaneously. Figure 3.3 shows images of particles and SNARF-1 before and 130 s after applying 5 V_{pp} at 100 Hz. Initially, the fluorescence intensities from particles and SNARF-1 are uniform throughout the cell. However, after the field is applied, particles near the top electrode begin to move downwards, while those near the bottom move upwards. After 100 s, most particles are focused at a position that is 17 μm from the bottom electrode. The accumulation of particles causes significant scattering and absorption of excitation light, resulting in noticeable changes in fluorescense of SNARF-1 above the focusing point. Nonetheless, ratiometric analysis accounts for those variations since it does not rely on absolute intensity to obtain local pH. The pH maps and pH profiles obtained from experiments with and without particles look similar (Fig.3.1), suggesting that at the low volume fraction used in these experiments, the pH profile is not significantly affected by the presence of the particles. Consequently, the pH profiles are still determined by the electrochemical conditions of the system. Figure 3.3G shows fluorescence intensity maps from particles, for all times in a single experiment. The intensity map shows that particles begin to focus as soon as the field is applied. Comparing the pH (Fig.3.3F) and intensity profiles (Fig.3.3.H) after 220 s, it is apparent that particles focus at the point of maximum pH. This significant observation suggests the peak in pH gradient induces a potential capable of focusing and trapping the particles.

Experiments with particles under different voltages and frequencies show that a divergent and nonmonotonic pH profile is needed to observe focusing. Figure 3.4 compares pH and intensity profiles for experiments at different frequencies and voltages. The changes in the shape of the pH profiles are mirrored in the intensity profiles from the particles. In contrast to 2 V_{pp}, focusing is not observed at 0.1 V_{pp}. Furthermore, in comparison to 100

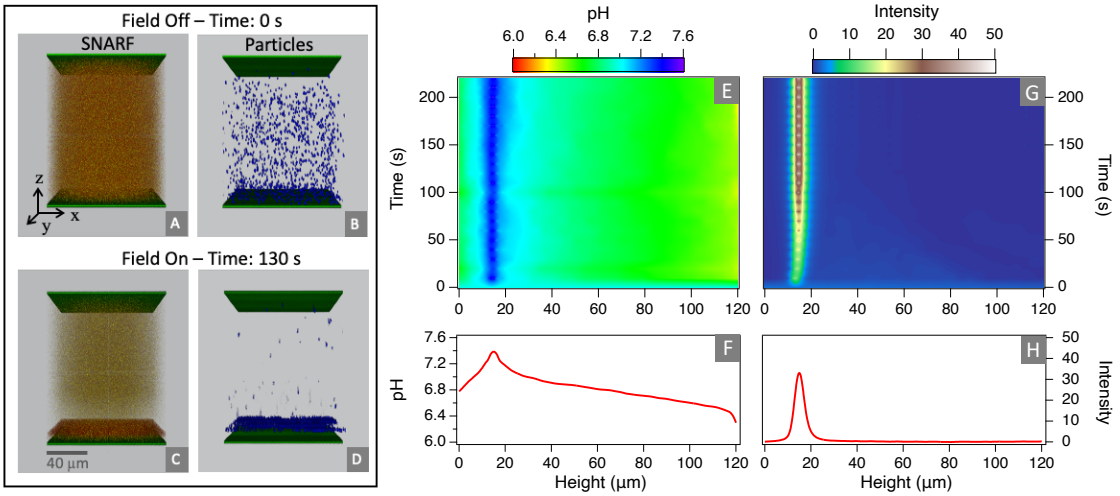

Figure 3.3: Particles respond to applied ac fields by focusing at the position of maximum pH. (A-D) Confocal images of SNARF and fluorescent particles acquired simultaneously before and after applying an ac field (5 V_{pp}, 100 Hz) for 130 s. The images report volumes of cross section area equal to 106 $\times$ 106 μm, electrode gap of 120 μm, and detection from four channels centered at 435 nm (blue), 580 nm (yellow-orange), 488 nm (green) and 640 nm (red). Panels E and G are 2D heat maps that condense the pH and the fluorescence intensity from the particles for all times in a single experiment, while Panels F and H represent the pH and intensity profile for a single time, after reaching steady state. Notice how particles focus at the point of highest pH.

Hz, the peak in pH for 1000 Hz occurs at approximately 8 μm. The intensity profile shows that the particles accumulate closer to the electrodes, but exactly at the same position where the peak in pH is taking place. To sum up, particles are transported to the point where the maximum pH values occur. Also, notice that although a divergent and nonmonotonic pH profile forms at 1 Hz, the rate of accumulation of particles is much smaller than at either 100 or 1000 Hz, confirming the important role that the pH profile plays.

Next, I look into the dynamics of the particles by measuring the migration velocity under different voltages, but at the same field frequency. To measure the velocity of the particles throughout the whole cell, two sets of experiments were performed. First, particles were allowed to completely sediment on the top electrode for at least 4 hr. Then, once all particles were experiencing Brownian motion in the vicinity of the electrode, the device was mounted on the microscope stage. To measure the velocity below the focusing point, particles were allowed to sediment on the bottom electrode instead. Once the field was turned on, particles began to move in a band, whose position at any time was easily

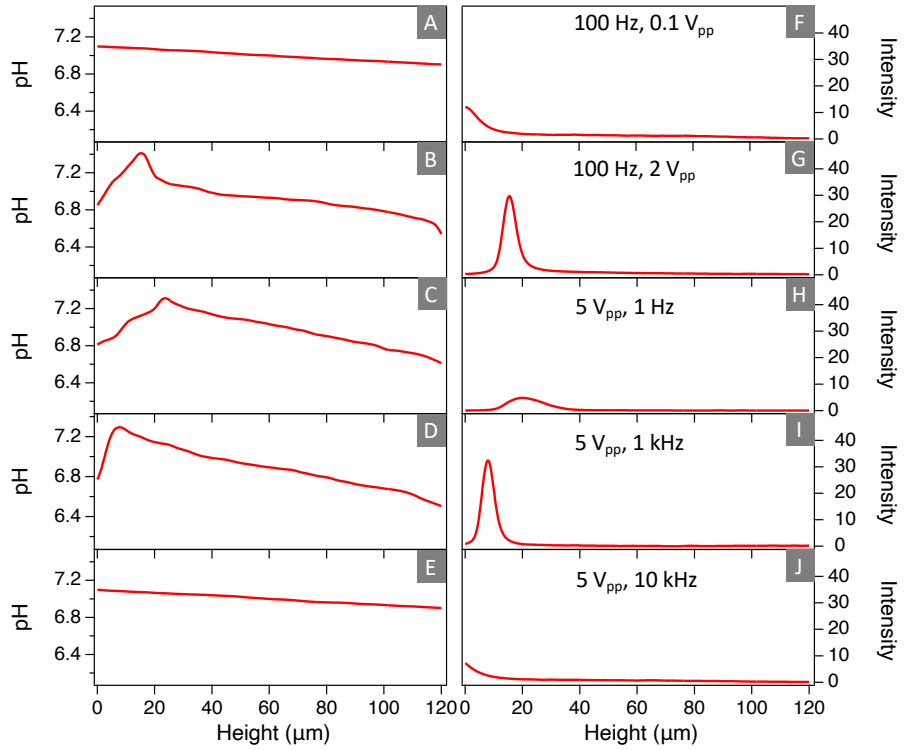

Figure 3.4: Rapid migration and focusing of particles occur when highly nonlinear and nonmonotonic pH profiles are induced. Profiles of pH (A-E) and fluorescence intensity of particles (F-J) for experiments at different voltages and frequencies. Linear pH profiles do not lead to significant motion; in those cases, particles move downwards due to gravity. For all the experiments, the respective heat maps condensing the pH profiles and intensity for all times are provided in Appendix Figure 7 and 8.

determined by tracking the intensity profile (Appendix B, Figure B.7-8). From such visual tracking, the velocity was calculated by determining the position as a function of time.

Figure 3.5 A shows the velocity profiles of particles under different voltages. First, from top to bottom, particles initially accelerate until reaching a plateau about 20 microns from the electrode. The plateau in velocity extends for approximately 70 microns. Then, 30 μm from the bottom electrode, particles briefly accelerate again, but rapidly decelerate towards the focusing point. For particles moving upwards from the bottom electrode, initially the velocity is constant for the first 15 μm, and then they quickly decelerate towards the point of zero velocity. The applied voltage influences the observed velocity. For example, at the plateau, the values of velocity are about 0.5 μm/s and 1 μm/s for 1 V_{pp} and 5 V_{pp}, respectively. Similarly, close to the bottom electrode, the velocity of particles under 1 V_{pp}

is about 60 % the value under 5 V_{pp}. Again, notice that although the particles reach the same final position, the dip in velocity before reaching the focusing point is quite sensitive to the applied voltage.

To get an idea of the relative importance of diffusive and convective transport, a Peclet number ($Pe = 2U_0R/D_0$) is calculated; U_0 and D_0 represent the free particle velocity and diffusivity. Using the values presented in Figure 3.5A, *Pe* can be as high as 25 for 5 V_{pp}, and as low as 1 for 0.1 V_{pp}, where no significant gradient is induced. Therefore, aperiodic EDP generates conditions where convective transport can dominate diffusive transport.

The previous section showed that points of zero velocity within the cell lead to focusing of particles far from the electrodes. In this regard, the devices work as electrokinetic traps. Therefore, the potential landscape provides further information about the capabilities of the system to focus and trap colloids in the z-direction. The potential landscape experienced by the particles, $V(z)$, can be deduced from the velocity profiles presented in Figure 3.5A and the following formula,

$$V(z) = -\int_{z_0}^{z} F\,dz = -6\pi\mu R \int_{z_0}^{z} U(z)\,dz. \tag{3.5}$$

The force, F, is deduced from Stokes expression. Figure 3.5B shows the potential experienced by the particles under ac fields generated by applying voltages of 0.1, 1, 2, 5 V_{pp}, at 100 Hz. First, the potential landscape for the particles under the lowest field, 0.1 V_{pp}, is similar to the gravitational potential. The curve shows a linear increase with height, as expected for particles experiencing a uniform gravitational force. The following expression gives the potential energy due to gravity,

$$V_g(z) = \frac{4}{3}\pi R^3 \left(\rho_p - \rho_f\right) gz, \tag{3.6}$$

where R represents the radius of particles; ρ_p and ρ_f are the density of particles and fluid, respectively. The particles move down at rates similar to sedimentation velocity (≈ 0.1

μm/s). Once the applied voltage increases, the potential landscape changes dramatically. For 1, 2, and 5 V_{pp}, the potential decreases rapidly until it reaches a minimum, approximately 17 μm from the bottom electrode. Then, the potential increases rapidly, albeit at a different rate. There are several noticeable features in these curves. First, the potential energy under EDP is substantial, and the particles experience potential wells that are higher than 100 k_BT. Second, some properties of the potential landscape can be easily adjusted by changing the field parameters. The applied voltage adjust the depth as well as the stiffness of the potential well. Notice how the slope after the energy minimum changes with the applied voltage. All these features provide potentially useful handles to manipulate the position and collective structure of charged colloids through directed assembly (see Section 3.4.4).

3.4.3 Mechanistic Insights into the Motion of Particles under Aperiodic EDP

The characteristic charging frequency of the electrodes is related to the finite time needed to form a double layer in an ac field, $\left(f_c = \frac{\sigma}{\varepsilon} \cdot \frac{\lambda_D}{L}\right)$. σ, ε, and λ_D represent the conductivity, permittivity, and Debye length of the medium, whereas L stands for the characteristic length scale of the system. When the applied frequency is much lower than f_c, the double layer has enough time to form, and the faradaic reactions proceed at rates similar to those under direct current. In contrast, at frequencies much higher than f_c, the rate of faradaic reactions becomes negligible. The frequencies used in this study were both below and above the electrode charging frequency. For experiments without any indifferent electrolytes, as well as $\lambda_D = 30$ nm and $\sigma = 2$ mS/m, $f_c \approx 700$ Hz in the system. Thus, the electrolysis of water has enough time to occur. Consequently, the production of H^+ and OH^- drives the formation of pH gradients. Moreover, substantial changes in pH have been reported even at frequencies as high as $10 \times f_c$ (132). These observations have important implications for the study of colloidal electrokinetics. Notice that this frequency range is often chosen for studying the propulsion and assembly of colloids (81; 120; 119; 54). However, with some exceptions (144; 70), the effect of faradaic processes, and the ensuing gradients of

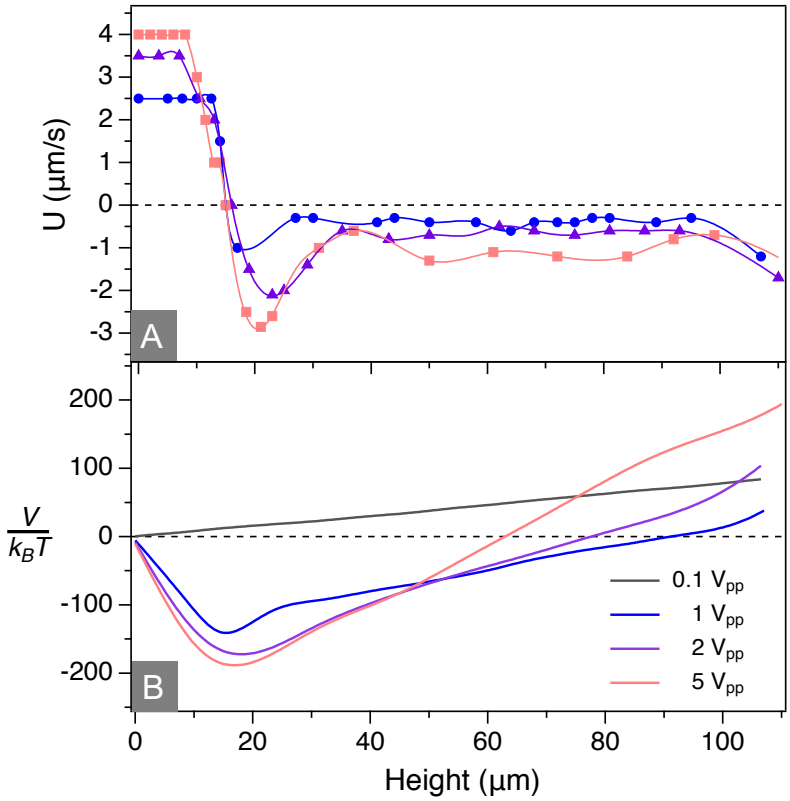

Figure 3.5: (A) Velocity profile under different applied potentials and constant frequency, 100 Hz. The solid lines—provided for guidance—are interpolation of the data using cubic splines. (B) Potential landscape calculated from velocity profiles in Panel A. The potential energy (V) is given with reference to thermal energy (k_BT).

electroactive species, have not been an integral part of the physical description for the forces acting on charged particles under ac electric fields (116; 134; 54). An important barrier has been the need to measure concentration and fluxes of ionic species with high spatial and temporal resolution.

The transport model reproduces the basic features of the experiments. Figure 3.6A shows pH profiles obtained from solutions of the transport equations using an oscillating voltage, and electrode reactions, as boundary condition. First, the model predicts a flat or small linear pH gradient at low voltages. As voltage increases, a peak in pH profiles emerges 5 μm from the bottom electrode. Further away, the pH decreases monotonically. There are some differences with experimental pH profiles; for example, calculations predict

larger peaks in pH that occur closer to bottom electrode. Despite those differences, the model confirms that an oscillating voltage, along with resultant production of H^+ and OH^-, leads to nonlinear, nonmonotonic and divergent pH profiles, like those shown in Figure 3.1. It is important to note that these calculations were performed in the absence of SNARF-1 since equations Eq.3.9 is valid for monovalent ions. Nonetheless, when the SNARF ion are included, pH profiles resemble those shown in Figure 3.6A. As a first approximation, EDP can be described by the addition of an electrophoretic and a diffusiophoretic term:

$$U_{EDP} = U_{EP} + U_{DP}. \tag{3.7}$$

For a thin double layer, U_{EP} is given by the Smolowchowski equation, but if the zeta potential does not change substantially during one period of the field, then U_{EP} approaches zero due to the oscillating nature of the signal. As a result, the upward and downward velocities needed to observe focusing must stem from the U_{DP} term. U_{DP} depends on the zeta potential, as well as the diffusivity and gradients of ionic species. Since more than two ions are present in the system, the theory developed by Squires and collaborators for multicomponent systems is suitable (145). This theory provides an expression for U_{DP} that depends on the fluxes (j_i), the diffusivity of the ions (D_i) and the normalized zeta potential ($\widetilde{\zeta_p}$):

$$U_{DP} = \frac{k_B T}{n_0^B}\left(M_+ \sum_+ \frac{j_i}{D_i} + M_- \sum_- \frac{j_i}{D_i}\right), \tag{3.8}$$

$$\text{with} \quad -M_\pm = \frac{\varepsilon}{e\eta}\frac{k_B T}{2e}\left[\mp\widetilde{\zeta_p} + 4ln\left(cosh\frac{\widetilde{\zeta_p}}{4}\right)\right]; \tag{3.9}$$

n_0^B represents the bulk electrolyte concentration.

Figure 3.6B shows the velocity profile calculated using the theory above. The curves reproduce several important features of the experiments. First, and most importantly, points of zero velocity appear where the corresponding maximum in pH occurs. Similarly, the velocity profiles show regions of positive velocity (close to the bottom electrode) and regions of negative velocity (above the focusing point). Second, velocity profiles at 0.6 and 1 V_{pp}

show a dip before reaching the point of zero velocity. Also, like in the experiments, focusing only happens at higher voltages. Lastly, the magnitude of the calculated velocity is similar to those observed in the experiments, $\sim 1\,\mu m$, specially near the bottom electrode. Nonetheless, points of zero velocity in Figure 3.6B occur closer to the electrode for 100 Hz. The overall agreement between modeling and experimental results supports the hypothesis that aperiodic EDP induces long-range transport and focusing of charged particles.

While developing the previous hypothesis that pH gradients and ac faradaic currents induce focusing, alternatives were also considered other. For example, if dielectrophoresis was the mechanism responsible for the directional motion of particles, a nonuniform electric field had to be present. However, the geometry of the device ensures that the potential is geometrically uniform. Another possibility is isoelectric focusing (IEF). In IEF, particles migrate under the influence of an electric field, and accross a pH gradient, until they reach their point of zero charge. In this case, focusing would require that particles hold negative, as well as positive, charges on either side of the isoelectric point. However, the carboxylate-polystyrene particles show zero charge at low pH (~ 3) and do not acquire positive charges at any pH. Therefore, it will not be possible for particles to reach an isoelectric point where maximum pH occurs. A third potential mechanism is AREF; however, two important observations are not consistent with AREF (135; 136; 54). First, the experiments show that reactions are taking place, thus a key assumption in the AREF theory is violated. Second, particles only focus when there is a nonmonotonic and divergent pH gradient. Without such pH profiles, particles neither levitate nor focus; such is the case when buffers or highly acidic solutions are used (see Appendix B Figure B.5-6). Similarly, what controls the position of focusing is the point of highest pH, which can be modulated with frequency, voltage, initial pH and concentration of electrolytes.

3.4.4 Induced Potential Landscapes Lead to Disorder-order Transitions

The ability of aperiodic EDP to focus and concentrate particles in a narrow region can be used to explore the phase diagram of the system. Therefore, I now look at the struc-

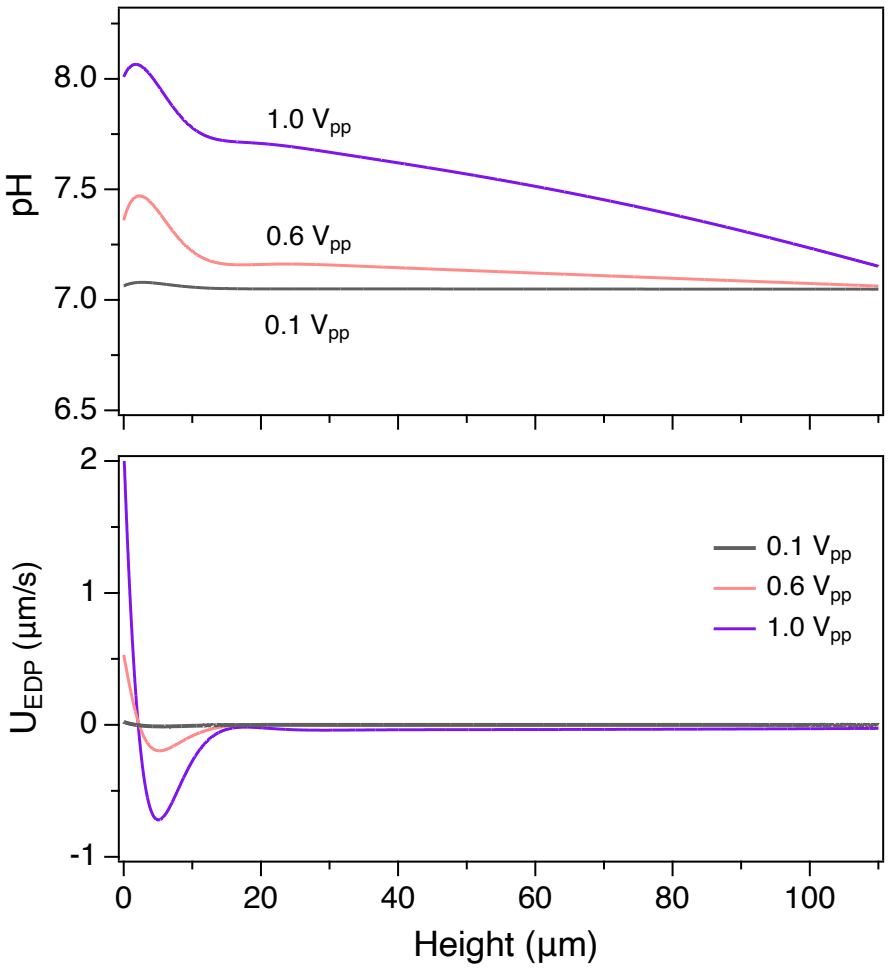

Figure 3.6: (A) pH profiles generated by solving the transport model at 100 Hz, and different oscillating voltages at the bottom electrode. The top electrode stayed grounded. (B) Velocity profiles calculated using equations (3.7-3.9) and the pH profiles shown in Panel A.

tures that form once particles have migrated from the bulk, which generally occurs after approximately 90 seconds. Figure 3.7 shows images at the focusing position for different starting volume fractions. At low volume fractions, $\phi \approx 4.8 \times 10^{-4}$, hundreds of particles form clusters (Figure 3.7A). Images at higher zoom (Figure 3.7B-C) suggest little crystalline order and lack of close packing. As a quantitative measure of local crystallinity, the small value for the bond order parameter, $\Psi_6 \approx 0.04$, confirms the lack of local order. Furthermore, the lack of close-packing is reflected in the high interparticle distance — $d_{cc} = 1.7 \pm 0.1$, in particle diameters.

Setting the volume fraction to 2.4×10^{-2} leads to complete coverage for the cross-

section at the focusing position, Figure 3.8D. Images at higher magnification (Figure 3.7E-F) reveal the outstanding transition into a highly organized array. Particles organize into 2D hexagonal crystal lattices, with a high bond order parameter, $\Psi_6 \approx 0.89 \pm 0.10$, and low interparticle distance, 1.18 ± 0.03. The crystal lattices include defects such as vacancies, grain boundaries and dislocations, as reflected by the standard deviation in Ψ_6. Aperiodic EDP induces a phase transition by increasing the local concentration many folds. The formation of clusters at low volume fractions suggests the presence of pair-wise hydrodynamic interactions. Nonetheless, I argue that the transition to hexagonal lattices originates from the equilibrium phase behavior of colloidal hard spheres. In this view, the potential landscape induced by aperiodic EDP transport, focus and concentrate particles to the point of a phase transition. Although detailed thermodynamic and kinetic analysis are beyond the scope of this work, it is instructive to assess the basic features of the observations in the context of field convective assembly. The change of volume fraction within a system can be described using a convection-diffusion equation that was originally formulated for sedimentation, and recently adapted for the case of electric fields (146; 147; 148). The convection-diffusion equation indicates that changes in volume fraction (ϕ) at a height (z), and time (t), occur through the contributions of convective and diffusive fluxes,

$$\frac{\partial \phi}{\partial t} + U_0 \frac{\phi K(\phi)}{\partial z} = D_0 \frac{\partial}{\partial z}\left(K(\phi) \frac{d}{d\phi}[\phi Z(\phi)] \frac{\partial \phi}{\partial z} \right). \tag{3.10}$$

U_0 represents the free particle velocity induced by the field; $K(\phi)$ accounts for the hindrance experienced by particles at higher concentrations, and $Z(\phi)$ stands for the compressibility factor of the suspension. In this case, aperiodic EDP causes the convective flux, with characteristic values of velocity presented in Figure 3.6. The convective term could also stem from gravity (147; 148), evaporation (149; 150), dc fields (146; 84) , and dielectrophoresis (151; 152).

Under equilibrium, the accumulation term becomes zero, while the convective and diffusive fluxes become equal. In other words, the Brownian force balances the external force

due to Aperiodic EDP,

$$\frac{\partial \Pi(n)}{\partial z} = -\frac{\partial V(z)}{\partial z} \cdot n(z). \tag{3.11}$$

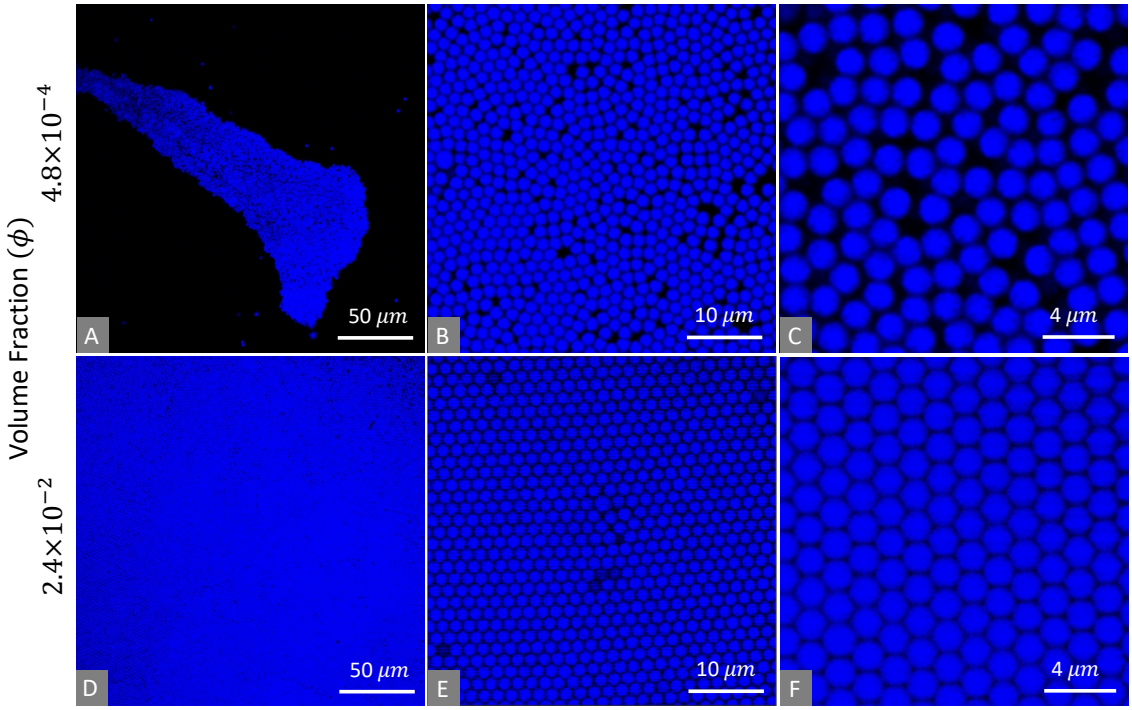

Figure 3.7: Once at the focusing point, particles form aggregates of different local order. (A-C) Images at the focusing point for starting volume fraction of 4.8×10^{-4}. At low volume fractions, particles form aggregates with low local order. (D-F) Images at the focusing point for starting volume fraction of 2.4×10^{-2}. At higher volume fractions and surface coverage, particles form crystals with hexagonal lattices. In this experiment, an ac field (5 Vpp, 100 Hz) was applied and images were taken after all particles reached the focusing point. Colloidal crystals form 15-17 μm above the bottom electrode.

The Brownian force is written in terms of the osmotic pressure, Π, and the number density of particles, n. The external force and potential landscape induced by aperiodic EDP was shown in Figure 3.5. The osmotic pressure is connected to the structures accessible to hard spheres via an equation of state,

$$Z(\phi) = \frac{\Pi(\phi)}{nk_BT}, \tag{3.12}$$

where the compressibility factor ($Z(\phi)$) captures the deviation from the osmotic pressure of an ideal solution, as the number density of particles increases. The specific form that $Z(\phi)$ takes depends on the phase of the system—liquid, solid, or glass (153; 154). In

these experiments, transport to the focusing position, and the subsequent accumulation of particles, increases the volume (area) fraction, thus inducing a transition from a fluid to a close-packed solid. For hard spheres, the coexistence of fluid and crystalline phases occurs at volume fractions between 0.49 and 0.54. For hard disks in 2D geometries, the coexistence region occurs for area fractions between 0.69 and 0.716 (152; 151).

We can tune the osmotic pressure, and therefore the structure formed by the particles, through the potential landscape (Eq. 3.11). The tunability of the potential landscape (Figure 3.5) with field parameters suggests a strategy to modulate the local order and position of the crystalline phases. First, the frequency of the field determines the position of minima in potential energy, thus providing a handle to control where crystallization occurs. Figure 3.8A shows how crystallization can be induced at distances as far as 15-17 μm and as close to the electrode as 3 μm. Remarkably, when 5 V_{pp} is applied, the particles maintain their crystalline order at high frequencies, although the focusing distance changes. The highest focusing points occur at lower frequencies (1-100 Hz). As the frequency increases, the focusing point decays monotonically to zero. At frequencies above 1700 Hz, particles deposit on the surface of the electrode. As soon as particles are brought to the surface of the electrode, they disassemble, which correlates with the lack of nonmonotonic and divergent pH profiles at high frequencies.

On the other hand, the magnitude of the applied voltage has two effects: first, it changes the minimum in potential energy and the rate of change around it. Therefore, the applied voltage enables adjusting the order of the crystalline phases (see eqn. 3.11). Figure 3.8B shows the bond order parameter and the interparticle distance for experiments under the same frequency, but different voltages. Ψ_6 is small for voltages below 2 V_{pp}, but it increases rapidly between 2 and 3 V_{pp}. The rate of change decreases above 3 V_{pp} until the highest values are achieved at 5 V_{pp}. The interparticle distance displays the opposite trend; d_{cc} decreases rapidly between 1 and 3 V_{pp}. Figures 3.8C-F are representative images at each voltage. The images superimpose the contthiss identifying each particle and the respective

Voronoi polygons. The images unequivocally demonstrate the effect of the voltage on the resultant structures. Crystalline phases with long-range order—as demonstrated by the presence of mostly hexagons in the Voronoi diagram—can be achieved at voltages above 3 V_{pp} (Figure 3.8E). At lower voltages, the crystalline order deteriorates due to the inability of the field to keep particles tightly focused. For example, although the particles are all concentrated in a narrow band under 1 and 2 V_{pp}, many of them appear slightly out of focused, judging from their appearance as half-moons.

2D crystals of colloidal particles can be achieved using coplanar or parallel plate electrode geometries, by modulating dipolar interactions or EHD flows. However, what is unusual in these experiments is the combination of long-range transport, focusing, and crystallization far from the electrodes, through a single mechanism, in a simple geometry. Furthermore, crystallization away from the electrodes facilitate reconfigurability by minimizing irreversible adsorption. Figure 3.8B shows that the bond order parameter can be adjusted with voltage, while maintaining focus away from the electrodes. It is important to highlight that particles transition from one state to another with significant speed. The change occurs in a couple of seconds, although achieving maximum order takes longer when cycling from low to high voltage, but still within 10 seconds. In future work, the transition from one state to another could be optimized through toggled fields. Therefore, aperiodic EDP can be a tool for reconfigurable assembly.

Inducing EDP with ac fields is convenient. In dc fields, the progressive depletion of redox species leads to either increasing voltages (galvanostatic mode) or decreasing currents (potentiostatic mode). Both situations result in undesirable effects. In the first case, rising voltages often lead to degradation of electrodes; for ITO, degradation implies loss of transparency. In the second case, the driving force for assembly decreases with time. Also, relevant forces are induced in a simple geometry, using electrodes that do not need patterning through microfabrication. Nonetheless, it is important to keep in mind that low conductivities, and pH values close to neutral, were needed to observe focusing and crys-

tallization.

3.5 Conclusions

In this chapter, I have employed aperiodic EDP to effect long-range transport, focusing and colloidal crystallization. Confocal microscopy and ratiometric analysis showed that applying low frequency ac fields, $\sim$ 1000 Hz, to aqueous media in a parallel plate geometry leads to significant pH gradients, with changes as large as 0.6 units. Transport analysis indicated that oscillating currents from the electrolysis of water can reproduce key features of the experimental pH profiles. The induced pH gradients cause the motion of charged particles over tens of microns towards a point of zero velocity, thus promoting focusing far from the electrodes. These results confirmed that uniform ac electric fields can be used to effect directional motion under aperiodic electrodiffusiophoresis. In contrast to dielectrophoresis, a geometrically nonuniform field is not required. Calculations showed that potential wells larger than 100 k_BT tightly confine particles in the vertical direction. Furthermore, when experiments were performed at higher volume fractions, particles displayed a disorder-order transition into colloidal crystals with hexagonal lattices.

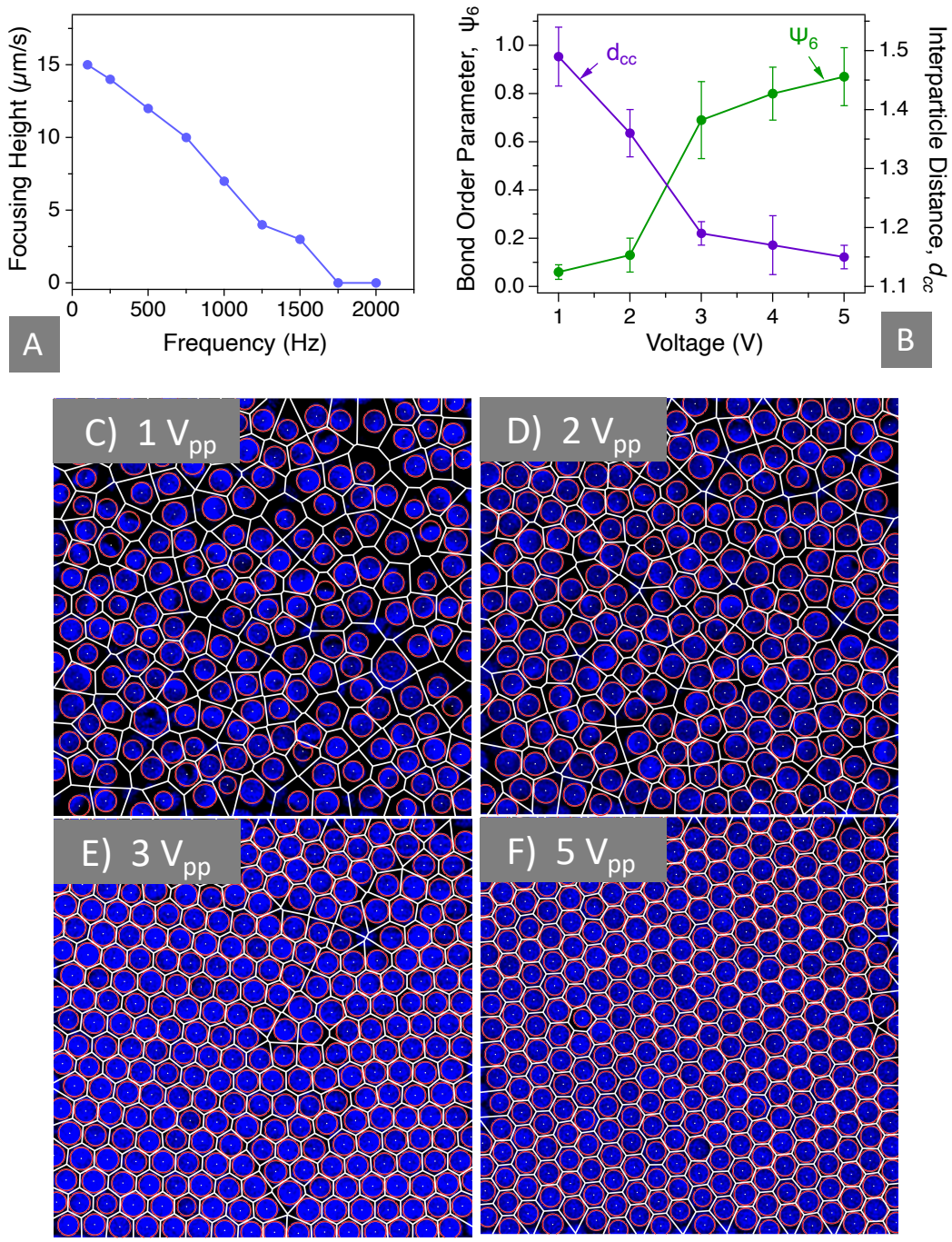

Figure 3.8: Frequency of the field (Panel A) modulates the position of the colloidal crystals, whereas the applied voltage (Panel B) determines the local bond order parameter and interparticle distance. Voltages above 3 V_{pp} leads to highly ordered structures. (C-F) Representative images of the structures that form under different voltages. The images superimpose the Voronoi diagram and the fluorescent particles. Each particle is identified by its contthese (red line) and center (white dots). The volume fraction of particles was 2.4×10^{-2}. Images represent areas equal to 30×30 μm.

CHAPTER 4

Aperiodic Electrodiffusiophoresis: $k_{\mathbf{B}}T$-scale Interparticle Potentials, Local Chemical Gradients and Assembly.

4.1 Abstract

Electric fields are widely used to tune the transport and interparticle interactions of colloidal materials. However, colloidal dynamics has rarely been studied under electrodiffusiophoresis (EDP)—the combination of electrophoresis and diffusiophoresis. In this chapter, I describe how EDP induces long-range interparticle potentials (> 1 μm) that lead to phase transitions. High resolution visualization reveals that local pH gradients and the resulting diffusiophretic attraction underlie the interaction potentials. The local chemical fields can be readily modulated by the field parameters and the surface chemistry of the particles. For example, while carboxyl-polystyrene particles show increasing pHs near their surface, silica and plain polystyrene particles show negative or no change in pH. This finding readily explains the tendency of carboxyl-polystyrene particle to form solid phases, while silica and plain polystyrene particles form liquid or gas phases, without long range order. Experiments under semi-dilute conditions measuring the kinetics of aggregation show a correlation between the kinetic rate constant for the depletion of singlets and the ΔpH. These discoveries open the door for another parameter space for the dynamic assembly of materials and the design of responsive matter.

4.2 Introduction

Colloidal materials display impressive features such as self-assembly, self- propulsion, and dynamic assembly. These features are promising for achieving advanced materials that mimic the versatility of natural systems. Electric fields are useful external inputs of energy because of the large parameter space available—amplitude, frequency, wave form—to tune transport and interparticle interactions. In combination with a rapidly expanding library of

particles, ac fields have produced a wide diversity of structures, and enabled fine control over defects as well as dynamics. The combination of electrophoresis and diffusiophoresis leads to electrodiffusiophoresis (EDP). Compared with those for electrophoresis (155; 68), dielectrophoresis (110), diffusiophoresis (95; 96; 156; 157; 158) and induced charge electrophoresis (ICEP) (80; 113), the available theoretical and experimental results for EDP are limited. Colloidal dynamics under EDP has rarely been studied since the seminal work by A.S. Dukhin in the former Soviet Union (69; 71; 72; 139; 140; 141). Consequently, colloidal transport under EDP remains vastly underutilized in reconfigurable assembly, microfluidics and actuation of soft materials. Nonetheless, in the context of directed assembly and micro/nanofluidics, fthe recent reports illustrate the potential of EDP for manipulation of colloidal dispersions (77; 134; 137; 159). For example, by inducing electrodiffusioosmotic (EDO) flows in nanopores (160), Lin et al. demonstrated negative differential resistance, where current decreases with the application of higher voltages (159).

Chapter 3, I established that significant pH gradients persist even at frequencies as high as 1.7 kHz, several times above the charging frequency of the electrodes (161). Strikingly, particles migrate away from both electrodes— with Péclet numbers (*Pe*) as high as 25—and focus at the position of maximum pH. Once at the focusing position, particles experience an outstanding transition from a fluid to a close-packed crystal. By adjusting the potential landscape under EDP—for example, by changing the voltage—particles form crystals of different order. In summary, a simple setup of parallel electrodes generating uniform fields can induce a rich physical scenario for long-range transport, trapping and structuring of complex fluids under EDP. However, it is not clear what interparticle forces result from the superposition of migration and diffusive fluxes on the charged particle.

In this chapter, I investigated the origin of the interactions that lead to phase transitions under electrodiffusiophoresis (EDP). First, I employed positional tracking of dimers at the focusing point to measure the potential landscape. The particles experience long-range ($> 1\mu$m) pairwise potentials, on the order of a few k_BT. Then, high resolution visualiza-

tion and ratiometric analysis reveal that low frequency AC electric fields not only induce global pH gradients, but also local ones. At the scale of each particle, these chemical fields lead to diffusiophoretic attraction. We study the manifestation on the assembly of particles by measuring the kinetics of aggregation and assembly. This mode of transport and interparticles forces will be useful in controlled transport, directed assembly and separation processes.

4.3 Methods

4.3.1 Model Systems

The model systems used were fluorescent polystyrene particles (PS) (2 μm) , carboxylate-functionalized fluorescent polystyrene particles (CB-PS) (1 μm, 1.75 μm and 5 μm) and silica particles (2 μm). All particles were dispersed in ultrapure deionized water (18 MΩ cm^{-1}) with a concentration of approximately 0.00025 w/v% for the study of interparticle forces. Measurements of zeta potential (ζ) were performed in a Litesizer 500 (Anton Paar) through electrophoretic light scattering. All three particles were negatively charged, with an average ζ value of 65.0 $\pm$ 3.1 mV for CB-PS, -48.2 $\pm$ 4.4 for PS and -50.2 $\pm$ 5.5 for silica particles . To change the ζ of CB-PS, particles were modified by cross-linking poly(ethylene glycol) (PEG) chains of different molecular weights (5 and 10 kDa) to the carboxylate groups (PEG-modified particles, PEG-PS). Particles became less negatively charged after the attachment of PEG molecules and the magnitude of change was modulated by the molecular weight of PEG. ζ for the 10 kDa PEG-PS and 5 kDa PEG-PS were 38.8 $\pm$ 2.1 mV and 46.1 $\pm$ 1.9 mV, respectively.

4.3.2 Experimental Set-up

Figure 4.1A shows the experimental setup, similar to that discussed in Chapter 2. In a typical experiment, approximately 15 μL of suspension was confined in the electrochemical cell. The ac electric fields were applied using a function generator (Rigol DG1022) with frequency ranging from 1 to 5 kHz, and voltage varying from 1 to 5 Vpp (peak to peak).

The particles, the fluorescent dye, and the electrodes were simultaneously imaged using a Leica SP8 Confocal Laser Scanning Microscope (CLSM). Water (40×, 1.10 NA) and oil (63×, 1.30 NA) immersion objectives were used, while the pinhole was set to 1 Airy unit. The optical properties of particles were selected to avoid significant overlap with the ratiometric dye (SNARF-1). The particles were excited at 405 nm and their emission was collected at wavelengths between 420 and 470 nm. A high-speed resonant scanner (8 kHz) enabled high acquisition rates of up to 28 frames per second at a resolution of 512 × 512 pixels. Two imaging modes were utilized. xyzt mode was used for observation within a given imaging volume, whereas xyt mode was used to image in xy plane at a given height. To measure the pH around a single particle, the acquisition parameters were optimized to balance speed of acquisition with the level of pixel to pixel noise. Once a single particle was located, images of approximately 17×17 μm^2 in size (with a zoom factor equal to 7), were obtained with 512×512 pixel resolution, and frame average of 2. Videos of ten frames were acquired for several particles to quantify statistical significance.

4.3.3 Measuring pH During Operation

Details on the measurement of pH in-operando can be found in Chapter 1. Briefly, pH was mapped by using a ratiometric fluorescent pH indicator, 5-(and-6)-carboxy SNARF-1 (ThermoFisher, C1270). SNARF-1 fluorescent emission presents a shift from yellow-orange to deep red with increasing pH, allowing the pH to be obtained at any point in the experiment through the ratio of dual emissions at two different wavelengths. The ratio of dual emission signals minimizes the effect of fluctuations in focus, excitation intensities, concentration of the dye, and transmittance loss of ITO under electric field, thus proving a more reliable quantification of pH. In these experiments, SNARF-1 (100 μL) was excited at 514 nm, with dual emissions detecting at 580 and 640 nm. After acquisition of images, pH maps were calculated and plotted using an algorithm developed in Igor Pro, following

the formula below:

$$\mathrm{pH} = \mathrm{pKa} - log\left(\frac{R_b - R}{R - R_a} \cdot \frac{I_{b,2}}{I_{a,2}}\right), \tag{4.1}$$

where R represents the ratio of intensities at two detection points, I_1 and I_2, while R_b and R_a denote the ratios of intensities at the basic (I_b) and acidic (I_a) end points. The pH at every z-position was calculated by avering the intensity of the whole frame for each channel. To quantify the pH around particles, the calculations were performed at every pixel of a single frame. To further improve the signal-to-noise ratio, we applied an average convolution filter with a kernel size equal to 5.

4.4 Results and Discussion

4.4.1 EDP Induces $k_\mathbf{B}T$ Scale Pairwise Potentials

Herein, carboxyl-polystyrene particles (CB-PS) are subjected to low frequency ac fields in parallel plate devices as depicted in Figure 4.1. Figures 4.1A shows 3D microscopy images of the electrochemical cell before and 130 s after applying an ac field of 5 V_{pp} and 100 Hz. These images show the view from the x-z plane of the volume between the electrodes (green slabs). The images combine the intensity from SNARF-1 collected at 580 nm (I_{pp}, yellow orange), and at 640 nm (I_{pp}, red) as well as the intensity from CB-PS particles (blue). Once the ac field is applied, the changes in color from SNARF-1 indicate that substantial pH gradients form throughout the cell. In response to the nonlinear pH profile formed between the electrodes, particles migrate toward the position of maximum pH (15 μm from bottom electrode) (138). Particles experience potential wells that are higher than 100 k_BT, so they remain focused while the field is on. As discussed in Chapter 3, if loaded at sufficiently high volume fractions, the particles experience a transition from a disordered liquid into a colloidal crystal. However, even under dilute conditions, particles form aggregates with high local order (Figure 4.1D). This observation reveals that particles not only experience a potential that leads to focusing in the z-direction, but also an interparticle potential that induces clustering even under dilute conditions.

To understand the nature of the interaction between particles at the focusing position, I performed experiments under dilute conditions to favor the formation of small clusters. In these experiments, a pair of interacting particles (a dimer) is first identified and their position recorded. Then, the relative position of the two particles is extracted from videos using image analysis and particle tracking. Figure 4.1E shows examples of trajectories for two interacting particles at the focusing position (15 μm above the electrodes). The histograms of the interparticle distance reveal that, through Brownian motion, particles mostly sample a range of relative positions within 3 particle diameters; however, it is evident that the most likely interparticle distance is at ≈ 4.8 μm (Figure 4.1F). The positional information can be converted into a potential distribution using the Boltzmann equation:

$$P(r) = Ae^{-\phi(r)/(k_B T)}, \tag{4.2}$$

The Boltzmann equation relates the probability, $P(r)$, of sampling interparticle positions to the potential energy landscape, $\phi(r)$, experienced by the particles. A is a normalization constant chosen such that $\int_0^\infty P(r)dr = 1$. Figure 4.1G shows the potential energy calculated from the distribution of interparticle distances (162; 163). The plot shows a potential that is long-range in comparison to electrostatic interactions. Also, notice that the potential wells are only a few $k_B T$ in magnitude, which explains the propensity of the system to assembled into well-organized structures.

4.4.2 Induced Interparticle Potential Depends on Surface Chemistry of Particles

The images in Figure 4.2 compare the state of particles as soon as they arrive at the focusing position and 300 s afterwards. Surprisingly, neither plain PS nor silica particles form readily discernible structures, in stark contrast to the CB-PS particles. All types of particles reach the focusing point but differ drastically in how they behave once there. To gain further insight, I calculated the radial pair distribution function ($g(r)$), which is mathematically defined as follows:

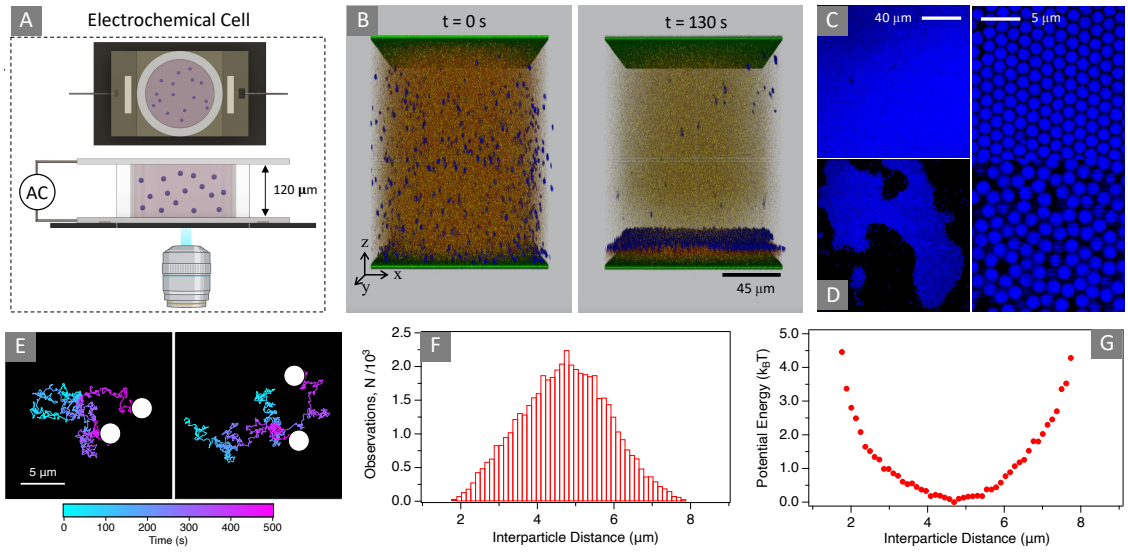

Figure 4.1: Charged particles exhibit strong in-plane pairwise interactions under electrodiffusiophoresis. (A) Schematic of the experimental setup. Panel B show confocal images of the volume between the electrodes (green slabs) before and after 130 s of applying an ac field (100 Hz and 5 V_{pp}). Particles (blue) focus tens of microns from the bottom electrode, where the pH changes most rapidly. (C) Particles at higher volume fraction (2.6%) form crystals at said focusing point. (D) But even for dilute suspensions, particles form aggregates of low order. (E) Trajectories of dimers at the levitation position.

$$g(r) = \frac{A}{2\pi r N} \sum_i \sum_{i \neq j} \delta(r - r_{ij}) \tag{4.3}$$

where N is the number of particles, A is the area, and δ is the delta function. The radial pair distribution function quantifies the probability of finding a particle at a distance, r, from a reference particle, normalized by the uniform distribution of an ideal gas. Consequently, $g(r)$ quantifies the extent a structure deviates from complete randomness. The $g(r)$ for PS shows the behavior of an ideal gas since it remains constant with a value near 1. Consequently, the positions of PS particles are uncorrelated. The $g(r)$ of silica particles display a large peak that decays rapidly with distance, reminiscent of a fluid-like structure with weak interactions. The positions of silica particles, albeit more correlated than for PS particles, display only short-ranged correlations. In stark contrast to the previous cases, the CB-PS particles display regular peaks that decay with distance, also confirming the presence of strong interactions. At the limit of low density, $g(r)$ is linked to the potential of mean force (w) as follows, $g(\vec{r}_1, \vec{r}_2) = e^{\frac{w(\vec{r}_1, \vec{r}_2)}{k_B T}}$ (164; 165). Therefore, we can infer that the range of the

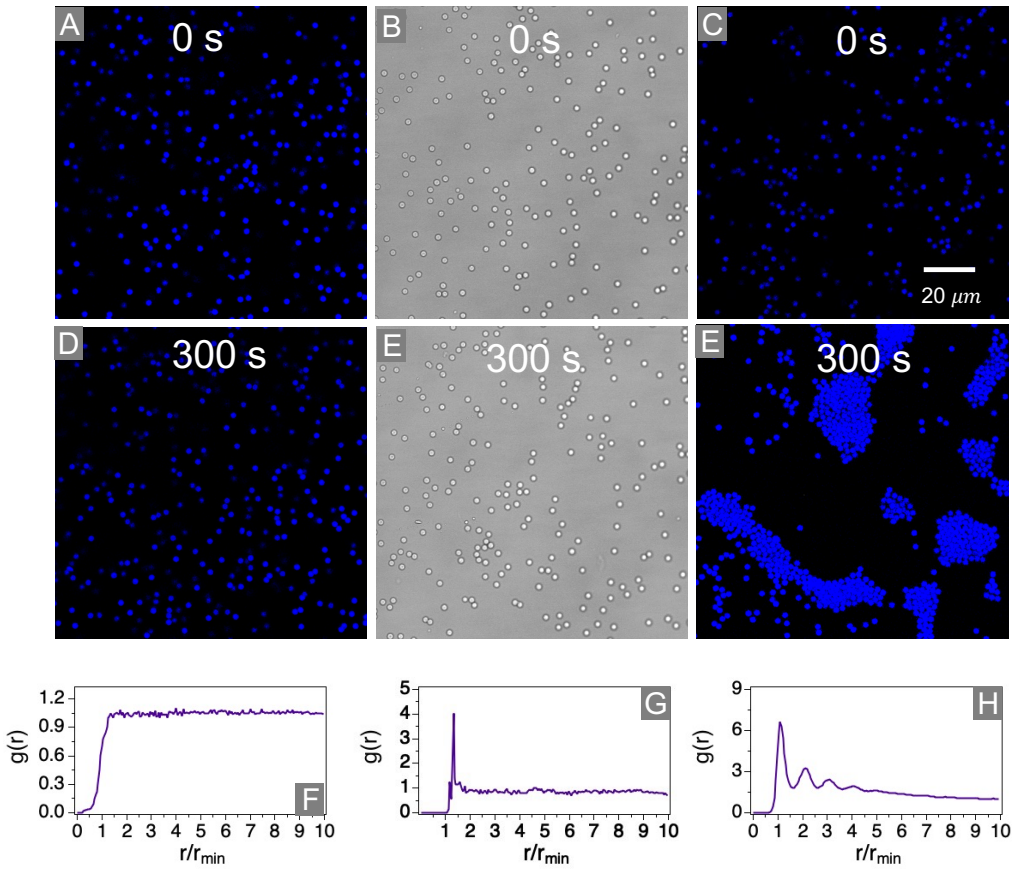

Figure 4.2: Surface chemistry impacts the resulting interparticle potential under EDP. (A-C) Images of silica as well as plain and carboxylate polystyrene particles immediately after reaching the levitation point. (D-F) Images after 300 s at the levitation position. (G-I) Pairwise radial distribution function, $g(r)$, for the different particles. Surface chemistry determines wether the particles are found in the gas, liquid or solid states. Particles had similar sizes and zeta potentials.

interparticle potential for PS and silica particles is much shorter than for CB-PS.

The contrasting behavior of the silica, PS, and CB-PS particles is puzzling. The difference in behavior for seemingly similar dielectric particles has been at the center of a long-standing debate in colloidal electrokinetics. For exampleed, similar experiments, but at higher frequencies (800 Hz), have shown that silica particles aggregate, whereas PS particles remain separated from each other. Also, the types of ions present in the media determine whether dielectric particles aggregate near a conductive electrode (135; 166; 167). Recently, Ning Wu and collaborators proposed differences in the conductivity of the Stern layer as the cause (168). According to this hypothesis, the difference in the conductivity

of the Stern layer for silica and PS can lead to electrohydrodynamic flows of contrasting characteristics (extensile vs contractile). Nonetheless, though compelling, this mechanism cannot explain the behavior in this system since the particles are focused far from the electrodes. Consequently, the potential impact of EHD flows diminishes greatly.

4.4.3 EDP Induces Local pH Gradients around Charged Particles

The question to address next is how dielectric particles, with similar amount of surface charges can behave so differently under EDP. To gain further insight into the origin of the interparticle potential, I examined individual particles that are levitating above the bottom electrode. To do so, the sample is diluted to a volume fraction of 5.0×10^{-5} so that only one particle appears in the field of view. The fluorescence intensity from SNARF-1 is imaged using a $40\times$ objective (1.3 NA). The intensity from SNARF-1 at the two wavelengths is converted to pH values using ratiometric analysis. The heat map in Figure 4.3A captures the spatial distribution of pH around a single particle; the colors red and purple represent pH extrema of 7.1 and 7.5. Surprisingly, the pH increases near the particle. The pH profile in Figure 4.3C across the particle shows that there is a significant pH gradient from the bulk solution towards the surface of the particle, with the pH increasing about 0.3 units. The disturbance of pH extends over 2.5 microns from the surface of the particles, which makes it long-range in comparison to the Debye length. Also, notice that pH decays to the bulk values over the same length scale where the interaction potential reaches a minimum value. Figure 4.3B,D show the respective pH map and profile for silica particles. Strikingly, in contrast to CB-PS particles, the pH decreases near silica particles. While there is no observable pH change near PS particles (Appendix C Figure C.1). The change of pH versus the background (ΔpH) depends on the field parameters (amplitude and frequency), the size of particles, and to a less extent, on the conductivity of the medium. Figure 4.3E shows the δpH for CB-PS particles under different voltages. First, it is apparent that pH gradients do not appear in the absence of an applied electric field. When there is no field, the pH near the CB-PS particles equals the bulk's, 7.2. However, even at voltages as low as 1 V_{pp},

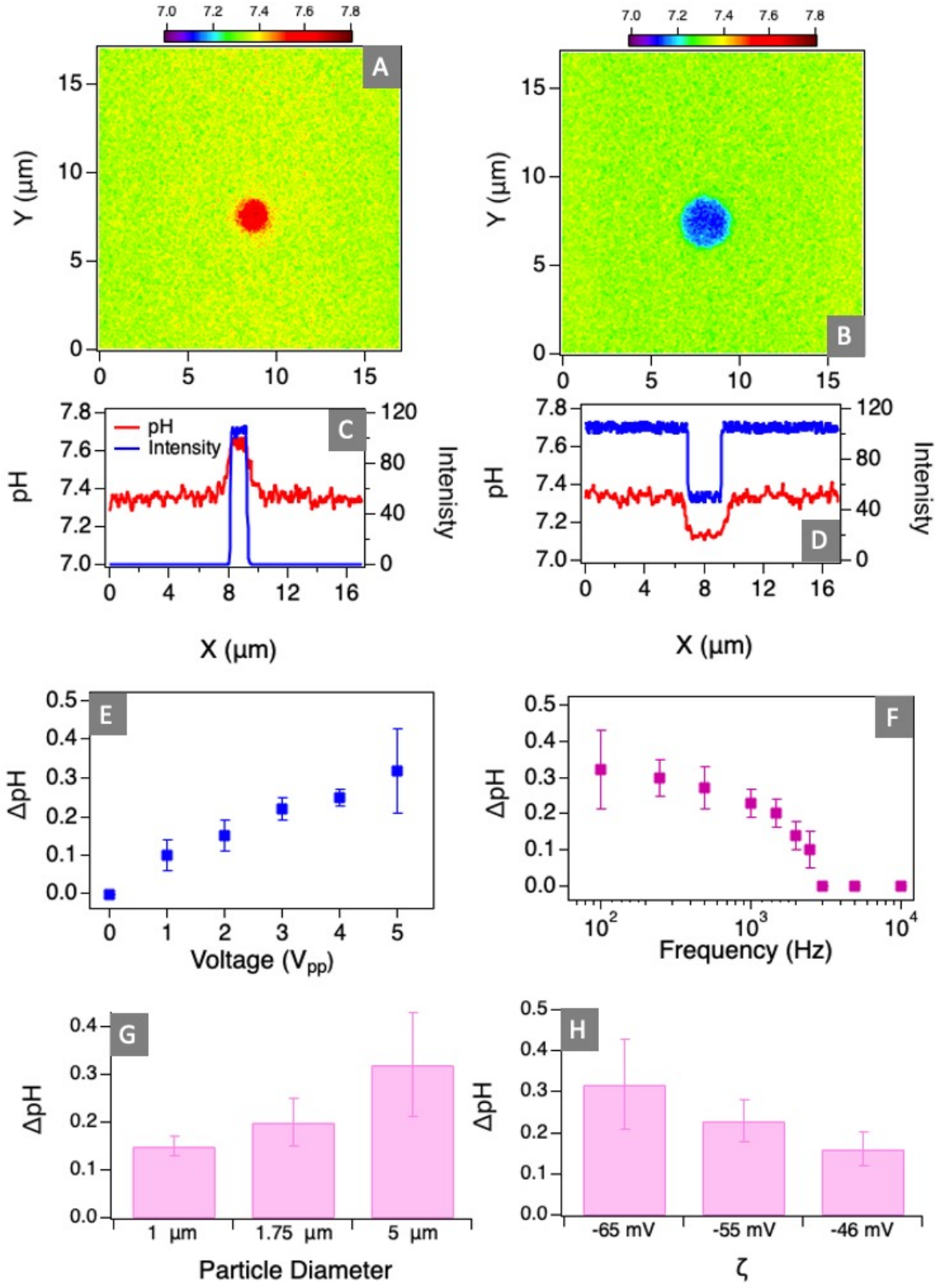

Figure 4.3: The presence of a negatively charged colloidal particle affects the pH distribution in the x-y plane at the focusing height. Panel A and B depict 2-D heat maps that condenses the pH and distribution at all x-y positions. Notice how pH increases around the particle. Panel C and D show the pH profile and particle intensity along the x-axis at y = 7.5 μm. The pH in the vicinity of the particle increases by $\approx$0.3 units in comparison to the background. (E-H) summarizes δpH as a function of voltages, frequencies, particle size and particles zeta potential respectively.

the pH changes substantially near the surface of the particles. Increasing the voltage from 1 to 5 V_{pp} leads to a drastic change in pH. Experiments at different frequencies (Figure 4.3F) show the gradients of pH remain relatively constant between 0.1 and 1 kHz, and quite remarkably, the pH gradients appear at frequencies as high as 3 kHz. Therefore, the frequency window to manipulate this phenomenon extends over a few kilohertz. The ΔpH correlates with the size of particles. For 1 μm particles, $\Delta pH \approx 0.15$, while for 2 μm and 5 μm, ΔpH are approximately 0.2 and 0.3, respectively.

To study the effect of zeta potential, CB-PS particles were modified by attaching PEG chains of different molecular weights. The PEG chains controllably modify the charges on the particles by covalently attaching to the carboxyl groups. As a result, the zeta potential decreases as the length of the attached PEG molecules increases. Figure 4.3H indicates ΔpH increases with the magnitude of zeta potential. For example, by changing the zeta potential from -65 to -36 mV, the ΔpH changes from about 0.3 to 0.16, suggesting that the gradient in pH depends on the number of carboxyl groups available. These results reveal that surface chemistry plays an important role in establishing the interparticle potentials under ac electric fields. The surface groups that were tested have one characteristic in common: they all participate in surface proton reactions, albeit with different pKa's. Nonetheless, at the moment, how the local pH gradients are generated is not fully understood.

4.4.4 Interparticle Potential Determines Rate of Assembly

Measuring ΔpH as a function of the size of a cluster reveals that as more particles come together, the pH gradient grows larger (Appendix C Figure C.2). This observation explains why smaller clusters readily migrate towards larger aggregates rather than forming ones of intermediate size. As a consequence, the aggregation process proceeds in a feedback loop, where the driving force intensifies as more particles join a cluster. To analyze the relationship between the pH gradients and the crystallization process, we turn the attention to the kinetics. Figure 4.2 shows the rate of depletion of singlets for experiments under different voltages. To collect this information, the number of singlets was counted for

each frame using image analysis. The size of the frames were 120×120 μm^2, containing approximately 300 initial particles. The figure shows that at the higher voltages (5 and 4 V_{pp}), singlets are depleted within 10 seconds of starting the experiment. When the voltage decreases to 3 V_{pp}, the rate of depletion decreases substantially, reaching steady state with a fraction of singlets of about 20 %. The behavior at 1 and 2 V_{pp} is similar but with higher percentage of singlets at steady state. The steady-state is interesting because it suggest an equilibrium state with equal rates of association and dissociation. A kinetic expression of second order describes the rate of depletion of singlets:

$$\frac{n_1}{n_1^0} = \frac{1}{1+k_E n_1^0 t}. \tag{4.4}$$

In this expression, n_1^0 and n_1 represent the fraction of singlets at time zero and later times (t), while k is the kinetic rate constant.(60; 169; 167) By fitting the data before steady state to this expression, k_E can be obtained for every experimental condition. Figure 4.4 shows that the rate constant displays a sigmoidal shape, similar to the one observed previously for the bond order parameter at high concentrations (Figure 3.8 B). When compared to the induced ΔpH around individual particles, it can be observed that the kinetic rate constant follows a similar dependence on voltage. The ΔpH shows a substantial change between 3 and 4 V_{pp}, although less steep than for the kinetic rate constant. The qualitative resemblance between the dependence of the rate constant and ΔpH with voltage reflects an outstanding connection between local pH around particles and the assembly process.

4.5 Conclusions

In this chapter, the driving force behind the particles phase transition at the focusing position away from the electrode observed in Chapter 3 was investigated. By using the ratiometric pH visualizing strategy developed in Chapter 2, I observed a local pH gradient surrounding CBPS colloidal particle in xy plane. This induced pH gradient gave rise to a diffusiophoretic potential. The local pH gradient is heavily dependent on the particle surface chemistry properties. For CBPS, a positive pH disturbance is induced while for silica

particles, there is a negative pH disturbance surrounding the particle. In addition, the local pH profile can also be modulated by adjusting the applied ac field strength and frequencies, or changing the particle sizes and zeta potentials. The correlation between pH gradient and the particle assembly kinetics suggest that EDP originating from the locally induced pH profile may be responsible for particles assembly.

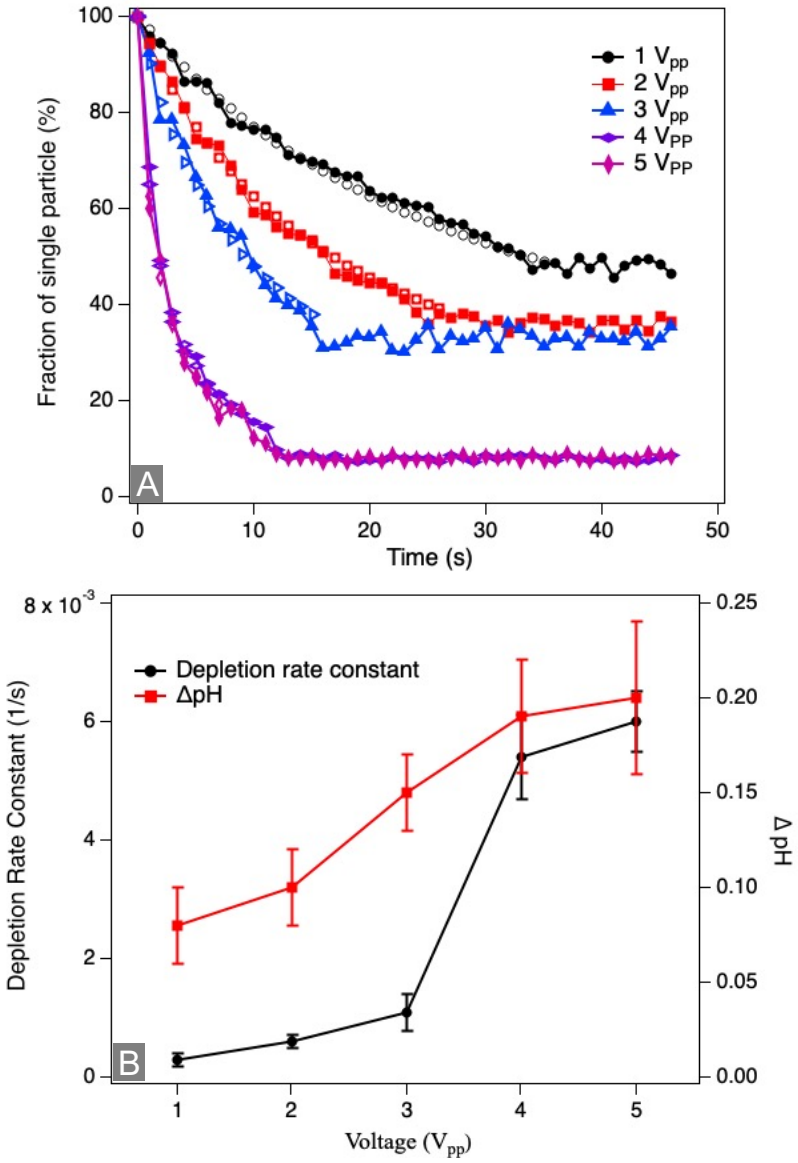

Figure 4.4: The rate of depletion of singlets correlates with the size of ΔpH. (A) Fraction of free particles as a function of time, for different voltages. The higher voltages lead to faster depletion of free particles and lower fraction of singlets at steady state. The voided circular curves plot the corresponding fitting curves following Eq 4.4 at different voltages. k_E is obtained through fitting the data before the fraction of singlets level off. (B) The rate of depletion (black circles) follows similar trends to ΔpH (red squares) as the voltage increases. Therefore, the kinetics of aggregation is directly impacted by the pH gradients induced around the particles and their clusters. Experiments were performed at 100 Hz.

CHAPTER 5

Conclusions and Future Work

In this dissertation, I explored the electrokinetic transport and directed assembly under electric fields and the induced concentration gradients. The induced concentration gradients can be accurately mapped using ratiometric analysis. Fast multichannel imaging of LSCM enables the simultaneous visualization of colloidal transport and quantification of pH distribution.

In Chapter 2, I studied the response of colloidal particles under the coupling of dc fields and the induced pH profiles. The results reveal that a dramatic pH gradient is formed between two planar electrodes separated by approximately 120 μm at dc currents between 0.15 and 4.5 A/m^2. It was further discovered that particles accumulate at positions where the pH gradients are steepest. Qualitative numerical analysis agrees with the hypothesis that the accumulation of particles away from both electrodes is mainly resulted from the diffusiophoretic contribution originating from the shape of the electrochemically generated pH profiles.

I extended the study into ac fields to study the effect of aperiodic EDP on colloidal long-range transport and directed assembly in Chapter 3. Significant pH gradients with a pH maximum occurring as far as 15 μm from the bottom electrode can be formed with low frequency ac fields. Transport analysis suggests that the induced pH profiles originate from the electrolysis of water under oscillating currents. The induced pH gradients promote particles to migrate towards and ultimately focus at the maximum pH position. Furthermore, by increasing the particle volume fractions, particles assembled into highly organized hexagonal crystal structures.

The aim of Chapter 4 was to study the physical mechanism behind particle phase transition at the focusing position. The results revealed that a pH gradient as large as 0.3 units was formed around each particle. I also discovered that changing surface chemistry lead

to different local pH profiles. CB-PS particles with carboxylate surface groups induce a positive pH gradient while non-functionalized PS and silica particles induce no gradient and negative gradients respectively. The induced pH gradients correlate with particles aggregation kinetics at different voltages. This correlation supports the hypothesis that EDP in the xy plane drives the particles to aggregate with each other and display a transition from disorder to order.

Based on these results, future work can be focused on two aspects. The origins of the local pH gradients in the xy plane near the particle need to be studied theoretically. Although, I have successfully observed pH profiles and showed that this pH profile can be modulated by tuning the filed parameters, how this pH gradient is generated still remains unknown. This study can be done experimentally and through numerical simulation.

The pH gradients formed throughout the electrochemical cell provide new possibilities to control the colloidal response. For example, light addressable electrode (LAE) has been used to control the pH gradients generated through water electrolysis in the xy plane (170; 171; 172). The results in Chapters 2 and 3 show that colloidal particles in our system are controlled by the induced pH gradient. Thus, by employing LAEs, I can not only control the particle motion in Z direction throughout the cell but also particle motion and assembly in the xy plane. Another example is to use Janus particles with both silica and CB-PS surfaces. Since the pH profiles induced by the CB-PS and silica side are opposite to each other, the Janus particles may provide further implications for the general field.

Appendix A

Additional Insights into EDP

A.1 Visualization of pH Using fluorescein

As an alternative probe, fluorescein sodium salt, provide further insights on the electrochemical behavior of the system. Figure A.1 shows a 3D confocal image of a section of the electrochemical cell, before and after applying 4.5 A/m^2. The green slabs represent the electrodes, while the blue signal represents the emission from fluorescein. After applying the current, the intensity from fluorescein decreases dramatically near the anode (bottom electrode), but it increases rapidly starting at around 60 μm; the intensity levels off near the cathode. The quenched intensity indicates acidic pHs, while the high intensity indicates basic environments. Although fluorescein (pKa $\approx$ 6.4) is not a ratiometric dye, the experiments display similar features as those with SNARF-1.

A.2 Heat Maps of pH Profiles and Particle Intensity

Experiments with suspensions of different initial pHs (Figure A.2 and A.3) confirm that even when we apply the highest current (4.5 A/m^2), particles do not migrate away from the electrodes in the absence of steep gradients in pH. When the initial pH is 6.5, the system does not develop a transition from acidic to basic pH, and the particles slowly deposit on the bottom (anode) electrode. In contrast, when the initial pH is 8.5, particles do accumulate away from the electrodes, although at a much lower rate.

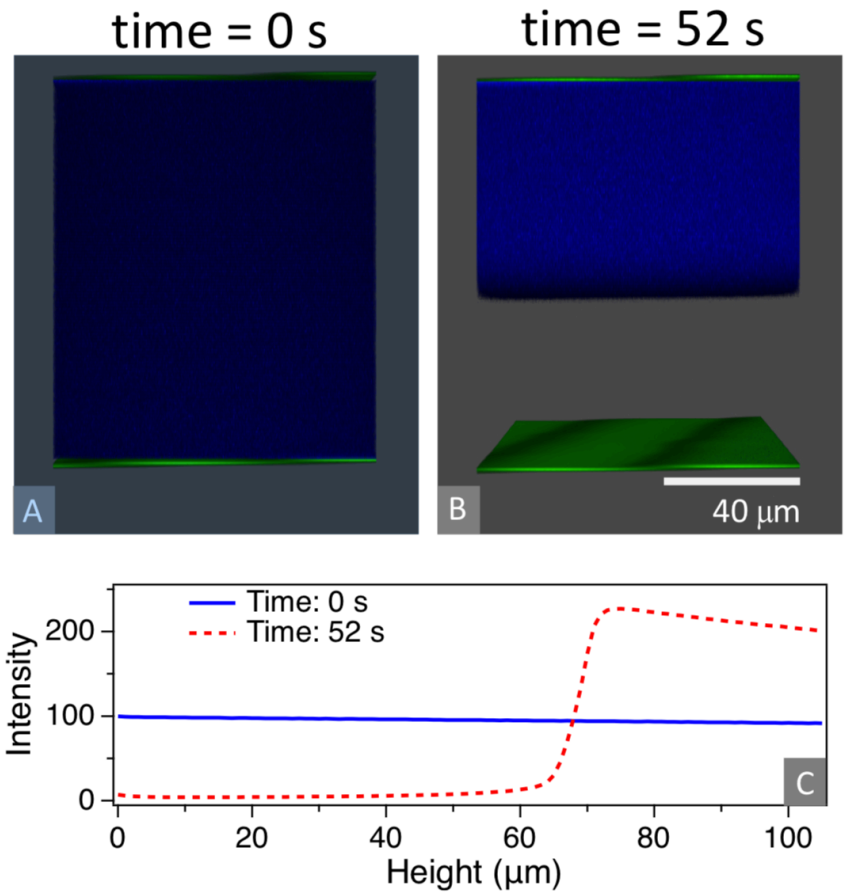

Figure A.1: Experiments with Na-Fluorescein (blue) reveal similar profiles as those with SNARF-1. (A-B) Images show the volume between the electrodes (green) before and after applying 4.5 A/m^2 for 52 seconds. (C) The intensity profile of Na-Fluorescein (blue) can be qualitatively correlated to values of pH within the experimental cell. Near the anode (bottom) the intensity decreases dramatically due to acidic pH values.

Figures A.4 and A.5 juxtapose the pH maps and the fluorescence intensity maps from the experiments studying the response of particles (Figure 2.4). The figures provide two important insights. First, steep changes in pH are needed for particles to migrate away from the electrodes. Second, the peaks in fluorescence intensity from the particles occur exactly at the same position where the gradient of pH is highest.

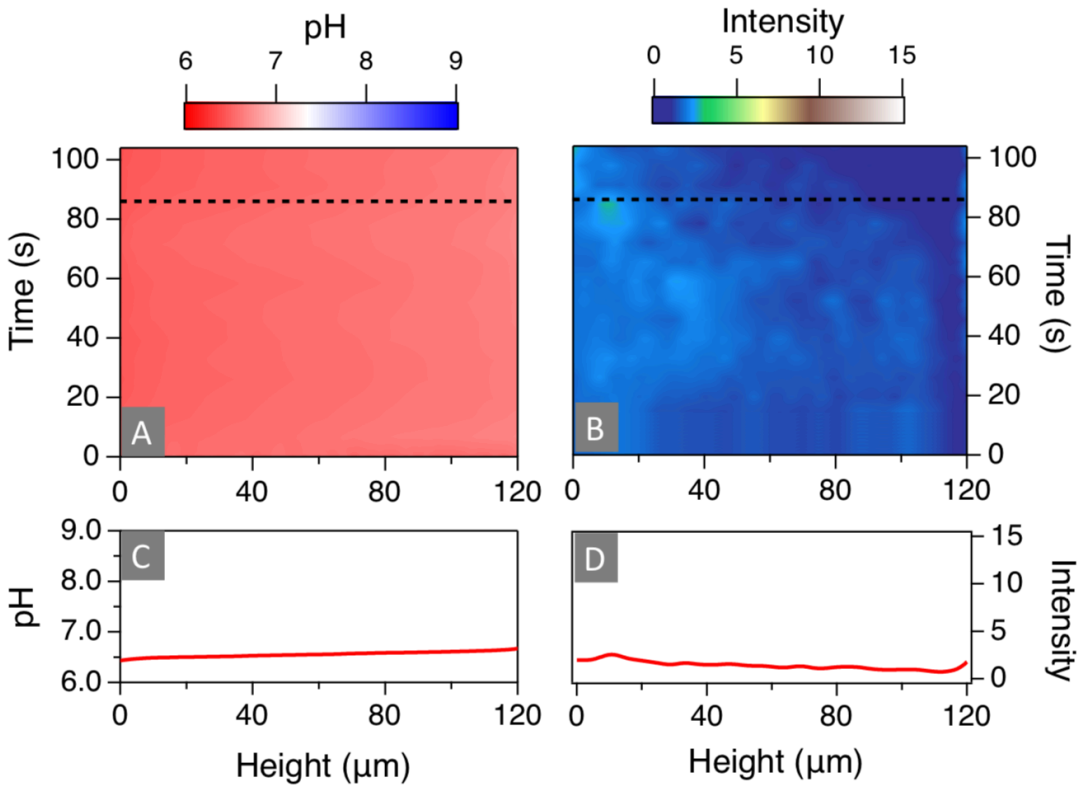

Figure A.2: Juxtaposition of the pH map and the particle intensity map for experiments with initial pH6.5. Panels A-B are 2D heat maps that condense the pH profiles and the fluorescence intensity from the particles for all times in a single experiment, while Panels (C-D) represent the pH and intensity profile for a single time (86 s), indicated by the dashed lines. A current of 4.5 A/m^2 was applied, while the average zeta potential of the particles was -34.6 ± 1.6 (10 kDa PEG-PS). Notice how steep gradients in pH are absent when the initial pH is sufficiently acidic. In this case, particles barely move and there is neither accumulation at the electrodes nor elsewhere ‘.

Figure A.6 shows how the pH profiles are affected by the conductivity of the suspension. At low concentrations of NaSCN, there is no significant change in the pH profile; however, at or above 90 mM there are significant changes in pH profiles, the biggest pH gradient appears close to the top electrode. The magnitude of pH gradients also decrease with increasing NaSCN concentration.

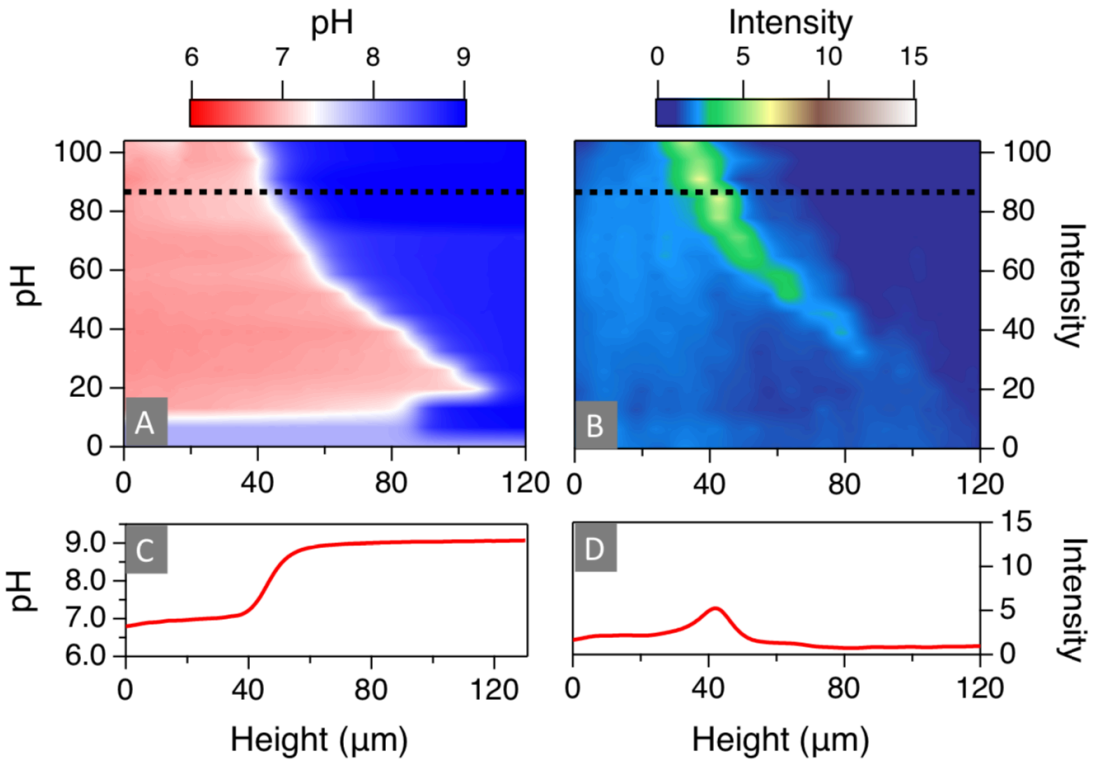

Figure A.3: Juxtaposition of the pH map and the particle intensity map for experiments with initial pH of 8.5. Panels A-B are 2D heat maps that condense the pH profiles and the fluorescence intensity from the particles for all times in a single experiment, while Panels (C-D) represent the pH and intensity profile for a single time (86 s), indicated by the dashed lines. A current of 4.5 A/m2 was applied, while the average zeta potential of the particles was -34.6 ± 1.6 mV (10 kDa PEG-PS). In contrast to acidic initial pH, a steep gradient still forms at basic pH 8.5. In this case, particles accumulate at positions where steep gradients occur.

A.3 Calculations of EDP Velocity and Criteria for Focusing.

Figure A.7 shows the experimental concentration profile for $H^+$and OH^-, for current density of 4.5 A/m^2. B shows a velocity profile calculated using Eq 2.6 and 2.7 in the main text, for the same experiment. The calculations show encouraging features that are in qualitative agreement with the experiments. First, the EDP velocity changes throughout the cell. The velocity is higher close to the cathode ($\approx 6m/s$), while it is almost zero near the anode. Second, there is a point of zero velocity in the middle of the cell, where the gradient in pH is largest. Accumulation of particles and focusing occurs at this point. Nonetheless, the acceleration of the particles before coming to a stop seems higher than what is observed in the experiments. Also, given the factor $1/n_B^0$ in eq 2.7, the values of velocity are quite

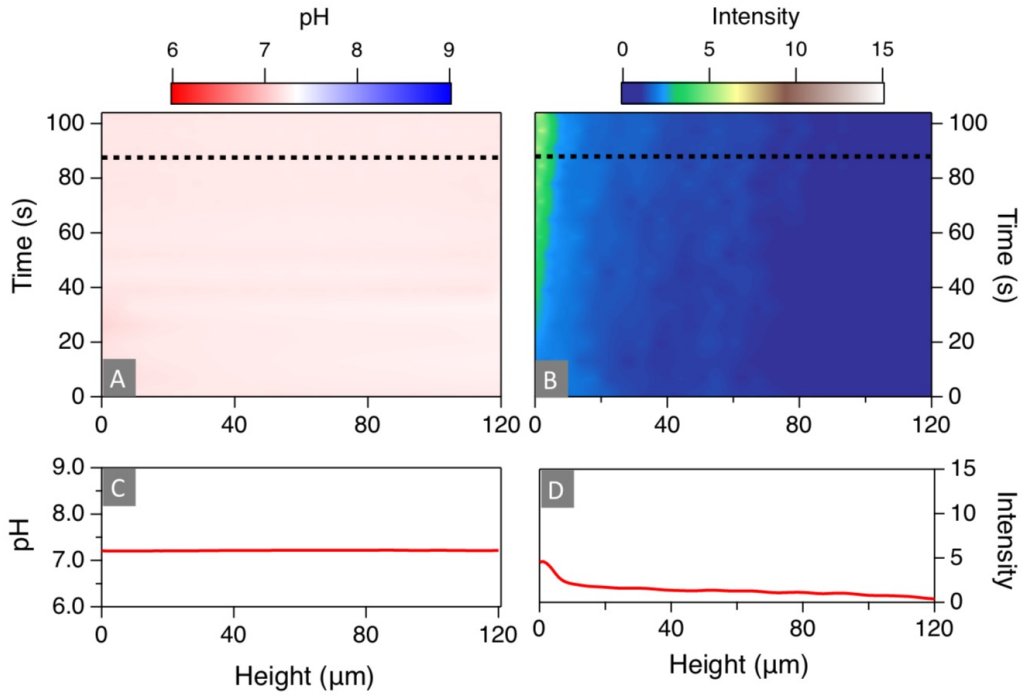

Figure A.4: Juxtaposition of the pH map and the particle intensity map for experiments in Figure 2.4 in chapter 2. Panels A-B are 2D heat maps that condense the pH profiles and the fluorescence intensity from the particles for all times in a single experiment, while Panels (C-D) represent the pH and intensity profile for a single time (86 s), indicated by the dashed lines. A current of 0.15 A/m^2 was applied, while the average zeta potential of the particles was -34.6 ± 1.6 mV (10 kDa PEG-PS).

sensitive to the concentration of background electrolyte. In general, the value of velocity decreases with higher concentration of background electrolyte, like in the experiments.

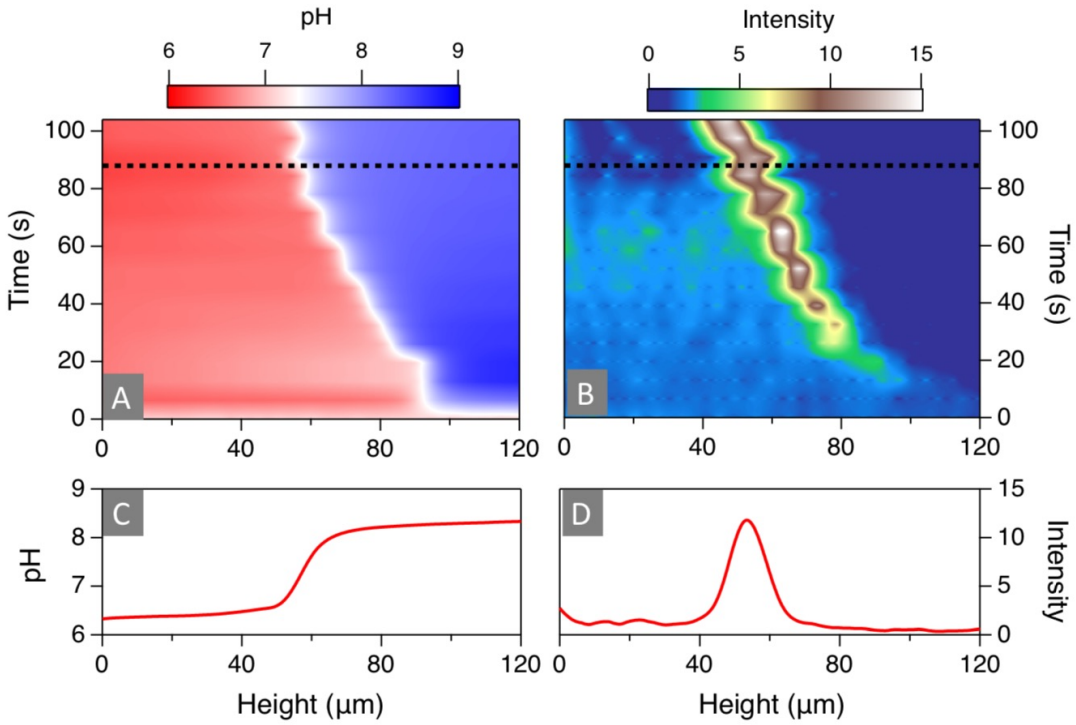

Figure A.5: Juxtaposition of the pH map and the particle intensity map for experiments in Figure 2.4 in chapter 2. Panels A-B are 2D heat maps that condense the pH profiles and the fluorescence intensity from the particles for all times in a single experiment, while Panels (C-D) represent the pH and intensity profile for a single time (86 s), indicated by the dashed lines. A current of 4.5 A/m^2 was applied, while the average zeta potential of the particles was -34.6 ± 1.6mV (10 kDa PEG-PS).

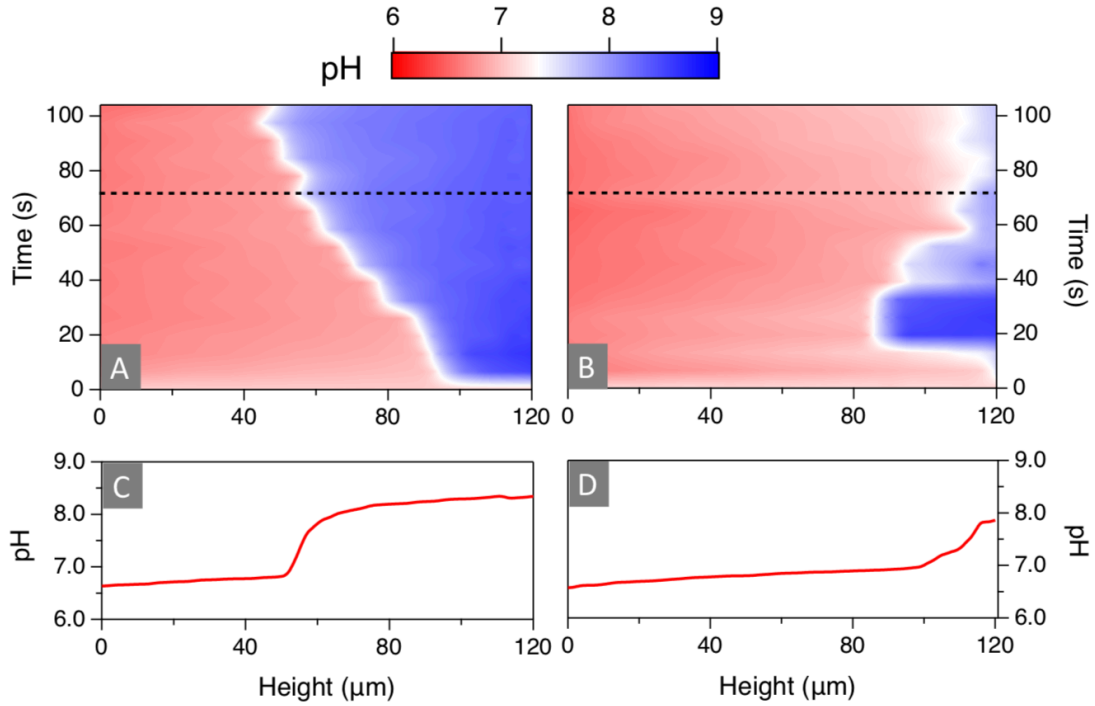

Figure A.6: pH map for experiments in Figure 2.6 of the main text. In this system, the solutions contain different concentrations of NaSCN, 0.1 and 90 mM. Panels A-B are 2D heat maps that condense the pH profiles and the fluorescence intensity from the particles for all times in a single experiment, while Panels (C-D) represent the pH and intensity profile for a single time (72 s), indicated by the dashed lines. A current of 4.5 A/m^2 was applied, while the average zeta potential of the particles was -28.8 ± 1.0 mV (30 kDa PEG-PS) and with initial pH7.2.

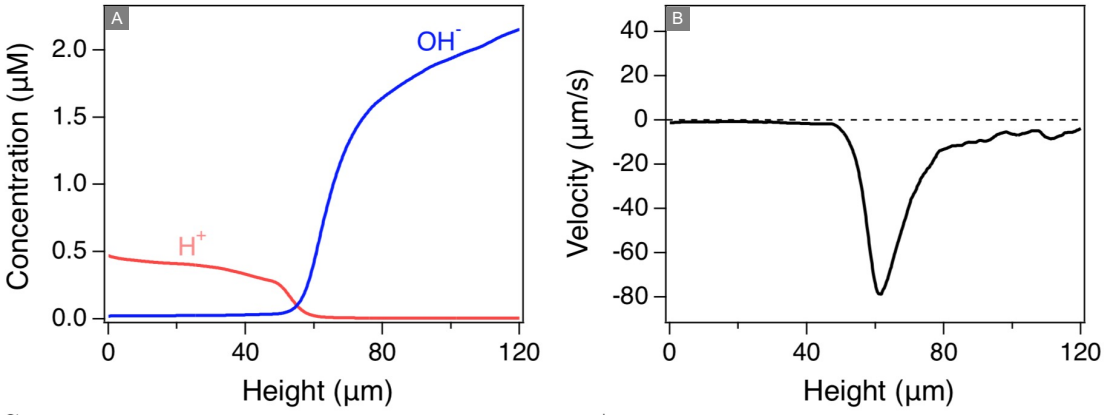

Figure A.7: A) Experimental concentration profile for H^+ and OH^- , for a current density of 4.5 A/m^2; and B) Velocity profile calculated using eq 2.6 and 2.7 in the main text.

Appendix B

Additional Insights into Aperodic EDP

B.1 Heat Maps of pH and Particle Intensity

Figures B.1-7 provide the heat maps for pH and intensity profiles that support the discussion in Section 3.4 of chapter 3. These figures demonstrate that highly nonlinear—and divergent—pH profiles are essential to observe focusing of particles. When solutions are made highly acidic or basic, or when the solution is buffered, changes in pH are minimal. We did not observe focusing in any of those cases.

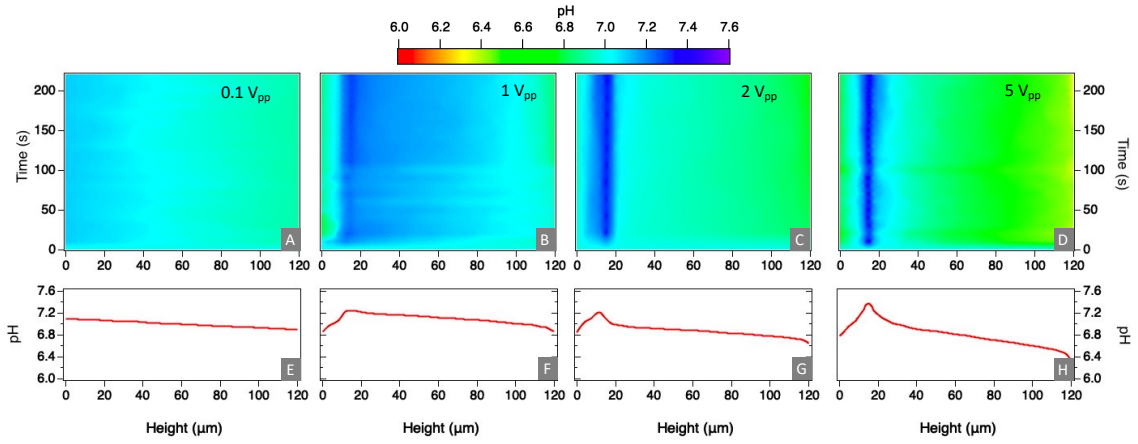

Figure B.1: Comparison of pH profiles under different voltages. Panels (A-D) are 2D heat maps that show the established pH profiles during an experiment, while Panels (E-H) represent the pH profiles at the end of the experiment (220 s). The applied voltages were 0.1 (A, E), 1 (B, F), 2 (C, G) and 5 Vpp (D, H). The frequency was kept constant at 100 Hz. This data shows that higher voltages lead to more nonlinear pH profiles.

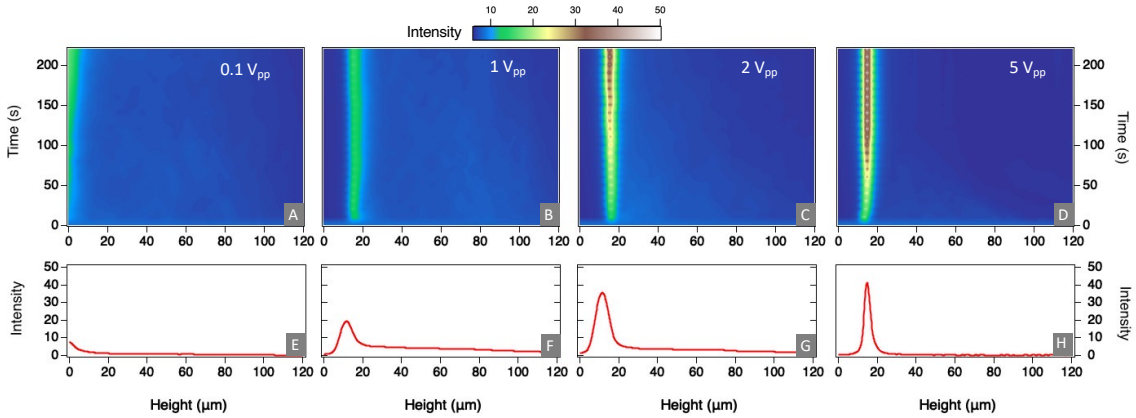

Figure B.2: Comparison of electrokinetic response of charged particles (-65.5 $\pm$ 1.6) under different voltages. Panels (A-D) are 2D heat maps that show the established intensity profiles during an experiment, while Panels (E-H) represent the intensity profiles at the end of the experiment (220 s). The applied voltages were 0.1 (A, E), 1 (B, F), 2 (C, G) and 5 Vpp (D, H). The frequency was kept constant at 100 Hz. The rate of migration of particles towards the focusing position is strongly dependent on the applied voltage and the magnitude of the resultant pH gradients.

B.2 Measurements of Velocity under Aperiodic EDP: Examples of Images and Analysis

Figures B.7-8 show snapshots of cell and average intensity during experiments designed to measure migration velocity under aperiodic EDP. The position of the ensemble of particles is extracted by tracking the maximum intensity within the cell. To construct the curves of velocity shown in Figure 3.6 of chapter 3, two experiments were performed. In one experiment, particles were allowed to sediment at the bottom electrode; in the other, particles sedimented and started from the top electrode. Given the much higher velocity near the bottom electrode, only a volume covering 20 microns in height was imaged to increase the time resolution of the measurements. To measure the downward velocity, the cell was imaged from top to bottom electrodes.

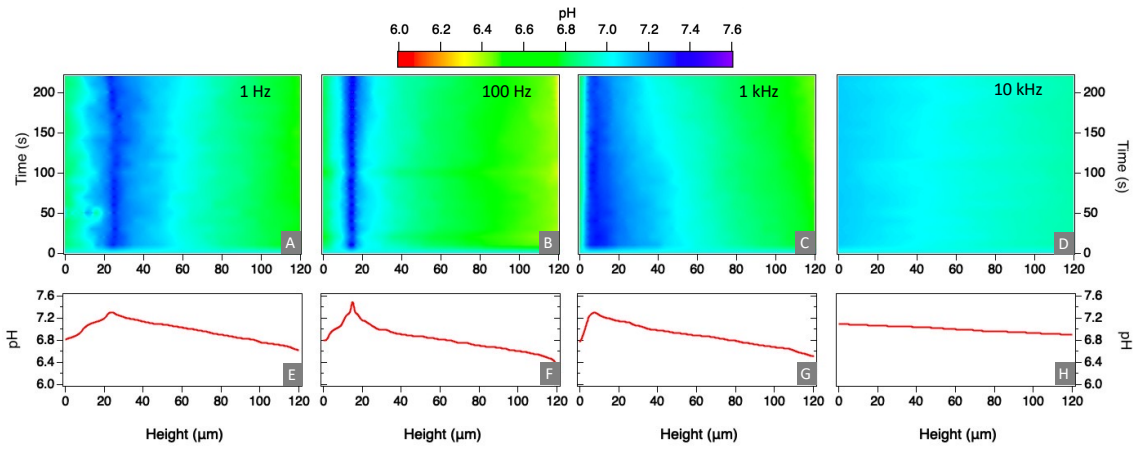

Figure B.3: Comparison of pH profiles under different frequencies. Panels (A-D) are 2D heat maps that show the established pH profiles during an experiment, while Panels (E-H) represent the pH profiles at the end of the experiment (220 s). The applied voltages were 1 Hz (A, E), 100 Hz (B, F), 1 kHz (C, G) and 10 kHz (D, H). The voltage was kept constant at 5 Vpp. This data shows that frequency affects the shape and position of maxima in pH.

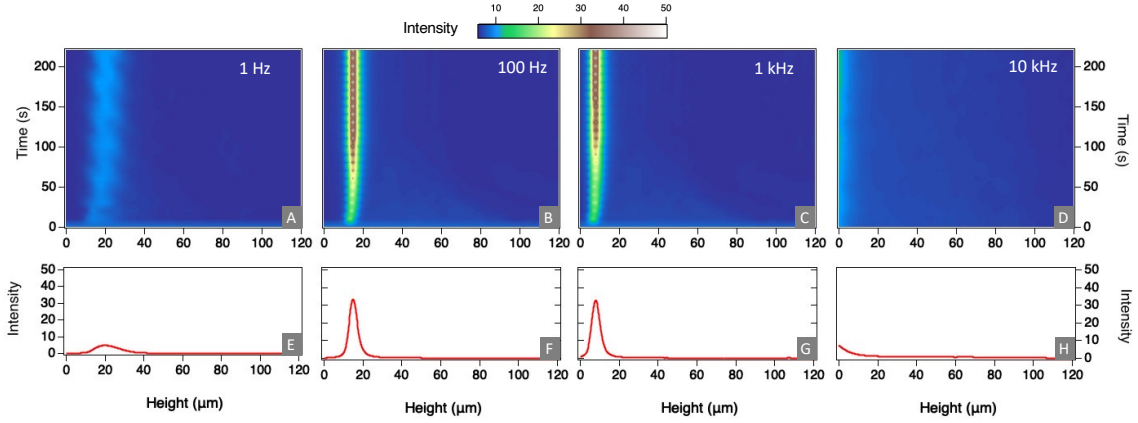

Figure B.4: Comparison of electrokinetic response of charged particles (-65.5 $\pm$ 1.6) under different voltages. Panels (A-D) are 2D heat maps that show the established intensity profiles during an experiment, while Panels (E-H) represent the intensity profiles at the end of the experiment (220 s). The applied voltages were 1 Hz (A, E), 100 Hz (B, F), 1 kHz (C, G) and 10 kHz (D, H). The voltage was kept constant at 5 Vpp. This data shows that frequency affects the position of focusing and the rate of migration. Nonlinear pH gradients cease to form at frequencies above 1.7 kHz.

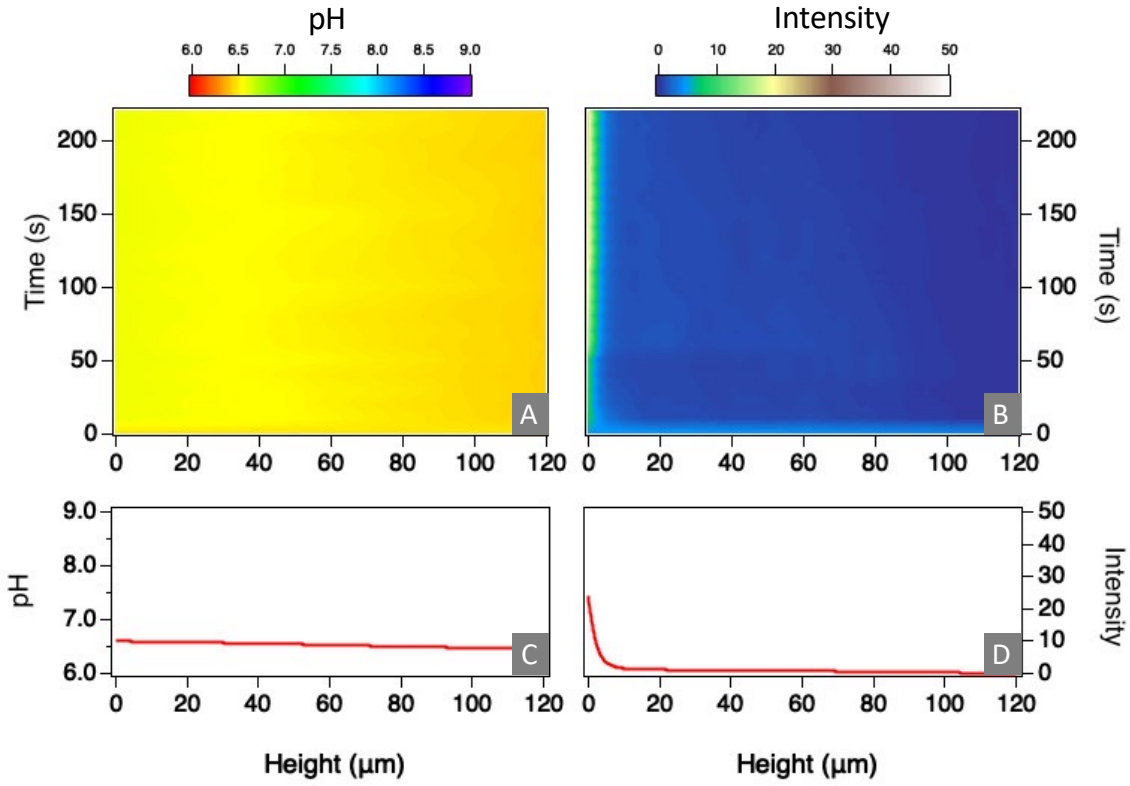

Figure B.5: Juxtaposition of the pH map and the particle intensity map for experiments with initial pH0 $\approx$ 6.5. Panels A-B are 2D heat maps that condense the pH profiles and the fluorescence intensity from the particles, for all times in a single experiment. Panels (C-D) represent the pH and intensity profile for a single time (220 s). The applied signal was 5 Vpp and 100 Hz. Notice how steep gradients in pH are absent when the initial pH is sufficiently acidic. In this case, particles barely move, and the accumulation of particles at the bottom electrodes occurs due to gravity.

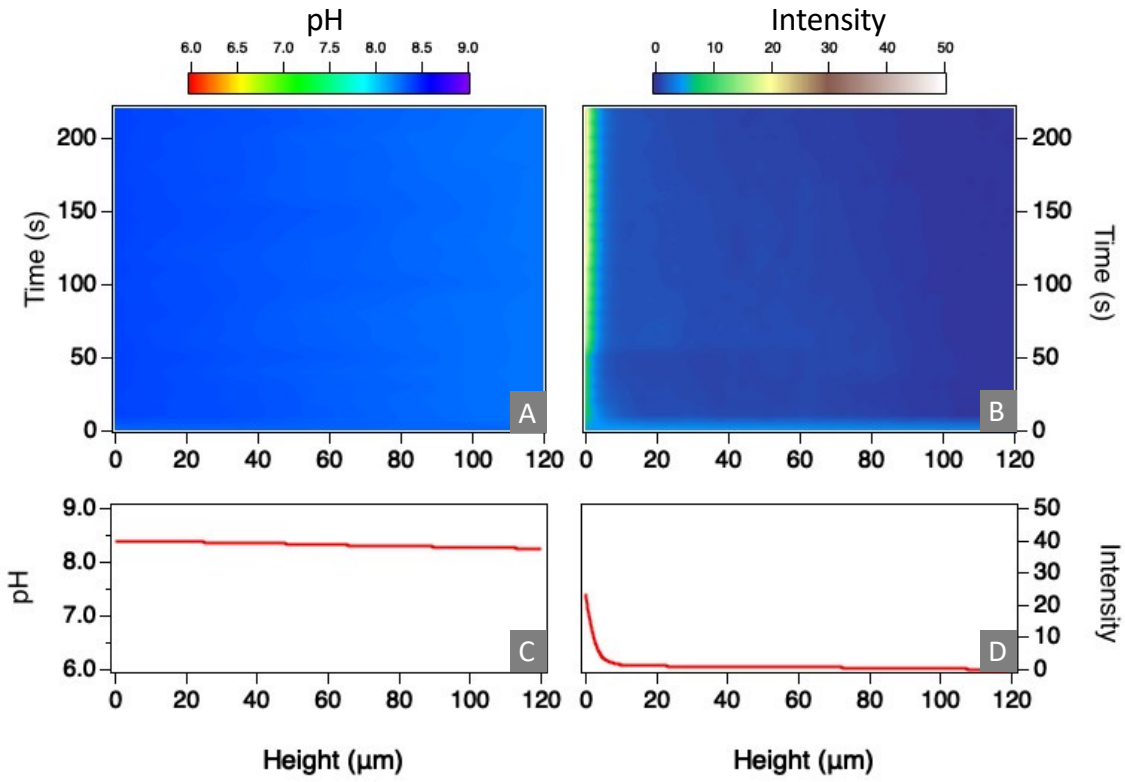

Figure B.6: Juxtaposition of the pH map and the particle intensity map for experiments with initial pH0 $\approx$ 6.5. Panels A-B are 2D heat maps that condense the pH profiles and the fluorescence intensity from the particles, for all times in a single experiment. Panels (C-D) represent the pH and intensity profile for a single time (220 s). The applied signal was 5 Vpp and 100 Hz. Notice how steep gradients in pH are absent when the initial pH is sufficiently acidic. In this case, particles barely move, and the accumulation of particles at the bottom electrodes occurs due to gravity.

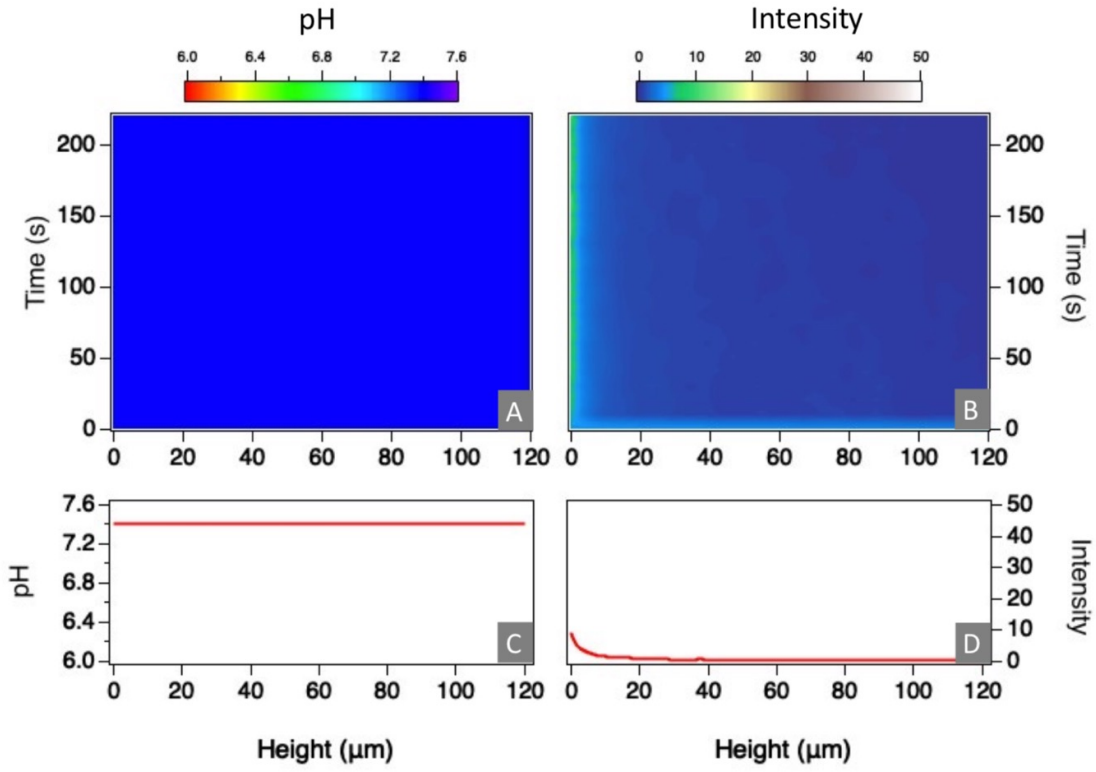

Figure B.7: Juxtaposition of the pH map and the particle intensity map for experiments with PBS buffer and initial pH0 $\approx$ 7.4. Panels A-B are 2D heat maps that condense the pH profiles and the fluorescence intensity from the particles, for all times in a single experiment. Panels (C-D) represent the pH and intensity profile for a single time (220 s). The applied signal was 5 Vpp and 100 Hz. Notice how steep gradients in pH are absent in the presence of a pH buffer. In this case, particles barely move and the accumulation of particles at the bottom electrodes occurs due to gravity. This is evidence that pH gradients are necessary to observed migration and focusing of particles.

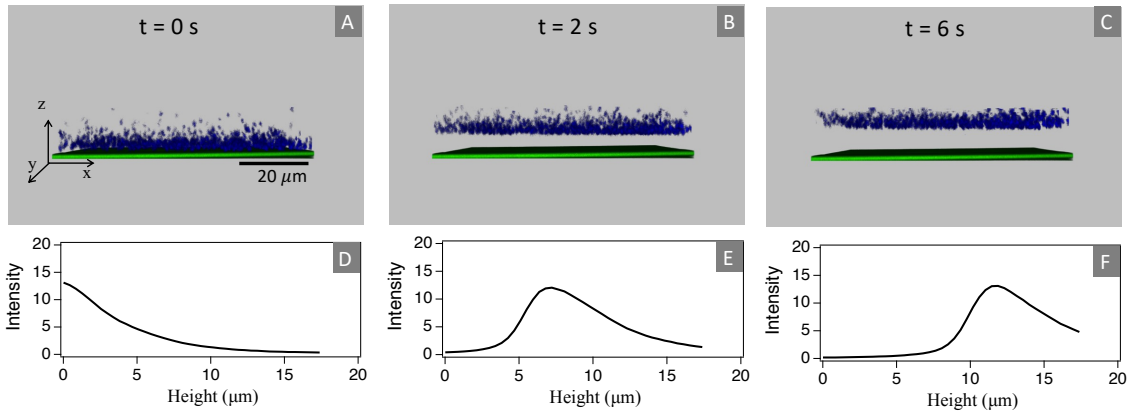

Figure B.8: (A) To measure the upward velocity, particles are allowed to sediment on the bottom electrode for several hours with the field off. Once field is turned on, particles move towards the focusing point (B and C). The average position of the ensemble is estimated by the location of the peak in intensity (D-F). The frequency and voltage in this example are 100 Hz and 5 V_{pp}.

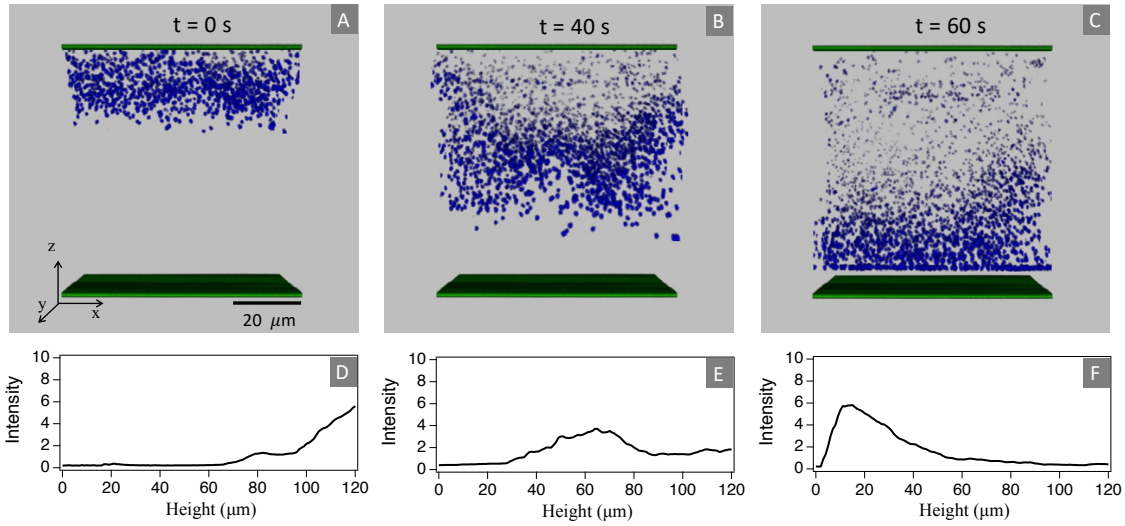

Figure B.9: (A) To measure the downward velocity, particles are allowed to sediment on the top electrode for several hours with the field off. Once field is turned on, particles move towards the focusing point (B and C). The average position of the ensemble is estimated by the location of the peak in intensity (D-F). The frequency and voltage in this example are 100 Hz and 5 V_{pp}.

Appendix C

Additional Insights into Local pH Gradients and Assembly

Figure C.1 exhibits pH distribution surrounding a single PS particle (in the center of the image view) at 5 V_{pp} and 100 Hz ac fields. There is no induced pH gradient surrounding the PS particle.

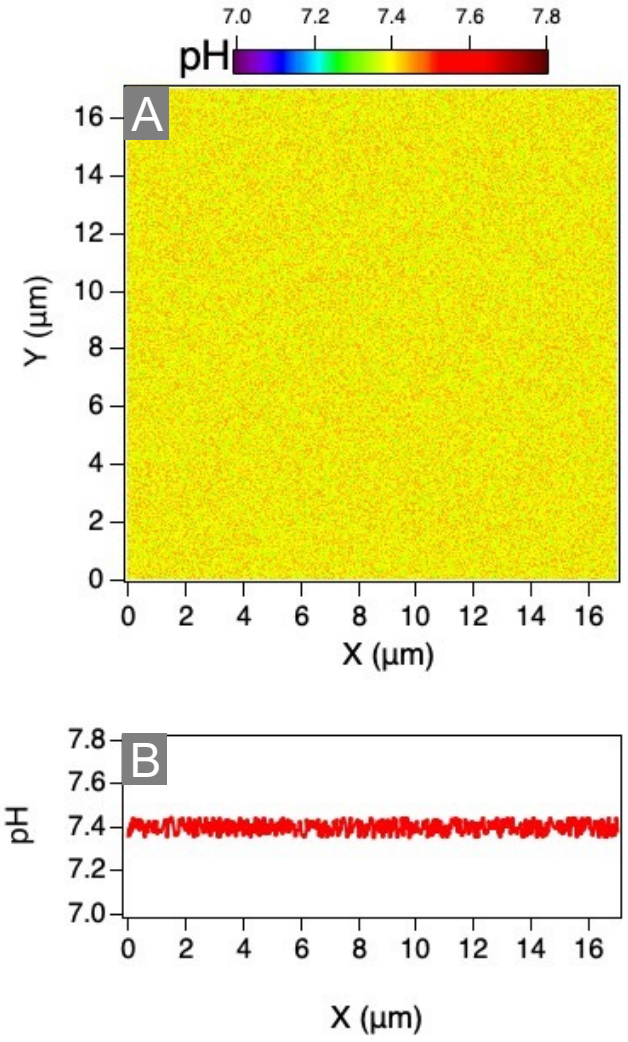

Figure C.1: Panel A depicts a 2-D heat map that condenses the pH distribution at all x-y positions. The particle is placed at the center of the view. Notice how the pH remians unchanged around the negatively charged PS particle. Panel B shows the pH profile along the x-axis crossing the particle.

Figure C.2 displays the evolution of local ΔpH with the growth of aggregation of particles at 5 V_{pp} and 100 Hz ac fields.

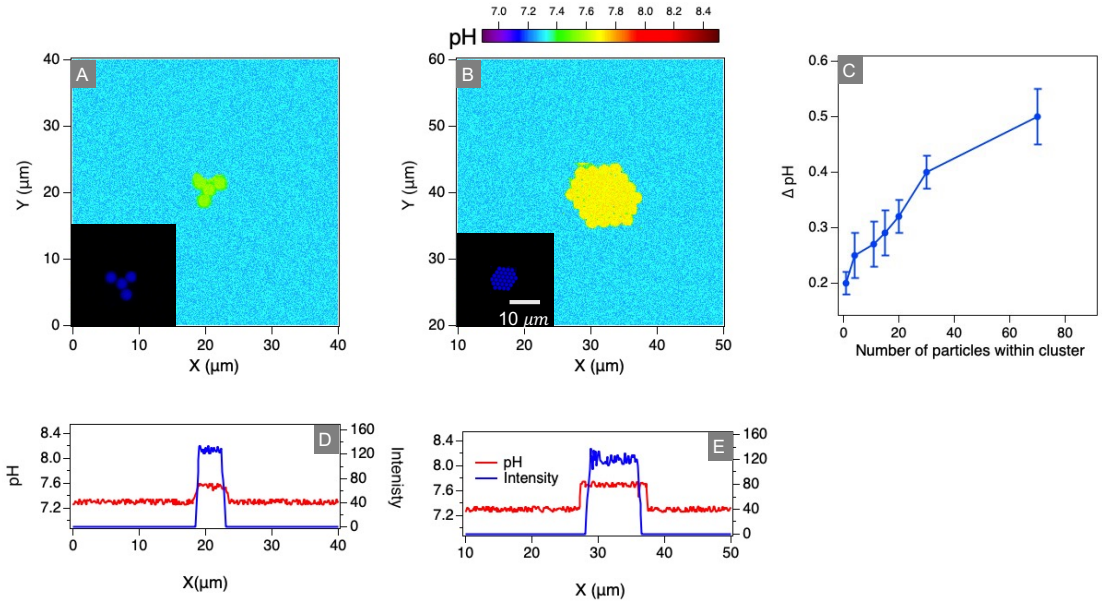

Figure C.2: Panel A-B depict a 2-D heat map that condenses the pH distribution surrounding aggregation of different number of particles at all x-y positions. Panel D-E shows the pH profile (red line) and particle intensity (blue line) along the x-axis crossing the aggregation. Panel C summarizes ΔpH as a function of number of particles within the aggregation. Notice how local ΔpH increases with increasing aggregation sizes.

Appendix D

Modeling pH Gradients under Low Frequency ac Fields

Mass-transport of dissolved species was simulated by solving Nernst-Planck equations assuming no potential gradients with water equilibrium.

$$\frac{\partial C_j}{\partial t} + \nabla \cdot j_j = R_j, \tag{D.1}$$

$$j_j = -D_j \nabla C_j, \tag{D.2}$$

Where C_j, j_j, R_j and D_j are the concentration, flux, reaction and diffusivitty of each species.

Oscillating voltages was accounted for at the bottom electrode, while the top electrode was grounded. The applied oscillating voltage at the bottom electrode is a sinusoidal function of time

$$\phi_s = \phi_0 * \sin(2 * \pi * f * t), \tag{D.3}$$

Where f is the ac signal frequency.

Ionic fluxes were set as the boundary conditions which were determined as following:

$$-n \cdot j_j = \frac{-\nu_j i_{OC}}{nF}, \tag{D.4}$$

Where ν_j is the stoichiometry coefficient and i_{OC} is the local current density at the electrode surface. n is the number of electrons participating in the reaction and F is Faraday constant.

The local electrode current density (i_{OC}) was calculated by linearized Butler-Volmer relation:

$$i_{OC} = i_0 \frac{(\alpha_a + \alpha_c) F}{RT} \eta, \tag{D.5}$$

$$i_0 = i_{0,ref} \prod_{j:\nu_j>0} \left(\frac{C_j}{C_{j,ref}}\right)^{(\alpha_c \nu_j/n)} \prod_{j:\nu_j<0} \left(\frac{C_j}{C_{j,ref}}\right)^{(-\alpha_a \nu_j/n)}, \tag{D.6}$$

Where $i_{0,\,ref}$ is the exchange current density, α_a and α_c are the anodic and cathodic transfer coefficient respectively. R is the universal gas constant and T is temperature. n is the number of electrons participated in the reaction. C_j, $C_{j,ref}$ and ν_j are concentration, reference conventration and stotiometric coefficient of each species. The overpotential (η) was determined by the following equation:

$$\eta = E_{ct} - E_{eq}, \tag{D.7}$$

$$E_{ct} = \phi_{s,exter} - \phi_l, \tag{D.8}$$

Where, $\phi_{s,exter}$ is the external potential and ϕ_l is the electrolyte potential, the equilibrium E_{eq} was determined through Nernst equation accounting for concentration overpotential due to the pH gradient:

$$E_{eq} = E_{eq,ref} - \left(\frac{RT}{nF}\right) ln \prod_j \left(\frac{C_j}{C_{j,ref}}\right)^{(\nu_j)}, \tag{D.9}$$

Where $E_{eq,\,ref}$ is the reference equilibrium potential of water splitting at initial pH of 7 calculated through water Pourbaix plot. α_a and α_c are the anodic and cathodic transfer coefficient respectively. R is the universal gas constant and T is temperature. n is the number of electrons participated in the reaction. C_j, $C_{j,ref}$ and ν_j are concentration, reference conventration and stotiometric coefficient of each species.

The above models was solved in the Comsol electrochemsitry module using the tertiary current distribution, Nernst Planck interface. The Mesh was predefined as extremely fine in the domain with fixed number of 1000 elements near the electrodes. The model was solved as time-dependent up to 20 s after the ac field is applied with time step of 0.1 s. The parameters used to perform the Comsol Multiphysics simulation and calculation of EDP velocity are listed in table E.1 annd E.2 respectively.

The exchange current densities were obtained through the Tafel plot. The x-axis inter-

Table D.1: Parameters used in Multiphysics simulation

Parameter	Symbol and Units	Value
Diffusivity, OH^-	D_{OH^-} (m^2/s)	5.00×10^{-9}
Diffusivity, H^+	D_{H^+}(m^2/s)	9.30×10^{-9}
Exchange Current Density, Anode	$i_{0,ref1}$ (A/m^2)	1.40×10^{-3}
Exchange Current Density, Cathode	$i_{0,ref1}$ (A/m^2)	4.00×10^{-3}
Reference Equilibrium Potential, Redox Reaction	E_{eq} (V)	8.20×10^{-1}
Reference Equilibrium Potential, Oxidizing Reaction	E_{eq} (V)	4.10×10^{-1}
Temperature	T (K)	2.98×10^{2}
Faraday Constant	F (sA/mol)	9.65×10^{5}
Reference Concentration, OH^-	$C_{OH^-,ref}$ (Mol/m^3)	1.60×10^{-4}
Reference Concentration H^+,	$C_{H^+,ref}$ (Mol/m^3)	6.31×10^{-5}
Anodic Transfer Coefficient	α_a	0.50
Cathodic Transfer Coefficient	α_c	0.50
Stoichiometric Coefficient, OH^-	ν_{OH^-}	1
Stoichiometric Coefficient, H^+	ν_{H^+}	1
Number of Participating Electrons	n	1
Initial pH	pH_0	7.2

Table D.2: Parameters used to perform EDP velocity calculations

Parameter	Symbol and Units	Value
Permittivity of Vacuum	$\varepsilon_0(C_2m_2/N)$	8.85×10^{-12}
Rel. Dielectric Constant, H_2O	ε_w	8.00×10^{2}
Elementary Charge	e (C)	1.60×10^{-19}
Avogadro's Number	N_A (1/mol)	6.02×10^{23}
Boltzmann constant	K_B (m^2kg/s^2K)	1.38×10^{-23}
Temperature	T (K)	2.98×10^{2}
Thermal Energy	K_BT (J)	4.11×10^{-21}
Thermal Potential	K_BT/e (V)	2.57×10^{-2}
Viscosity	μ (Pa·s)	1.00×10^{-3}
Diffusivity, OH^-	D_{OH^-} (m^2/s)	5.00×10^{-9}
Diffusivity, H^+	D_{H^+}(m^2/s)	9.30×10^{-9}
M+	s/kg	-1.00×10^{11}
Zeta Potential	$\zeta e/K_BT$ (V)	-2.53
Bulk Concentration	n_0^B(mol/m^3)	0.10

cept of the Tafel plot is the exchange current density. The Tafel plot was obtained through linear sweep voltammetry (LSV) running from -5 to +5 V with the step of 5 mV through our electrochemical device using potentiostat/galvanostat (Metrohm PGSTAT204).

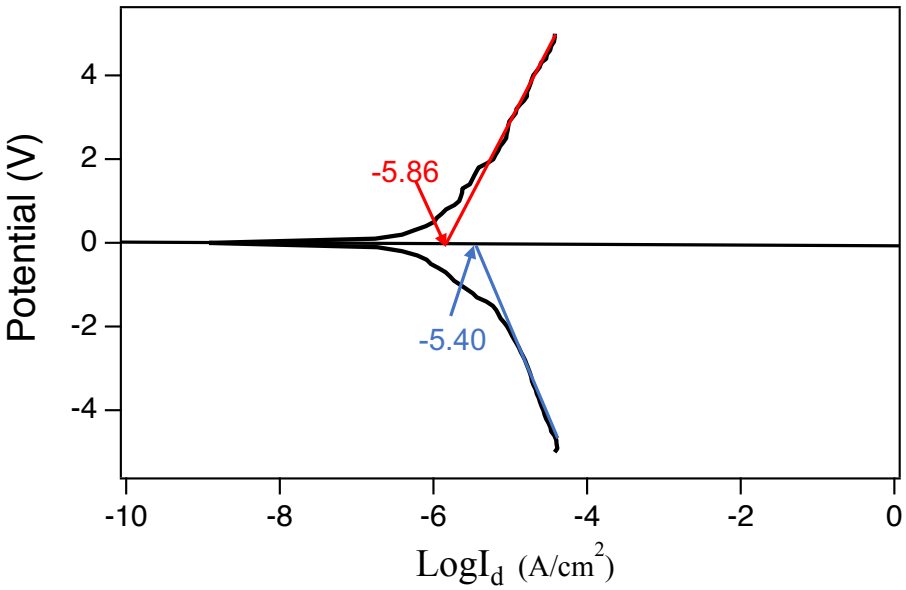

Figure D.1: Tafel plot obtained through LSV . Both the positive and negative Tafel plots were linear fitted (red and blue line). The X-axis intercept, which is log (i_0,ref) was determined as -5.86 (positive LSV) and -5.40 (negative LSV), respectively.

Appendix E

Analysis of Bond Order Parameters

Below is the code used for analysis of bond order parameters developed in MATLAB. The bond order parameters are calculated following the equation below:

$$\psi_6 = i/N[|(1/N_{ij}\sum_j exp(i6\theta_{ij}|] \tag{E.1}$$

Where θ_{ij} is the azimuthal angle between particle i and j, N is the total number of particles, N_{ij} is the number of nearest particles around particle j.

The code calculates the bond order parameters by first identifying and counting the number of nearest particle of each target particle. The second part of the code is to calculate the interparticle distance between target particle and nearing particle. θ_{ij} is calculated in the last part of the code.

```
function [nn, num_nn]=nearest_neighbour(x_particle,
   y_particle)
a=delaunay(x_particle,y_particle); %Performs delauney
   triangulation on the center points of the particles based
    on their x and y coordinates from the first part of
   other code
nn = cell(length(x_particle), 1);
num_nn = zeros(1 , length(x_particle));
for n_tri=1:length(a)
    for index=1:3
        for neighbour=1:3
            if index~=neighbour
                if isempty(nn{a(n_tri,index)}) %looks to see
                    if that specific spot in nn is empty so
                   can be populated
                    nn{a(n_tri,index)}=zeros(1,1); %If it is
                        empty, before doing nearest neighbor
                       , fills that spot in nn with 0 so no
                       longer empty and won't loop through
                       that element again
                    num_nn(a(n_tri,index))=num_nn(a(n_tri,
                       index))+1; %Adds 1 to the number of
                       nearest neighbors for that particle,
                       after which this can happen again for
                        every neighboring particle
                    nn{a(n_tri,index)}(num_nn(a(n_tri,index)
                       ))=a(n_tri,neighbour); %Replaces the
```

```
                        0 value of nn with number that equals
                         a value from beginning of loop when
                        multiplied by paired num_nn value
                    elseif isempty(find(nn{a(n_tri,index)}==a(
                       n_tri,neighbour))) %If the nn cell is
                       already populated, finds where in a the
                       nn value is, essentially for finding more
                        neighbors after the first one is found
                       for a given particle
                        num_nn(a(n_tri,index))=num_nn(a(n_tri,
                           index))+1; %Adds 1 to the number of
                           nearest neighnors for that particle
                        nn{a(n_tri,index)}(num_nn(a(n_tri,index)
                           ))=a(n_tri,neighbour); %Same as line
                           12
                        end
                    end
                end
            end
        end
    end
end
clc; clear;

ScalingMicron = 29; %This is where you input the size of the
    image in  m  to scale the image from pixels to  m
ScalingPixels = 1700;   %This is where you input the size of
    the image in pixels from the microscrope
```

```
Scaling = ScalingMicron/ScalingPixels;

A = imread(['Video_9.tif']); %Reads imported Tif image of
   particles
[x_length, y_length] = size(A);
imshow(A)
[centers, radii, metric] = imfindcircles(A,[30 110],'
   Sensitivity',0.962); %finds the outlines of the particles
    and records the locations of their centers and radii

imshow(A) %Shows the initial image imported
h = viscircles(centers,radii); %plots the circles around
   each particle found in the imfindcircles function
hold on
x_particle = centers(:,1); %annexes the x-coordinates of
   each of the centers of the particles in an array
y_particle = centers(:,2); %annexes the y-coordinates of
   each of the centers of the particles in an array
plant = voronoi(x_particle,y_particle, 'w') %plots the
   Voronoi Diagram, as seen in the white hexagons, on top of
    the circles previously plotted
plant(1).LineWidth = 3; %Increases the linewidth of the
   voronoi diagram so more visible
plant(2).LineWidth = 3;
axis equal
diameter = 2*(mean(radii));%Finds the average diameter of
   the particles
```

```
diamaterMicron = diameter * Scaling;
hold off

%Bond Orientation Order Parameter Code

%Equation for bond orientation order parameter:

%Where psi (bond order) is denoted by variable S and Nij is
   denoted by variable num_nn

[nn, num_nn]=nearest_neighbour(x_particle, y_particle) %
   Calls upon other function to determine nearest neighbors
   of each particle
S=zeros(1,length(x_particle));
Interdist = [];
for cnt1=1:length(x_particle) %Count 1 is a loop
   representing the first sum in the bond order equation
   denoted by sigma i above
    for cnt2=1:num_nn(cnt1) %Count 2 is a loop represemtomg
       the second sum in the bond order equation denoted by
       sigma j above
            h=x_particle(nn{cnt1}(cnt2))-x_particle(cnt1); %
               Distance in the x-direction between
               neighboring particles
            v=y_particle(nn{cnt1}(cnt2))-y_particle(cnt1); %
               Distance in the y-direction between
               neighboring particles
```

```
            Interdist(end+1) = sqrt((h.^2)+(v.^2)); %Finds
               the interparticle distance between
               neighboring particles
            if (h~=0)
                theta = atan(v/h); %Calculating angle
                   between particles of interest by taking
                   inverse tangent of x and y distances
            else
                theta = atan(sign(v)*inf); %If the distance
                   between the particles is 0 in the x-
                   direction, just take the inverse tangent
                   of infinity to find theta, as that is
                   similar
            end
            S(cnt1) = S(cnt1) + exp(sqrt(-1)*(6*theta)); %
               Calculation of part of equation after sigma j
                and adding up for all possible values of
               count 2
        end
        S(cnt1)=S(cnt1)/num_nn(cnt1); %Calculation of part of
           equation after sigma i
end

N = sum([num_nn==6]); % Determine all the particles that
   have 6 nearest neighbours
Savg = 0;
for cnt1=1:length(x_particle)
```

```
    if (num_nn(cnt1)==6) %For each particle that has a
       perfect lattice (6 nearest neighbors), the S value of
        that particle are added to the average to get the
       average S value for these perfect lattices
        Savg = Savg + S(cnt1)/N;
    end
end
Savg=abs(Savg);
InterdistAvg = mean(Interdist); %Finds average interparticle
    distance
InterdistMicron = InterdistAvg * Scaling; %Puts average
   interparticle distance in microns
InterDistDia = InterdistMicron/1.75; %Makes the average
   interparticle distance in units relative to the average
   diameter of teh particles
```

Appendix F

Ratiometric Analysis

Below is the code developed for ratiometric analysis and pH heatmap plotting in Igor Pro. The code consists of three sections. The first section applies the average filter on the raw tiff images. The second section calculates pH values following the calibration equation. The third section condenses the pH profiles along both x axis and y axis into a 2D heatmap.

```
#pragma TextEncoding = "UTF-8"
#pragma rtGlobals=3             // Use modern global access
   method and strict wave access.
#include <Multi-dimensional Utilities>
#include <MatrixToXYZ>

// Earlier versions were restricted to handle only single
   frames of tiff images.

// Update: This code was updated on 2023-07-16 to enable the
    ability to analize stacks of tiff files.
// The new code imports a single tiff stack for the two
   channels and assign them to 3D waves.
// The ratiometric calculations are performed as before.
// The visualization of the stack is performed using the 3D
   Vieving package.

// Update: 2023-07-23 This update enables the aplication of
   an average filter to a 3D stack of images.

//*****************************************************************

Menu "3D pH/Intensity Analysis"
   "Average Filter on Stack", AverageFilter_3DStack()
   "Ratiometric Calibration", SNARF_Calibration()
        "Ratiometric Analysis", Ratiometric_Analysis()
        "Interpolate Matrix", MatrixIntp()
```

```
        "Plot Matrix and Hook",DCursorMoved2()
End

Function AverageFilter_3DStack()

        String mat //Name of 580 nm matrix
        String mat1 //Name of 640 nm matrix
        String Routput
        String Routput1  //Name of interpolated matrix
        String base
        String base1
        Variable nr,nc, nl, ii

        //Prompt mat,"2D 580 nm Matrix Wave (Number of
           layers and chunks must be zero)",popup,WaveList
           ("*_580nm",";","DIMS:2") // use "*_580nm" to make
            it more specific or "*" to show all matrices
        //DoPrompt "Select Matrix to Process and Output name
           .", Mat

        Prompt mat,"Target Matrix",popup,WaveList
           ("*",";","") // use "*_580nm" to make it more
           specific or "*" to show all matrices
        DoPrompt "Select Matrix to Process and Output name
           .", Mat

   nr=Dimsize($mat,0) // Getting the number of columns
```

```
nc=Dimsize($mat,1) // Getting the number of columns
     nl=Dimsize($mat,2) // Getting the number of layers
        to cycle in for loop

     //build the names of the waves needed
     base=RemoveEnding(mat, "_Raw")
     Routput = base + "_AF"

Wave WTarget = $mat   // Local reference for mat
Duplicate  WTarget, $Routput  //Duplicate mat and use new
    name with, suffix _AF
Wave WFilter= $Routput // Local reference to Routput. The
    next command does not accept $Routput as input.
     //The WAVE declaration is required when you use a
        wave in an assignment statement (=) in a function
        .

For (ii=0;ii<nl;ii+=1)
MatrixOp/O Dummy = Layer(WTarget,ii) // Extract the layer
    to be filtered
MatrixFilter /N=5 avg Dummy          // Apply filter

// Perform wave assignment [] means all elements and p,q
   are needed for indexing. Otherwise,
//there will be an error where waves indexes will not
   match.
```

```
   WFilter[][][ii] = Dummy[p][q]                // Add Layer
       to the filtered stack, wave with suffix _AF.

   endfor

  KillWaves Dummy

End

Function SNARF_Calibration()
NewPanel /N=SNARF_Calibration
Variable/G pKa, Rb, Ra, IbIa

        pKa=7.33
        Rb=0.15
        Ra=4
        IbIa=3.73

        SetVariable pKa,pos={8.00,0.00},size={113.00,20.00},
           bodyWidth=83,title="pKa"
        SetVariable pKa,fSize=14
        SetVariable pKa,limits={20,0.1,0.01},value=pKa,live
           =1

        SetVariable Rb,pos={17.00,31.00},size
           ={105.00,20.00},bodyWidth=84,title="Rb"
        SetVariable Rb,fSize=14
```

```
        SetVariable Rb,limits={0.01,10,0.01},value=Rb,live=1

        SetVariable Ra,pos={17.00,65.00},size
           ={105.00,20.00},title="\\Z14Ra",fSize=14
        SetVariable Ra,limits={0.01,20,0.01},value=Ra,live=1

        SetVariable IbIa,pos={8.00,92.00},size
           ={104.00,23.00}
        SetVariable IbIa,title="\\Z14I\\Bb\\M/I\\Ba",fSize
           =14
        SetVariable IbIa,limits={0.01,100,0.01},value=IbIa

        DrawText 58,150,"pH=pKa-log[(R-Rb)/(Ra-R)]*(Ib,2/Ia
           ,2)"

end

Function Ratiometric_Analysis()

        String mat //Name of 580 nm matrix
        String mat1 //Name of 640 nm matrix
        String Routput
        String Routput1  //Name of interpolated matrix
        String base
        String base1
        Variable nr,nc, nrs, ncs
        Variable/G pKa, Rb, Ra, IbIa
```

```
//Prompt mat,"2D 580 nm Matrix Wave (Number of
   layers and chunks must be zero)",popup,WaveList
   ("*_580nm",";","DIMS:2") // use "*_580nm" to make
    it more specific or "*" to show all matrices
//DoPrompt "Select Matrix to Process and Output name
   .", Mat

//Prompt mat1,"2D 640 nm Matrix Wave (Number of
   layers and chunks must be zero)",popup,WaveList
   ("*_640nm",";","DIMS:2") // use "*_680nm" to make
    it more specific or "*" to show all matrices
//DoPrompt "Select Matrix to Process and Output name
   ", Mat1

Prompt mat,"580 nm Matrix Wave",popup,WaveList
   ("*",";","") // use "*_580nm" to make it more
   specific or "*" to show all matrices
DoPrompt "Select Matrix to Process and Output name
   .", Mat

Prompt mat1,"640 nm Matrix Wave",popup,WaveList
   ("*",";","") // use "*_680nm" to make it more
   specific or "*" to show all matrices
DoPrompt "Select Matrix to Process and Output name",
    Mat1
```

```
      //Prompt output,"Output triplet wave name"
      //Prompt mktbl,"Put triplet in new table?",popup,"
         Yes;No"

      //build the names of the waves needed
      base=RemoveEnding(mat, "_Raw")
      Routput = base + "_Ratio"
      Routput1 = base + "_RA_pH_Raw"

// Check that the matrices have the same size; if not,
   stop the code and provide a message
      Silent 1;PauseUpdate
      if( WaveDims($mat) != WaveDims($mat1))
              Abort mat+" do not have matching dimensions!
                 "
      endif


// Make sure there are no zeros in the matrices.
   Otherwise, there will be a problem when calculating
   the log.
Wave W580 = $mat   // Local reference for mat
Wave W640 = $mat1  // Local reference for mat1

MatrixOp/O Dummy = replace(W580,0,1)
MatrixOp/O Dummy1 = replace(W640,0,1)
```

```
   // Calculate matrix with ratio
        MatrixOp/O $Routput = Dummy/Dummy1
        Wave Ratio= $Routput // Local reference to Routput.
           The next command does not accept $Routput as
           input.
        //The WAVE declaration is required when you use a
           wave in an assignment statement (=) in a function
           .

   // Calculate matrix with pH

  // MatrixOp/O $Routput1 = 7.33-log(((Ratio-0.15)/(4-Ratio)
     )*3.712)
   //MatrixOp/O $Routput1 = 7.33-log(((Ratio-0.15)/(4-Ratio)
      )*8.7)
   MatrixOp/O $Routput1 = pKa-log(((Ratio-Rb)/(Ra-Ratio))*
      IbIa)

  KillWaves Dummy,Dummy1

end

Function MatrixIntp()
        String mat //Name of matrix to convert to triplet
           and interpolate
        String output
        //Variable mktbl=2
```

```
        //Variable mkgrf=2
        String Intoutput  //Name of interpolated matrix
        String base
        Variable nr,nc, nrs, ncs

        output="triplet"
        Prompt mat,"2D Matrix Wave",popup,WaveList("*_Raw
           ","";","DIMS:2") // use "*_Raw" to make it more
           specific or "*" to show all matrices
        DoPrompt "Select Matrix to Process and Output name",
            Mat
        //Prompt output,"Output triplet wave name"
        //Prompt mktbl,"Put triplet in new table?",popup,"
           Yes;No"

        //build the names of the waves needed
        base=RemoveEnding(mat, "_Raw")
        output = base + "_triplet"
        Intoutput = base + "_IntP"

// Check that the matrix fullfil the requirements
        Silent 1;PauseUpdate
        if( WaveDims($mat) != 2)
                Abort mat+" is not a two-dimensional wave!"
        endif
```

```
        output= CleanupName(output,1)    // allow liberal
           names
        if( strlen(output) == 0 )
                Abort "Please enter an name for the output
                   wave"
        endif

//Obtain the parameters for the interpolation
 nr=Dimsize($mat,0) // Getting the number of rows for
    Interpolation function, x-dimension
 nc=Dimsize($mat,1) // Getting the number of columns for
    Interpolation function, y-dimension
 nrs=IndexToScale($mat,nr,0)// It provides the dimension at
    the final point
 ncs=IndexToScale($mat,nc,1)// It provides the dimension at
    the final point

        fMatrixToXYZTriplet2($mat,output)
        ImageInterpolate /DEST=$Intoutput /S={0,0.2,nrs
           ,0,0.2,ncs} Voronoi $output

        //Preferences 1
        //if( mktbl == 1)
                //Edit $output
        //endif
End
```

```
Function fMatrixToXYZTriplet2(matrixWave, outputName)
        Wave matrixWave
        String outputName

        Variable dimx=DimSize(matrixWave,0)
        Variable dimy=DimSize(matrixWave,1)
        Variable rows=dimx*dimy
        Make/O/N=(rows,3) $outputName
        WAVE TripletWave= $outputName

        Variable xStart,xDelta
        Variable yStart,yDelta

        xStart=DimOffset(matrixWave,0)
        yStart=DimOffset(matrixWave,1)
        xDelta=DimDelta(matrixWave,0)
        yDelta=DimDelta(matrixWave,1)

        Variable i,j,count=0
        Variable xVal,yVal
        for(i=0;i<dimy;i+=1)            // i is y (column)
                yVal=yStart+i*yDelta
                for(j=0;j<dimx;j+=1)    // j is x (row)
                        xVal=xStart+j*xDelta
                        TripletWave[count][0]=xVal
                        TripletWave[count][1]=yVal
```

```
                        TripletWave[count][2]= matrixWave[j
                           ][i] // [row][col]
                        count+=1
                endfor
        endfor
End


//Preferences 1
        //if( mktbl == 1)
                //Edit $output
        //endif

Function DCursorMoved2()
String MatInt
Variable nr,nc,ns,AxisSignal

//Obtaining the input MatInt
// *** <This is where we can change the waves that are
   displayed in the menus. Just modify Wavelist statement***
//Prompt MatInt,"2D Matrix Wave",popup,WaveList("*_IntP
   ",";","DIMS:2") // use "*_Raw" to make it more specific
Prompt MatInt,"2D Matrix Wave",popup,WaveList("*",";","") //
    use "*_Raw" or "*_IntP" to make it more specific
Prompt AxisSignal,"Left or Right Axis?",popup,"Left Axis;
   Right Axis"
DoPrompt "Select Matrix to Plot as Image", MatInt,AxisSignal
```

```
// Changing names and creating wave references
Wave IntpHProfile=$MatInt //Local reference to
   M_InterpolatedImage, similar to the use of $ and strings
String TMW=NameOfWave(IntpHProfile) //String containing name
    of wave used in ModifiedImage--Can also use MaTInt
   String
String WNameProfile=TMW + "-Prof" //Name of profile wave

/// Creating profile wave
nr=Dimsize(IntpHProfile,0) // Getting the number of rows for
    Profile wave
ns=DimDelta(IntpHProfile,0)// Getting the scale for profile
   wave
Make/O/N=(nr)/D $WNameProfile // Create the profile wave to
   be updated later
SetScale/P x 0,ns,"", $WNameProfile
Wave w=$WNameProfile

if( AxisSignal == 1)
        Display /W=(14,45,633,530) as MatInt
        AppendImage/L IntpHProfile
        ModifyImage/Z [0] ctab= {7.1,7.5,Spectrum,0}
        ModifyGraph margin(left)=72,margin(bottom)=72,margin
           (top)=36,margin(right)=108
        ModifyGraph mirror=2, fSize=16
```

```
        ModifyGraph lblMargin(left)=11,lblMargin(bottom)=17,
           lblLatPos(left)=-2,lblLatPos(bottom)=5
        Label left " \\Z18 Y ( m )"
        Label bottom " \\Z18 X ( m )"
        SetAxis/Z left 0,17
        SetAxis/Z bottom 0,17
        Cursor/P/I A $TMW 100,100 // $TMW it refers to the
           actual name of the image or trace
        ShowInfo
        ColorScale/C/N=pH/F=0/A=MC/X=60.67/Y=0.00 image=$TMW
            // $TMW it refers to the actual name of the
           image
        //AppendText "\\Z18 pH"
SetWindow kwTopWin,hook(myHook)=myCursorMovedHook //It sets
   the window hook so that when an event occur on the graph,
    the function is executed

        Display w
                PauseUpdate; Silent 1           // modifying
                    window...
                ModifyGraph/Z margin(left)=72,margin(bottom)
                   =72,margin(top)=36
                ModifyGraph/Z lSize=2,mirror=2,fSize=16
                Label/Z left "\\Z18 pH "
                Label/Z bottom "\\Z18 X ( m )"
                SetAxis/Z left 7.1,7.5
```

```
else

Display /W=(14,45,633,530) as MatInt
        AppendImage/R IntpHProfile
   ModifyImage/Z [0] ctab= {7.1,7.5,Spectrum,0}
        ModifyGraph margin(left)=72,margin(bottom)
           =72,margin(top)=36,margin(right)=108
        ModifyGraph mirror=2, fSize=16
        ModifyGraph lblMargin(right)=17,lblMargin(
           bottom)=17,lblLatPos(right)=-2,lblLatPos(
           bottom)=5
        Label right " \\Z18 Y ( m )"
        Label bottom " \\Z18 X ( m )"
        SetAxis right 0,17
        SetAxis bottom 0,17
        Cursor/P/I A $TMW 100,100 // $TMW it refers
           to the actual name of the image or trace
        ShowInfo
        ColorScale/C/N=pH/F=0/A=MC/X=60.67/Y=0.00
           image=$TMW // $TMW it refers to the
           actual name of the image
        //AppendText "\\Z18 pH"

SetWindow kwTopWin,hook(myHook)=myCursorMovedHook //
   It sets the window hook so that when an event
   occur on the graph, the function is executed
```

```
/// Creating profile wave
   Display/R w
        PauseUpdate; Silent 1          // modifying window
           ...
        ModifyGraph/Z margin(left)=72,margin(bottom)=72,
           margin(top)=36
        ModifyGraph/Z lSize=2,mirror=2,fSize=16
        Label/Z right "\\Z18 pH "
        Label/Z bottom "\\Z18 X ( m )"
        SetAxis/Z right 7.1,7.5

        endif

End

Function myCursorMovedHook(s)
        STRUCT WMWinHookStruct &s

        Variable statusCode= 0

        strswitch( s.eventName )
                case "cursormoved":
                        // see "Members of WMWinHookStruct
                           Used with cursormoved Code"
                        UpdateControls(s.traceName, s.
                           cursorName, s.pointNumber, s.
                           yPointNumber)
```

```
                        break
        endswitch

        return statusCode
End

Function UpdateControls(traceName, cursorName, pointNumber,
   yPointNumber)
        String traceName, cursorName
        Variable pointNumber, yPointNumber

        Wave ww=traceNameToWaveRef("",traceName)
        print NameOfWave(ww)

        GetWindow kwTopWin wavelist
        Wave/T WL=W_Wavelist
        String Nwavename =WL[0][0]
        //print Nwavename
        Wave IntpHProfile=$NwaveName
        String WNameProfile=NwaveName + "-Prof"
        Wave w=$WNameProfile //Local reference to the pH
           profile wave created infirst function.
        w=IntpHProfile[p][yPointNumber]


End
```

Appendix G

Modeling of pH Gradients under dc Fields in Comsol

Attached is a complete report of modeling of pH gradients under dc fields generated from COMSOL MULTIPHYSICS. The report provides a complete demonstration of the model setup at COMSOL interface. The first section provides details of the parameters used in the model. The second section describes the geometry, variables, functions and tertiary current distribution module, mesh setup used for solving the pH profiles. The time dependant setup and solver configuration are described in the last section.

1 Global Definitions

GLOBAL SETTINGS

Name	Kunnn-1 5A m 2.mph
Path	C:\Users\behdanb\Documents\Paper_Simulations\Kunnn-1_5A_m_2.mph
Version	COMSOL Multiphysics 5.6 (Build: 401)
Unit system	SI

USED PRODUCTS

COMSOL Multiphysics

COMPUTER INFORMATION

CPU	Intel64 Family 6 Model 85 Stepping 7, 8 cores
Operating system	Windows Server 2019

1.1 PARAMETERS

PARAMETERS 1

Name	Expression	Value	Description
D_H	9.3e-9[m^2/s]	9.3E−9 m²/s	
D_OH	5.5e-9[m^2/s]	5.5E−9 m²/s	
k1	1.4e11[1/(M*s)]	1.4E8 m³/(s·mol)	
k2	0.0014[s^ - 1]	0.0014 1/s	
C_H2O	55[M]	55000 mol/m³	
Id	4.5[A/m^2]	4.5 A/m²	
F	96485.3329[s*A/mol]	96485 C/mol	
D_Na	1.3e-9[m^2/s]	1.3E−9 m²/s	
D_cl	2.3e-9[m^2/s]	2.3E−9 m²/s	
k3	442719[1/(M*s)]	442.72 m³/(s·mol)	
k4	0.14[s^ - 1]	0.14 1/s	
D_F	9.3e-10[m^2/s]	9.3E−10 m²/s	
D_HF	2.3e-9[m^2/s]	2.3E−9 m²/s	

2 Component 1

Date	Sep 15, 2021 11:00:19 AM

SETTINGS

Description	Value
Unit system	Same as global system (SI)
Geometry shape function	Automatic

SPATIAL FRAME COORDINATES

First	Second	Third
x	y	z

MATERIAL FRAME COORDINATES

First	Second	Third
X	Y	Z

GEOMETRY FRAME COORDINATES

First	Second	Third
Xg	Yg	Zg

MESH FRAME COORDINATES

First	Second	Third
Xm	Ym	Zm

2.1 GEOMETRY 1

Geometry 1

UNITS

Length unit	µm
Angular unit	deg

GEOMETRY STATISTICS

Description	Value
Space dimension	1
Number of domains	3
Number of boundaries	4

2.1.1 Interval 1 (i1)

INTERVAL

Coordinates (µm)
0
20

2.1.2 Interval 2 (i2)

INTERVAL

Coordinates (µm)
20
100

2.1.3 Interval 3 (i3)

INTERVAL

Coordinates (µm)
100
120

2.2 COEFFICIENT FORM PDE

USED PRODUCTS

COMSOL Multiphysics

Coefficient Form PDE

SELECTION

Geometric entity level	Domain
Selection	Geometry geom1: Dimension 1: All domains

2.2.1 Interface Settings

Discretization

SETTINGS

Description	Value
Shape function type	Lagrange
Element order	Quadratic
Frame	Spatial

Units

Dependent variable quantity	Unit
Custom unit	mol/m^3

Source term quantity	Unit
Custom unit	mol/m^3/s

2.2.2 Variables

Name	Expression	Unit	Description	Selection	Details
c.nx	nx		Normal vector, x component	Boundaries 1–4	Meta
c.ny	root.ny		Normal vector, y component	Boundaries 1–4	Meta
c.nz	root.nz		Normal vector, z component	Boundaries 1–4	Meta
c.nxmesh	nxmesh		Normal vector (mesh), x component	Boundaries 1–4	Meta
c.nymesh	root.nymesh		Normal vector (mesh), y component	Boundaries 1–4	Meta
c.nzmesh	root.nzmesh		Normal vector (mesh), z component	Boundaries 1–4	Meta

2.2.3 Coefficient Form PDE 1

Coefficient Form PDE 1

SELECTION

Geometric entity level	Domain
Selection	Geometry geom1: Dimension 1: All domains

EQUATIONS

$$e_a\frac{\partial^2 C_H}{\partial t^2}+d_a\frac{\partial C_H}{\partial t}+\nabla\cdot(-c\nabla C_H-\alpha C_H+\gamma)+\beta\cdot\nabla C_H+aC_H=f$$

$$\nabla=\frac{\partial}{\partial x}$$

SETTINGS

Description	Value
Absorption coefficient	k1*C_OH + k3*C_F
Diffusion coefficient	D_H
Convection coefficient	0
Source term	k2*C_H2O + k4*C_HF
Conservative flux source	0
Conservative flux convection coefficient	0
Mass coefficient	0
Damping or mass coefficient	1

Variables

Name	Expression	Unit	Description	Selection
domflux.C_Hx	-D_H*C_Hx	mol/(m²·s)	Domain flux, x component	Domains 1–3

Shape functions

Name	Shape function	Unit	Description	Shape frame	Selection
C_H	Lagrange (Quadratic)	mol/m³	Dependent variable C_H	Spatial	Domains 1–3

2.2.4 Zero Flux 1

Zero Flux 1

SELECTION

Geometric entity level	Boundary
Selection	Geometry geom1: Dimension 0: All boundaries

EQUATIONS

$$-\mathbf{n}\cdot(-c\nabla C_H - \alpha C_H + \gamma) = 0$$
$$\nabla = \frac{\partial}{\partial x}$$

2.2.5 Initial Values 1

Initial Values 1

SELECTION

Geometric entity level	Domain
Selection	Geometry geom1: Dimension 1: All domains

SETTINGS

Description	Value
Initial time derivative of C_H	0
Initial value for C_H	10^(-7.2)*1000

2.2.6 Flux/Source 1

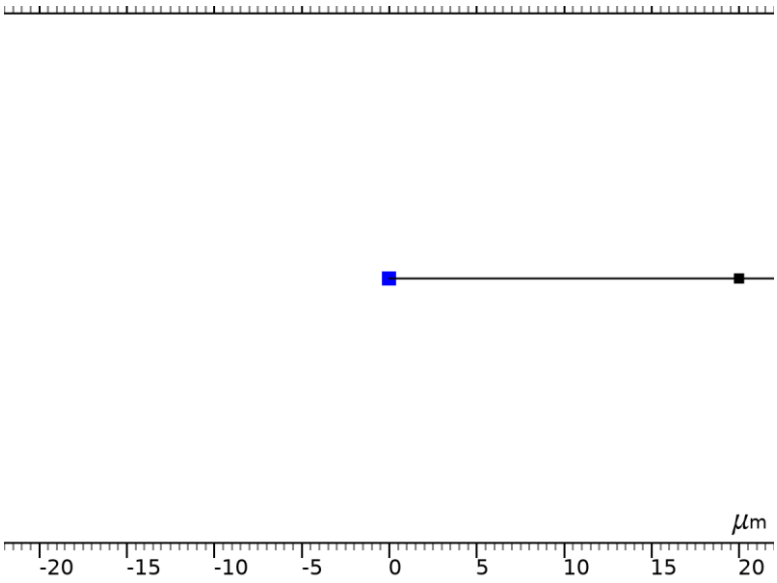

Flux/Source 1

SELECTION

Geometric entity level	Boundary
Selection	Geometry geom1: Dimension 0:

	Boundary 1

EQUATIONS

$$-\mathbf{n}\cdot(-c\nabla C_H - \alpha C_H + \gamma) = g - qC_H$$
$$\nabla = \frac{\partial}{\partial x}$$

SETTINGS

Description	Value
Boundary absorption/impedance term	0
Boundary flux/source	Id/F

Variables

Name	Expression	Unit	Description	Selection	Details
c.g_C_H	Id/F	mol/(m²·s)	Boundary flux/source	Boundary 1	+ operation

2.3 COEFFICIENT FORM PDE 2

USED PRODUCTS

COMSOL Multiphysics

Coefficient Form PDE 2

SELECTION

Geometric entity level	Domain
Selection	Geometry geom1: Dimension 1: All domains

2.3.1 Interface Settings

Discretization

SETTINGS

Description	Value
Shape function type	Lagrange
Element order	Quadratic
Frame	Spatial

Units

Dependent variable quantity	Unit
Concentration	mol/m^3

Source term quantity	Unit
Custom unit	mol/m^3/s

2.3.2 Variables

Name	Expression	Unit	Description	Selection	Details
c2.nx	nx		Normal vector, x component	Boundaries 1–4	Meta
c2.ny	root.ny		Normal vector, y component	Boundaries 1–4	Meta
c2.nz	root.nz		Normal vector, z component	Boundaries 1–4	Meta
c2.nxmesh	nxmesh		Normal vector (mesh), x component	Boundaries 1–4	Meta
c2.nymesh	root.nymesh		Normal vector (mesh), y component	Boundaries 1–4	Meta
c2.nzmesh	root.nzmesh		Normal vector (mesh), z component	Boundaries 1–4	Meta

2.3.3 Coefficient Form PDE 1

Coefficient Form PDE 1

SELECTION

Geometric entity level	Domain
Selection	Geometry geom1: Dimension 1: All domains

EQUATIONS

$$e_a\frac{\partial^2 C_OH}{\partial t^2}+d_a\frac{\partial C_OH}{\partial t}+\nabla\cdot(-c\nabla C_OH-\alpha C_OH+\gamma)+\beta\cdot\nabla C_OH+aC_OH=f$$

$$\nabla=\frac{\partial}{\partial x}$$

SETTINGS

Description	Value
Absorption coefficient	k1*C_H
Diffusion coefficient	D_OH
Convection coefficient	0
Source term	k2*C_H2O
Conservative flux source	0
Conservative flux convection coefficient	0
Mass coefficient	0
Damping or mass coefficient	1

Variables

Name	Expression	Unit	Description	Selection
domflux.C_OHx	-D_OH*C_OHx	mol/(m²·s)	Domain flux, x component	Domains 1–3

Shape functions

Name	Shape function	Unit	Description	Shape frame	Selection
C_OH	Lagrange (Quadratic)	mol/m³	Dependent variable C_OH	Spatial	Domains 1–3

2.3.4 Zero Flux 1

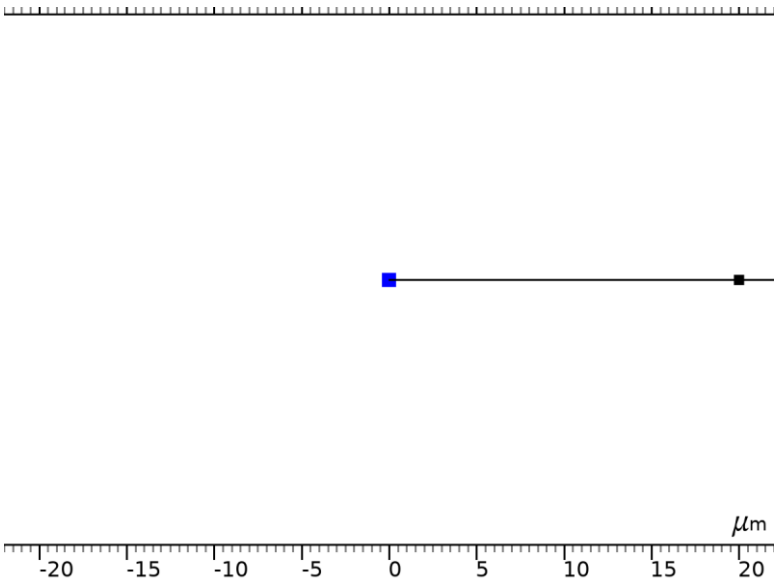

Zero Flux 1

SELECTION

Geometric entity level	Boundary
Selection	Geometry geom1: Dimension 0: All boundaries

EQUATIONS

$$-\mathbf{n}\cdot(-c\nabla C_O H - \alpha C_O H + \gamma) = 0$$

$$\nabla = \frac{\partial}{\partial x}$$

2.3.5 Initial Values 1

Initial Values 1

SELECTION

Geometric entity level	Domain
Selection	Geometry geom1: Dimension 1: All domains

SETTINGS

Description	Value
Initial time derivative of C_OH	0

Description	Value
Initial value for C_OH	10^(-6.8)*1000

2.3.6 Flux/Source 1

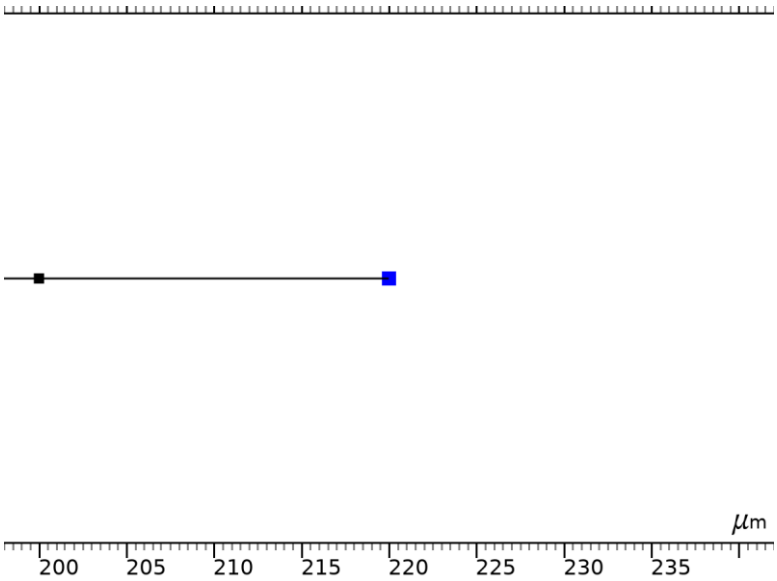

Flux/Source 1

SELECTION

Geometric entity level	Boundary
Selection	Geometry geom1: Dimension 0: Boundary 4

EQUATIONS

$$-\mathbf{n}\cdot(-c\nabla C_OH - \alpha C_OH + \gamma) = g - qC_OH$$

$$\nabla = \frac{\partial}{\partial x}$$

SETTINGS

Description	Value
Boundary absorption/impedance term	0
Boundary flux/source	Id/F

Variables

Name	Expression	Unit	Description	Selection	Details
c2.g_C	Id/F	mol/(m²	Boundary	Boundar	+ operatio

Name	Expression	Unit	Description	Selection	Details
_OH		·s)	flux/source	y 4	n

2.4 COEFFICIENT FORM PDE 3

USED PRODUCTS

COMSOL Multiphysics

Coefficient Form PDE 3

SELECTION

Geometric entity level	Domain
Selection	Geometry geom1: Dimension 1: All domains

2.4.1 Interface Settings

Discretization

SETTINGS

Description	Value
Shape function type	Lagrange
Element order	Quadratic
Frame	Spatial

Units

Dependent variable quantity	Unit
Concentration	mol/m^3

Source term quantity	Unit
Custom unit	mol/m^3/s

2.4.2 Variables

Name	Expression	Unit	Description	Selection	Details
c3.nx	nx		Normal vector, x component	Boundaries 1–4	Meta
c3.ny	root.ny		Normal	Boundaries	Meta

Name	Expression	Unit	Description	Selection	Details
			vector, y component	1–4	
c3.nz	root.nz		Normal vector, z component	Boundaries 1–4	Meta
c3.nxmesh	nxmesh		Normal vector (mesh), x component	Boundaries 1–4	Meta
c3.nymesh	root.nymesh		Normal vector (mesh), y component	Boundaries 1–4	Meta
c3.nzmesh	root.nzmesh		Normal vector (mesh), z component	Boundaries 1–4	Meta

2.4.3 Coefficient Form PDE 1

Coefficient Form PDE 1

SELECTION

Geometric entity level	Domain
Selection	Geometry geom1: Dimension 1: All domains

EQUATIONS

$$e_a\frac{\partial^2 C_N a}{\partial t^2} + d_a\frac{\partial C_N a}{\partial t} + \nabla\cdot(-c\nabla C_N a - \alpha C_N a + \gamma) + \beta\cdot\nabla C_N a + aC_N a = f$$

$$\nabla = \frac{\partial}{\partial x}$$

SETTINGS

Description	Value
Absorption coefficient	0
Diffusion coefficient	D_Na
Convection coefficient	0
Source term	0
Conservative flux source	0

Description	Value
Conservative flux convection coefficient	0
Mass coefficient	0
Damping or mass coefficient	1

Variables

Name	Expression	Unit	Description	Selection
domflux.C_Nax	-D_Na*C_Nax	mol/(m²·s)	Domain flux, x component	Domains 1–3

Shape functions

Name	Shape function	Unit	Description	Shape frame	Selection
C_Na	Lagrange (Quadratic)	mol/m³	Dependent variable C_Na	Spatial	Domains 1–3

2.4.4 Zero Flux 1

Zero Flux 1

SELECTION

Geometric entity level	Boundary
Selection	Geometry geom1: Dimension 0: All boundaries

EQUATIONS

$$-\mathbf{n}\cdot(-c\nabla C_N a - \alpha C_N a + \gamma) = 0$$

$$\nabla = \frac{\partial}{\partial x}$$

2.4.5 Initial Values 1

Initial Values 1

SELECTION

Geometric entity level	Domain
Selection	Geometry geom1: Dimension 1: All domains

SETTINGS

Description	Value
Initial value for C_Na	0.2
Initial time derivative of C_Na	0

2.5 COEFFICIENT FORM PDE 5

USED PRODUCTS

COMSOL Multiphysics

Coefficient Form PDE 5

SELECTION

Geometric entity level	Domain
Selection	Geometry geom1: Dimension 1: All domains

2.5.1 Interface Settings

Discretization

SETTINGS

Description	Value
Shape function type	Lagrange
Element order	Quadratic
Frame	Spatial

Units

Dependent variable quantity	Unit
Concentration	mol/m^3

Source term quantity	Unit
Custom unit	mol/m^3/s

2.5.2 Variables

Name	Expression	Unit	Description	Selection	Details
c5.nx	nx		Normal vector, x	Boundaries 1–4	Meta

Name	Expression	Unit	Description	Selection	Details
			component		
c5.ny	root.ny		Normal vector, y component	Boundaries 1–4	Meta
c5.nz	root.nz		Normal vector, z component	Boundaries 1–4	Meta
c5.nxmesh	nxmesh		Normal vector (mesh), x component	Boundaries 1–4	Meta
c5.nymesh	root.nymesh		Normal vector (mesh), y component	Boundaries 1–4	Meta
c5.nzmesh	root.nzmesh		Normal vector (mesh), z component	Boundaries 1–4	Meta

2.5.3 Coefficient Form PDE 1

Coefficient Form PDE 1

SELECTION

Geometric entity level	Domain
Selection	Geometry geom1: Dimension 1: All domains

EQUATIONS

$$e_a\frac{\partial^2 C_F}{\partial t^2}+d_a\frac{\partial C_F}{\partial t}+\nabla\cdot(-c\nabla C_F-\alpha C_F+\gamma)+\beta\cdot\nabla C_F+aC_F=f$$

$$\nabla=\frac{\partial}{\partial x}$$

SETTINGS

Description	Value
Absorption coefficient	k3*C_H
Diffusion coefficient	D_F
Convection coefficient	0

Description	Value
Source term	k4*C_HF
Conservative flux source	0
Conservative flux convection coefficient	0
Mass coefficient	0
Damping or mass coefficient	1

Variables

Name	Expression	Unit	Description	Selection
domflux.C_Fx	-D_F*C_Fx	mol/(m²·s)	Domain flux, x component	Domains 1–3

Shape functions

Name	Shape function	Unit	Description	Shape frame	Selection
C_F	Lagrange (Quadratic)	mol/m³	Dependent variable C_F	Spatial	Domains 1–3

2.5.4 Zero Flux 1

Zero Flux 1

SELECTION

Geometric entity level	Boundary
Selection	Geometry geom1: Dimension 0: All boundaries

EQUATIONS

$$-\mathbf{n}\cdot(-c\nabla C_F - \alpha C_F + \gamma) = 0$$

$$\nabla = \frac{\partial}{\partial x}$$

2.5.5 Initial Values 1

Initial Values 1

SELECTION

Geometric entity level	Domain

Selection	Geometry geom1: Dimension 1: All domains

SETTINGS

Description	Value
Initial time derivative of C_F	0
Initial value for C_F	0.1

2.6 COEFFICIENT FORM PDE 6

USED PRODUCTS

COMSOL Multiphysics

Coefficient Form PDE 6

SELECTION

Geometric entity level	Domain
Selection	Geometry geom1: Dimension 1: All domains

2.6.1 Interface Settings

Discretization

SETTINGS

Description	Value
Shape function type	Lagrange
Element order	Quadratic
Frame	Spatial

Units

Dependent variable quantity	Unit
Concentration	mol/m^3

Source term quantity	Unit
Custom unit	mol/m^3/s

2.6.2 Variables

Name	Expression	Unit	Description	Selection	Details

Name	Expression	Unit	Description	Selection	Details
c6.nx	nx		Normal vector, x component	Boundaries 1–4	Meta
c6.ny	root.ny		Normal vector, y component	Boundaries 1–4	Meta
c6.nz	root.nz		Normal vector, z component	Boundaries 1–4	Meta
c6.nxmesh	nxmesh		Normal vector (mesh), x component	Boundaries 1–4	Meta
c6.nymesh	root.nymesh		Normal vector (mesh), y component	Boundaries 1–4	Meta
c6.nzmesh	root.nzmesh		Normal vector (mesh), z component	Boundaries 1–4	Meta

2.6.3 Coefficient Form PDE 1

Coefficient Form PDE 1

SELECTION

Geometric entity level	Domain
Selection	Geometry geom1: Dimension 1: All domains

EQUATIONS

$$e_a\frac{\partial^2 C_H F}{\partial t^2} + d_a\frac{\partial C_H F}{\partial t} + \nabla\cdot(-c\nabla C_H F - \alpha C_H F + \gamma) + \beta\cdot\nabla C_H F + aC_H F = f$$

$$\nabla = \frac{\partial}{\partial x}$$

SETTINGS

Description	Value
Absorption coefficient	k4

Description	Value
Diffusion coefficient	D_HF
Convection coefficient	0
Source term	k3*C_F*C_H
Conservative flux source	0
Conservative flux convection coefficient	0
Mass coefficient	0
Damping or mass coefficient	1

Variables

Name	Expression	Unit	Description	Selection
domflux.C_HFx	-D_HF*C_HFx	mol/(m²·s)	Domain flux, x component	Domains 1–3

Shape functions

Name	Shape function	Unit	Description	Shape frame	Selection
C_HF	Lagrange (Quadratic)	mol/m³	Dependent variable C_HF	Spatial	Domains 1–3

2.6.4 Zero Flux 1

Zero Flux 1

SELECTION

Geometric entity level	Boundary
Selection	Geometry geom1: Dimension 0: All boundaries

EQUATIONS

$$-\mathbf{n}\cdot(-c\nabla C_H F - \alpha C_H F + \gamma) = 0$$

$$\nabla = \frac{\partial}{\partial x}$$

2.6.5 Initial Values 1

Initial Values 1

SELECTION

Geometric entity level	Domain
Selection	Geometry geom1: Dimension 1: All domains

SETTINGS

Description	Value
Initial value for C_HF	0
Initial time derivative of C_HF	0

2.7 MESH 1

Mesh 1

MESH STATISTICS

Description	Value
Minimum element quality	1.0
Average element quality	1.0
Edge element	10600
Vertex element	4

2.7.1 Size (size)

SETTINGS

Description	Value
Maximum element size	2.2
Minimum element size	0.0044
Curvature factor	0.2
Predefined size	Extremely fine

2.7.2 Edge 1 (edg1)

SELECTION

Geometric entity level	Domain
Selection	Geometry geom1: Dimension 1: Domain 2

Edge 1

Distribution 1 (dis1)

SELECTION

Geometric entity level	Domain
Selection	Geometry geom1: Dimension 1: Domain 2

Distribution 1

SETTINGS

Description	Value
Number of elements	10000

2.7.3 Edge 2 (edg2)

SELECTION

Geometric entity level	Domain
Selection	Remaining

Edge 2

Distribution 1 (dis1)

SELECTION

Geometric entity level	Domain
Selection	Geometry geom1: Dimension 1: All domains

Distribution 1

SETTINGS

Description	Value
Number of elements	300

3 Study 1

COMPUTATION INFORMATION

Computation time	1 min 5 s

3.1 TIME DEPENDENT

Times	Unit
range(0,1E-1,20)	s

STUDY SETTINGS

Description	Value
Include geometric nonlinearity	Off

STUDY SETTINGS

Description	Value
Output times	{0, 0.1, 0.2, 0.30000000000000004, 0.4, 0.5, 0.6000000000000001, 0.7000000000000001, 0.8, 0.9, 1, 1.1, 1.2000000000000002, 1.3, 1.4000000000000001, 1.5, 1.6, 1.7000000000000002, 1.8, 1.9000000000000001, 2, 2.1, 2.2, 2.3000000000000003, 2.4000000000000004, 2.5, 2.6, 2.7, 2.8000000000000003, 2.9000000000000004, 3, 3.1, 3.2, 3.3000000000000003, 3.4000000000000004, 3.5, 3.6, 3.7, 3.8000000000000003, 3.9000000000000004, 4, 4.1000000000000005, 4.2, 4.3, 4.4, 4.5, 4.6000000000000005, 4.7, 4.800000000000001, 4.9, 5, 5.1000000000000005, 5.2, 5.300000000000001, 5.4, 5.5, 5.6000000000000005, 5.7, 5.800000000000001, 5.9, 6, 6.1000000000000005, 6.2, 6.300000000000001, 6.4, 6.5, 6.6000000000000005, 6.7, 6.800000000000001, 6.9, 7, 7.1000000000000005, 7.2, 7.300000000000001, 7.4, 7.5, 7.6000000000000005, 7.7, 7.800000000000001, 7.9, 8, 8.1, 8.200000000000001, 8.3, 8.4, 8.5, 8.6, 8.700000000000001, 8.8, 8.9, 9, 9.1, 9.200000000000001, 9.3, 9.4, 9.5, 9.600000000000001, 9.700000000000001, 9.8, 9.9, 10, 10.100000000000001, 10.200000000000001, 10.3, 10.4, 10.5, 10.600000000000001, 10.700000000000001, 10.8, 10.9, 11, 11.100000000000001, 11.200000000000001, 11.3, 11.4, 11.5, 11.600000000000001,

Description	Value
	11.700000000000001, 11.8, 11.9, 12, 12.100000000000001, 12.200000000000001, 12.3, 12.4, 12.5, 12.600000000000001, 12.700000000000001, 12.8, 12.9, 13, 13.100000000000001, 13.200000000000001, 13.3, 13.4, 13.5, 13.600000000000001, 13.700000000000001, 13.8, 13.9, 14, 14.100000000000001, 14.200000000000001, 14.3, 14.4, 14.5, 14.600000000000001, 14.700000000000001, 14.8, 14.9, 15, 15.100000000000001, 15.200000000000001, 15.3, 15.4, 15.5, 15.600000000000001, 15.700000000000001, 15.8, 15.9, 16, 16.1, 16.2, 16.3, 16.400000000000002, 16.5, 16.6, 16.7, 16.8, 16.900000000000002, 17, 17.1, 17.2, 17.3, 17.400000000000002, 17.5, 17.6, 17.7, 17.8, 17.900000000000002, 18, 18.1, 18.2, 18.3, 18.400000000000002, 18.5, 18.6, 18.7, 18.8, 18.900000000000002, 19, 19.1, 19.200000000000003, 19.3, 19.400000000000002, 19.5, 19.6, 19.700000000000003, 19.8, 19.900000000000002, 20}
Tolerance	User controlled

VALUES OF DEPENDENT VARIABLES

Description	Value
Settings	User controlled

PHYSICS AND VARIABLES SELECTION

Physics interface	Discretization
Coefficient Form PDE (c)	physics
Coefficient Form PDE 2 (c2)	physics
Coefficient Form PDE 3 (c3)	physics
Coefficient Form PDE 4 (c4)	physics
Coefficient Form PDE 5 (c5)	physics
Coefficient Form PDE 6 (c6)	physics

MESH SELECTION

Geometry	Mesh
Geometry 1 (geom1)	mesh1

3.2 SOLVER CONFIGURATIONS

3.2.1 Solution 1

Compile Equations: Time Dependent (st1)

STUDY AND STEP

Description	Value
Use study	Study 1
Use study step	Time Dependent

LOG

<----
Compile Equations: Time Dependent in Study 1/Solution 1 (sol1) ----------
Started at Oct 24, 2023 1:58:18 PM.
Geometry shape function: Quadratic Lagrange
Running on Intel64 Family 6 Model 85 Stepping 7, GenuineIntel.
Using 1 socket with 8 cores in total on VUSE-120WM83.
Available memory: 32.42 GB.
Time: 1 s.
Physical memory: 1.06 GB
Virtual memory: 1.24 GB
Ended at Oct 24, 2023 1:58:18 PM.

Compile Equations: Time Dependent in Study 1/Solution 1 (sol1) ---------->

Dependent Variables 1 (v1)

GENERAL

Description	Value
Defined by study step	Time Dependent

RESIDUAL SCALING

Description	Value
Method	Manual

INITIAL VALUE CALCULATION CONSTANTS

Constant name	Initial value source
t	range(0,1E-1,20)
timestep	0.02[s]

LOG

<---- Dependent Variables 1 in Study 1/Solution 1 (sol1) ----------

Started at Oct 24, 2023 1:58:18 PM.
Solution time: 0 s.
Physical memory: 1.08 GB
Virtual memory: 1.24 GB
Ended at Oct 24, 2023 1:58:18 PM.

----- Dependent Variables 1 in Study 1/Solution 1 (sol1) ----------->

Dependent variable C_H (comp1.C_H) (comp1_C_H)

GENERAL

Description	Value
Field components	comp1.C_H
Internal variables	{comp1.uflux.C_H, comp1.dflux.C_H}

Dependent variable C_OH (comp1.C_OH) (comp1_C_OH)

GENERAL

Description	Value
Field components	comp1.C_OH
Internal variables	{comp1.uflux.C_OH, comp1.dflux.C_OH}

Dependent variable C_Na (comp1.C_Na) (comp1_C_Na)

GENERAL

Description	Value
Field components	comp1.C_Na
Internal variables	{comp1.uflux.C_Na, comp1.dflux.C_Na}

Dependent variable C_F (comp1.C_F) (comp1_C_F)

GENERAL

Description	Value
Field components	comp1.C_F
Internal variables	{comp1.uflux.C_F, comp1.dflux.C_F}

Dependent variable C_HF (comp1.C_HF) (comp1_C_HF)

GENERAL

Description	Value

Description	Value
Field components	comp1.C_HF
Internal variables	{comp1.uflux.C_HF, comp1.dflux.C_HF}

Time-Dependent Solver 1 (t1)

GENERAL

Description	Value
Defined by study step	Time Dependent
Output times	{0, 0.1, 0.2, 0.30000000000000004, 0.4, 0.5, 0.6000000000000001, 0.7000000000000001, 0.8, 0.9, 1, 1.1, 1.2000000000000002, 1.3, 1.4000000000000001, 1.5, 1.6, 1.7000000000000002, 1.8, 1.9000000000000001, 2, 2.1, 2.2, 2.3000000000000003, 2.4000000000000004, 2.5, 2.6, 2.7, 2.8000000000000003, 2.9000000000000004, 3, 3.1, 3.2, 3.3000000000000003, 3.4000000000000004, 3.5, 3.6, 3.7, 3.8000000000000003, 3.9000000000000004, 4, 4.1000000000000005, 4.2, 4.3, 4.4, 4.5, 4.6000000000000005, 4.7, 4.800000000000001, 4.9, 5, 5.1000000000000005, 5.2, 5.300000000000001, 5.4, 5.5, 5.6000000000000005, 5.7, 5.800000000000001, 5.9, 6, 6.1000000000000005, 6.2, 6.300000000000001, 6.4, 6.5, 6.6000000000000005, 6.7, 6.800000000000001, 6.9, 7, 7.1000000000000005, 7.2, 7.300000000000001, 7.4, 7.5, 7.6000000000000005, 7.7, 7.800000000000001, 7.9, 8, 8.1, 8.200000000000001, 8.3, 8.4, 8.5, 8.6, 8.700000000000001, 8.8, 8.9, 9, 9.1, 9.200000000000001, 9.3, 9.4, 9.5, 9.600000000000001, 9.700000000000001, 9.8, 9.9, 10, 10.100000000000001, 10.200000000000001, 10.3, 10.4, 10.5, 10.600000000000001, 10.700000000000001, 10.8, 10.9, 11, 11.100000000000001,

Description	Value
	11.200000000000001, 11.3, 11.4, 11.5, 11.600000000000001, 11.700000000000001, 11.8, 11.9, 12, 12.100000000000001, 12.200000000000001, 12.3, 12.4, 12.5, 12.600000000000001, 12.700000000000001, 12.8, 12.9, 13, 13.100000000000001, 13.200000000000001, 13.3, 13.4, 13.5, 13.600000000000001, 13.700000000000001, 13.8, 13.9, 14, 14.100000000000001, 14.200000000000001, 14.3, 14.4, 14.5, 14.600000000000001, 14.700000000000001, 14.8, 14.9, 15, 15.100000000000001, 15.200000000000001, 15.3, 15.4, 15.5, 15.600000000000001, 15.700000000000001, 15.8, 15.9, 16, 16.1, 16.2, 16.3, 16.400000000000002, 16.5, 16.6, 16.7, 16.8, 16.900000000000002, 17, 17.1, 17.2, 17.3, 17.400000000000002, 17.5, 17.6, 17.7, 17.8, 17.900000000000002, 18, 18.1, 18.2, 18.3, 18.400000000000002, 18.5, 18.6, 18.7, 18.8, 18.900000000000002, 19, 19.1, 19.200000000000003, 19.3, 19.400000000000002, 19.5, 19.6, 19.700000000000003, 19.8, 19.900000000000002, 20}

TIME STEPPING

Description	Value
Consistent initialization	Off

LOG

<---- Time-Dependent Solver 1 in Study 1/Solution 1 (sol1) ----------

Started at Oct 24, 2023 1:58:19 PM.
Time-dependent solver (BDF)
Number of degrees of freedom solved for: 106005 (plus 30 internal DOFs).
Nonsymmetric matrix found.
Scales for dependent variables:
Dependent variable C_F (comp1.C_F): 11
Dependent variable C_H (comp1.C_H): 4.1
Dependent variable C_HF (comp1.C_HF): 7.5
Dependent variable C_Na (comp1.C_Na): 0.2
Dependent variable C_OH (comp1.C_OH): 0.19

Step	Time	Stepsize	Res	Jac	Sol	Order	Tfail	NLfail	LinErr	LinRes
-	0	-	out							
1	4.8828e-06	4.8828e-06	26	8	26	1	0	6	1.9e-14	3.2e-14
2	9.7656e-06	4.8828e-06	27	8	27	1	0	6	2.4e-14	1.3e-14
3	1.4648e-05	4.8828e-06	28	8	28	1	0	6	1.8e-14	2.4e-14
4	2.4414e-05	9.7656e-06	30	9	30	1	0	6	3.3e-14	2.4e-14
5	3.418e-05	9.7656e-06	31	9	31	1	0	6	4.3e-14	2.8e-14
6	4.3945e-05	9.7656e-06	32	9	32	1	0	6	4.6e-14	3e-14
7	6.3477e-05	1.9531e-05	34	10	34	1	0	6	1.3e-13	1.5e-14
8	0.00010254	3.9063e-05	36	11	36	1	0	6	1.1e-14	3.9e-15
9	0.00018066	7.8125e-05	38	12	38	1	0	6	7.2e-15	4e-15
10	0.00033691	0.00015625	40	13	40	1	0	6	4.8e-14	4.8e-15
11	0.00049316	0.00015625	41	13	41	1	0	6	2.9e-14	7e-15
12	0.00080566	0.0003125	43	14	43	1	0	6	3.1e-14	5.2e-15

13 0.0011182 0.0003125 44 14 44 1 0 6 9.3e-14 4.9e-15
14 0.0014307 0.0003125 45 14 45 1 0 6 3.6e-14 5.2e-15
15 0.0017432 0.0003125 46 14 46 1 0 6 4.1e-14 5.4e-15
16 0.0020244 0.00028125 52 15 52 1 0 6 2.8e-14 1.1e-15
17 0.0022775 0.00025313 54 15 54 1 0 6 1e-14 1.1e-15
18 0.0025307 0.00025313 55 15 55 1 0 6 1.4e-14 1.4e-15
19 0.0030369 0.00050625 57 16 57 1 0 6 1.2e-13 3.7e-15
20 0.0040494 0.0010125 59 17 59 1 0 6 1.8e-13 1.7e-15
21 0.0050619 0.0010125 60 17 60 1 0 6 1.6e-13 1.1e-14
22 0.0070869 0.002025 62 18 62 1 0 6 4.8e-13 7.9e-15
23 0.0091119 0.002025 63 18 63 1 0 6 8.4e-13 1.1e-14
24 0.011137 0.002025 64 18 64 1 0 6 9.2e-13 9.6e-15
25 0.013162 0.002025 65 18 65 1 0 6 1.5e-13 6.9e-15
26 0.014947 0.0017849 71 19 71 1 0 6 1.1e-13 1.6e-15
27 0.016492 0.0015453 73 19 73 1 0 6 1.9e-13 1.7e-15
28 0.018037 0.0015453 74 19 74 1 0 6 3.1e-13 2.4e-15
29 0.021128 0.0030907 76 20 76 1 0 6 1.1e-12 6.6e-15
30 0.024219 0.0030907 77 20 77 1 0 6 5.2e-13 1.6e-14
31 0.02731 0.0030907 78 20 78 1 0 6 7e-13 2.3e-14
32 0.033491 0.0061814 84 21 84 2 0 6 9.3e-13 1.9e-15

33 0.039672 0.0061814 85 21 85 2 0 6 2e-12 3.1e-15
34 0.052035 0.012363 87 22 87 2 0 6 4e-12 6.3e-15
35 0.064398 0.012363 88 22 88 2 0 6 1.9e-12 1.9e-14
36 0.076761 0.012363 89 22 89 2 0 6 2.8e-12 7.6e-15
37 0.089123 0.012363 90 22 90 2 0 6 4.2e-12 2e-14
38 0.098714 0.0095907 96 23 96 1 0 6 8.4e-12 1.5e-14
- 0.1 - out
39 0.1061 0.0073896 98 23 98 1 0 6 1.2e-11 1.7e-14
40 0.11349 0.0073896 99 23 99 1 0 6 9e-12 1.7e-14
41 0.12088 0.0073896 100 23 100 1 0 6 1.2e-11 1.8e-14
42 0.12827 0.0073896 101 23 101 1 0 6 1.1e-11 1.6e-14
43 0.13566 0.0073896 107 24 107 1 0 6 4.7e-12 7.7e-15
44 0.14305 0.0073896 108 24 108 1 0 6 1.5e-12 6.9e-15
45 0.15044 0.0073896 109 24 109 1 0 6 3.1e-12 9.5e-15
46 0.16522 0.014779 111 25 111 1 0 6 1.9e-12 6e-15
47 0.18 0.014779 112 25 112 1 0 6 4.9e-12 5.6e-14
48 0.19478 0.014779 113 25 113 1 0 6 2.2e-12 1.8e-13
- 0.2 - out
49 0.22434 0.029558 115 25 115 2 0 6 5.5e-12 1e-14
50 0.25389 0.029558 116 25 116 2 0 6 2.3e-12 2.4e-14
51 0.28345 0.029558 122 26 122 2 0 6 1.8e-13 5.4e-14

```
  -        0.3          - out
 52     0.31301    0.029558      123   26  123     2     0      6  5.1e-
12  1.7e-14
 53     0.34257    0.029558      129   27  129     2     0      6  2.5e-
13  2.3e-14
 54     0.37213    0.029558      130   27  130     2     0      6  1.4e-
12  1.9e-14
  -        0.4          - out
 55     0.40169    0.029558      136   28  136     2     0      6  1.7e-
12  1.5e-14
 56     0.43124    0.029558      142   29  142     2     0      6  4.2e-
12  6.9e-15
 57      0.4608    0.029558      143   29  143     2     0      6  2.5e-
12    8e-15
 58     0.49036    0.029558      144   29  144     2     0      6  7.3e-
12  1.1e-14
  -        0.5          - out
 59     0.51992    0.029558      145   29  145     2     0      6  1.1e-
12  1.6e-14
 60     0.52177   0.0018474      160   32  160     2     0      8  2.1e-
13  3.7e-14
 61     0.52269   0.0009237      166   34  166     2     0      9  2.1e-
13  6.6e-14
 62     0.52269  1.8041e-06      188   40  188     2     0     14  4.3e-
14  3.9e-14
 63     0.52269  9.0205e-07      194   42  194     2     0     15  1.1e-
14  4.4e-14
 64     0.52269  1.8041e-06      196   43  196     2     0     15    6e-
15  2.1e-14
 65      0.5227  3.6082e-06      198   44  198     2     0     15    4e-
15  5.5e-15
 66     0.52271  7.2164e-06      200   45  200     1     0     15  8.4e-
15  6.3e-15
 67     0.52271  7.2164e-06      201   45  201     1     0     15  9.7e-
15  7.1e-15
 68     0.52273  1.4433e-05      203   46  203     1     0     15  1.1e-
14  2.1e-14
 69     0.52273  7.2164e-06      209   48  209     1     0     16    7e-
15  2.7e-14
```

70 0.52275 1.4433e-05 211 49 211 1 0 16 3e-15 3e-14
71 0.52278 2.8865e-05 212 50 212 1 0 16 1.3e-14 2.1e-14
72 0.52284 5.7731e-05 213 51 213 1 0 16 1e-13 7.2e-14
73 0.52295 0.00011546 214 52 214 1 0 16 1.9e-13 6.4e-13
74 0.52318 0.00023092 215 53 215 1 0 16 1.9e-13 9.1e-13
75 0.52364 0.00046185 216 54 216 1 0 16 4.7e-13 1.5e-12
76 0.52457 0.0009237 217 55 217 1 0 16 6.9e-13 2.3e-12
77 0.52641 0.0018474 218 56 218 1 0 16 1.6e-12 2.9e-12
78 0.53011 0.0036948 219 57 219 1 0 16 1.7e-12 7.9e-13
79 0.5375 0.0073896 221 58 221 1 0 16 3.4e-12 1.1e-13
80 0.55228 0.014779 223 59 223 1 0 16 7.3e-13 1.5e-13
81 0.58184 0.029558 225 60 225 1 0 16 4e-12 1.9e-13
- 0.6 - out
82 0.61139 0.029558 226 60 226 1 0 16 5.7e-12 2.2e-13
83 0.64095 0.029558 227 60 227 1 0 16 8.1e-12 1.7e-13
84 0.64095 1.0148e-07 269 70 269 1 0 25 9.3e-16 2.5e-15
85 0.64095 2.0296e-07 271 71 271 1 0 25 8.7e-16 7.9e-15
86 0.64095 1.0148e-07 276 73 276 1 0 26 5.7e-16 3.9e-15
87 0.64095 2.0296e-07 278 74 278 1 0 26 1.1e-15 1.4e-14
88 0.64095 2.0296e-07 279 74 279 1 0 26 1.6e-15 1.5e-14

89 0.64095 1.2685e-08 293 77 293 1 0 28 1.5e-16 4.8e-16
90 0.64095 2.537e-08 295 78 295 1 0 28 2.3e-16 1.4e-15
91 0.64095 1.2685e-08 301 80 301 1 0 29 1.5e-16 4.9e-16
92 0.64095 2.537e-08 303 81 303 1 0 29 4.4e-16 1.5e-15
93 0.64095 2.537e-08 304 81 304 1 0 29 3.6e-16 2.3e-15
94 0.64095 3.6351e-09 311 83 311 1 1 30 1.7e-16 2.4e-16
95 0.64095 7.2702e-09 313 84 313 1 1 30 1.7e-16 6.7e-16
96 0.64095 7.2702e-09 314 84 314 1 1 30 2.1e-16 5.1e-16
97 0.64095 7.2702e-09 315 84 315 1 1 30 2.1e-16 6.7e-16
98 0.64095 4.034e-10 329 87 329 1 1 32 1.5e-16 1.3e-16
99 0.64095 8.068e-10 331 88 331 1 1 32 1.5e-16 2.3e-16
100 0.64095 4.034e-10 337 90 337 1 1 33 8e-17 8.5e-17
101 0.64095 8.068e-10 339 91 339 1 1 33 1.5e-16 1.9e-16
102 0.64095 8.068e-10 340 91 340 1 1 33 1.2e-16 2.2e-16
103 0.64095 8.068e-10 341 91 341 1 1 33 1.2e-16 2.5e-16
104 0.64095 3.7422e-11 355 94 355 1 1 35 1.8e-16 1.8e-16
105 0.64095 1.8711e-11 360 96 360 1 1 36 1.5e-16 1.8e-16
106 0.64095 3.7422e-11 362 97 362 1 1 36 1.6e-16 1.4e-16
107 0.64095 1.8711e-11 368 99 368 1 1 37 1.5e-16 1.7e-16
108 0.64095 9.3555e-12 373 101 373 1 1 38 1.9e-16 2.1e-16

109 0.64095 1.8711e-
11 375 102 375 1 1 38 1.8e-16 2.8e-16
110 0.64095 9.3555e-
12 381 104 381 1 1 39 1.6e-16 1.3e-16
111 0.64095 1.8711e-
11 383 105 383 1 1 39 2.6e-16 2.4e-16
112 0.64095 1.8711e-
11 384 105 384 1 1 39 4.7e-17 2.3e-16
113 0.64095 4.6778e-
12 394 107 394 1 1 40 2.1e-16 2.6e-16
114 0.64095 4.6778e-
12 395 107 395 1 1 40 4.6e-17 7.6e-17
115 0.64095 4.6778e-
12 396 107 396 1 1 40 9.8e-17 1.6e-16
116 0.64095 2.3389e-
12 405 109 405 2 1 41 1.6e-16 1.7e-16
117 0.64095 4.6778e-
12 407 110 407 2 1 41 1.9e-16 2e-16
118 0.64095 4.6778e-
12 408 110 408 2 1 41 9.2e-17 2.8e-16
119 0.64095 1.1694e-
12 418 112 418 2 1 42 6.1e-16 5.4e-16
120 0.64095 5.8472e-
13 424 114 424 2 1 43 8.4e-17 1e-16
121 0.64095 1.1694e-
12 426 115 426 2 1 43 3.4e-16 4.3e-16
122 0.64095 1.1694e-
12 427 115 427 2 1 43 4e-16 3.5e-16
123 0.64095 1.1694e-
12 428 115 428 2 1 43 1.8e-16 2e-16
124 0.64095 1.4959e-
13 435 117 435 2 2 44 8.7e-17 8.7e-17
125 0.64095 7.4794e-
14 441 119 441 2 2 45 5.1e-17 6.9e-17
126 0.64095 1.4959e-
13 443 120 443 2 2 45 2.8e-16 3.2e-16
127 0.64095 1.4959e-
13 444 120 444 2 2 45 9e-17 1.9e-16
128 0.64095 1.4959e-
13 445 120 445 2 2 45 1.5e-16 1.6e-16

129 0.64095 1.4959e-
13 446 120 446 2 2 45 1e-16 2.3e-16
130 0.64095 9.3493e-
15 460 123 460 3 2 47 8.3e-17 9e-17
131 0.64095 1.8699e-
14 462 124 462 3 2 47 8.1e-17 1.7e-16
132 0.64095 9.3493e-
15 468 126 468 3 2 48 1.4e-16 3.1e-16
133 0.64095 4.6746e-
15 474 128 474 3 2 49 4.7e-17 9.6e-17
134 0.64095 9.3493e-
15 476 129 476 3 2 49 9e-17 2.5e-16
135 0.64095 9.3493e-
15 477 129 477 3 2 49 2.9e-16 4.2e-16
136 0.64095 1.6325e-
15 488 131 488 3 3 50 7.1e-17 1.3e-16
137 0.64095 3.265e-
15 490 132 490 3 3 50 3.2e-17 3.3e-16
138 0.64095 8.1625e-
16 500 134 500 3 3 51 2.3e-16 2.3e-16
138 0.64095 8.1625e-
16 out 504 135 504 3 3 52 1e-16 7.9e-16
Solution time: 195 s. (3 minutes, 15 seconds)
Physical memory: 1.35 GB
Virtual memory: 1.51 GB
Ended at Oct 24, 2023 2:01:34 PM.
----- Time-Dependent Solver 1 in Study 1/Solution 1 (sol1) -------
---------->

Fully Coupled 1 (fc1)

Appendix H

Modeling of pH Gradients under ac Fields in Comsol

Attached is a complete report of modeling of pH gradients under low frequency ac fields generated from COMSOL MULTIPHYSICS. The report provides a complete demonstration of the model setup at COMSOL interface. The first section provides details of the parameters used in the model. The second section describes the geometry, variables, functions and tertiary current distribution module, mesh setup used for solving the pH profiles. The time dependant setup and solver configuration are described in the last section.

1 Global Definitions

Date	Nov 9, 2021 10:14:12 AM

GLOBAL SETTINGS

Name	Paper replicate Behrouz.mph
Path	C:\Users\behdanb\Documents\Kun Simulation\paper replicate_Behrouz.mph
Version	COMSOL Multiphysics 5.6 (Build: 401)
Unit system	SI

USED PRODUCTS

COMSOL Multiphysics
Electrochemistry Module

COMPUTER INFORMATION

CPU	Intel64 Family 6 Model 85 Stepping 7, 8 cores
Operating system	Windows Server 2019

1.1 PARAMETERS

1.1.1 Parameters 2

PARAMETERS 2

Name	Expression	Value	Description
h_el	2.4[cm]	0.024 m	
d_els	1.35[cm]	0.0135 m	
h_cell	3.0[cm]	0.03 m	
h_el_b	0.1[cm]	0.001 m	
D_H	9.3e-5[cm^2/s]	9.3E−9 m²/s	
D_OH	5.3e-5[cm^2/s]	5.3E−9 m²/s	
D_H3PO4	0.65e-5[cm^2]	6.5E−10 m²	
D_H2PO4	0.85e-5[cm^2]	8.5E−10 m²	
D_HPO4	0.65e-5[cm^2]	6.5E−10 m²	

Name	Expression	Value	Description
D_PO4	0.72e-5[cm^2]	7.2E−10 m²	
D_K	1.96e-5[cm^2]	1.96E−9 m²	
Eeq_a	1.23[V]	1.23 V	
Eeq_c	0[V]	0 V	
Ecell	1.5[V]	1.5 V	
j_app	1[mA/cm^2]	10 A/m²	
i0_a	1E-4[A/m^2]	1E−4 A/m²	
i0_c	10[A/m^2]	10 A/m²	
c_inH	10^ - 6.7[mol/l]	1.9953E−4 mol/m³	
c_inH3PO4	c_inH/1[mol/l]/K1*c_inH2PO4	0.0015186	
c_inH2PO4	c_inH/1[mol/l]/K2*c_inHPO4	57.084	
c_inHPO4	1/(1 + c_inH/(K2*1[mol/l]) + c_inH^2/(K1*K2*1[mol^2/l^2] + K3*1[mol/l]/c_inH))*0.1[mol/l]	42.915	
c_inPO4	K3*1[mol/l]/c_inH*c_inHPO4	4.6028E−5	
K1	7.5e-3	0.0075	
K2	1.5e-7	1.5E−7	
K3	2.14e-13	2.14E−13	
T	298[K]	298 K	
h_in_out	0.9[cm]	0.009 m	
gap_in_out	0.01[cm]	1E−4 m	
D_O2	2.4e-5[cm^2/s]	2.4E−9 m²/s	
D_H2	5e-5[cm^2/s]	5E−9 m²/s	

2 Component 1

Date	Nov 8, 2021 10:18:25 AM

SETTINGS

Description	Value
Unit system	Same as global system (SI)
Geometry shape function	Automatic

SPATIAL FRAME COORDINATES

First	Second	Third
x	y	z

MATERIAL FRAME COORDINATES

First	Second	Third
X	Y	Z

GEOMETRY FRAME COORDINATES

First	Second	Third
Xg	Yg	Zg

MESH FRAME COORDINATES

First	Second	Third
Xm	Ym	Zm

2.1 DEFINITIONS

2.1.1 Variables

Variables 1

SELECTION

Geometric entity level	Entire model

Name	Expression	Unit	Description
Eeq_a_pH	root.comp1.Eeq_a_nernst(cH, c_inH)	V	
Eeq_c_pH	root.comp1.Eeq_c_nernst(cH, c_inH)	V	

Variables 2

SELECTION

Geometric entity level	Entire model

Name	Expression	Unit	Description
rho_PO4	root.comp1.RHO(cK, cH3PO4 + cH2PO4 + cPO4)		

2.1.2 Functions

Eeq_a_nernst

Function name	Eeq_a_nernst
Function type	Analytic

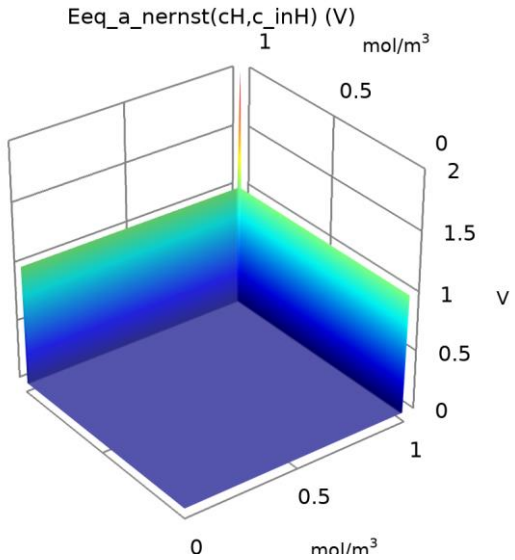

Eeq_a_nernst

DEFINITION

Description	Value
Expression	0*(cH<1) + 0*(c_inH<1) + 1*(cH>=1) + 1*(c_inH>=1)
Arguments	{cH, c_inH}

UNITS

Description	Value
Arguments	mol/m^3
Function	V

Eeq_c_nernst

Function name	Eeq_c_nernst
Function type	Analytic

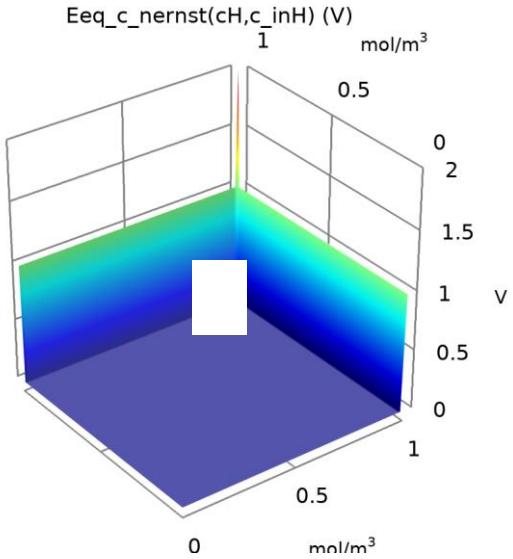

Eeq_c_nernst

DEFINITION

Description	Value
Expression	0*(cH<1) + 0*(c_inH<1) + 1*(cH>=1) + 1*(c_inH>=1)
Arguments	{cH, c_inH}

UNITS

Description	Value
Arguments	mol/m^3
Function	V

RHO

Function names	RHO
Function type	Interpolation

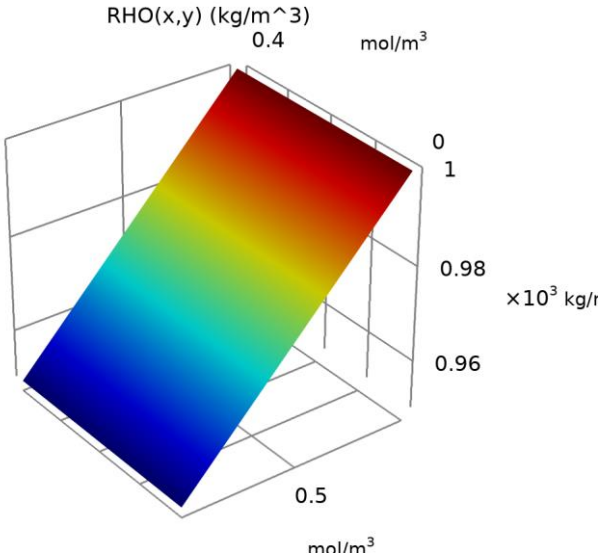

RHO

INTERPOLATION AND EXTRAPOLATION

Description	Value
Extrapolation	Linear

UNITS

Description	Value
Arguments	mol/m^3
Function	kg/m^3

2.2 GEOMETRY 1

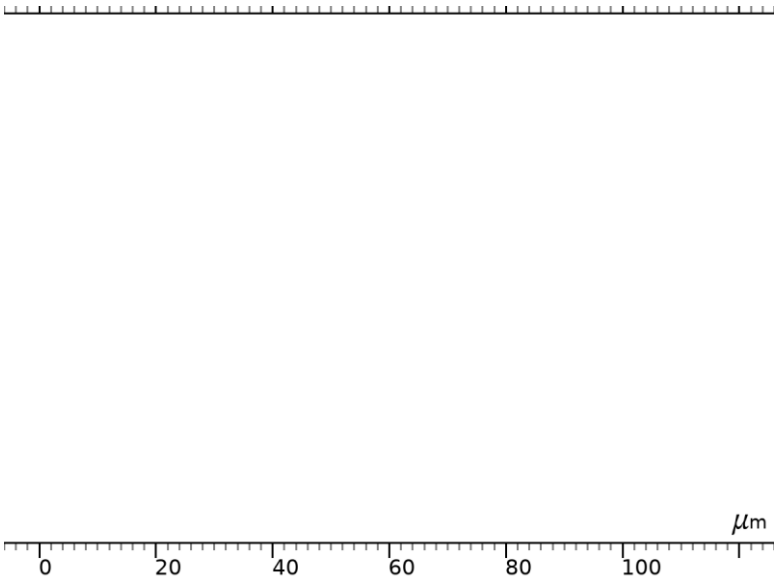

Geometry 1

UNITS

Length unit	µm
Angular unit	deg

GEOMETRY STATISTICS

Description	Value
Space dimension	1
Number of domains	0
Number of boundaries	0

2.3 TERTIARY CURRENT DISTRIBUTION, NERNST-PLANCK

USED PRODUCTS

COMSOL Multiphysics
Electrochemistry Module

Tertiary Current Distribution, Nernst-Planck

SELECTION

Geometric entity level	Domain

Selection	Geometry geom1: Dimension 1: All domains

EQUATIONS

$$\frac{\partial c_i}{\partial t} + \nabla \cdot \mathbf{J}_i + \mathbf{u} \cdot \nabla c_i = R_i$$
$$\nabla \cdot \mathbf{i}_l = F \sum_i z_i R_i + Q_l$$
$$\nabla \cdot \mathbf{i}_s = -F \sum_i z_i R_i + Q_s$$
$$\sum_i z_i c_i = 0$$
$$\mathbf{J}_i = -D_i \nabla c_i - z_i u_{m,i} F c_i \nabla \phi_l$$
$$\mathbf{i}_l = F \sum_i z_i \mathbf{J}_i$$
$$\mathbf{i}_s = -\sigma_s \nabla \phi_s$$
$$\phi_l = \text{phil}, \quad \phi_s = \text{phis}$$

2.3.1 Interface Settings

Discretization

SETTINGS

Description	Value
Concentration	Quadratic
Electrolyte po al	Quadratic
Electric potent...	Quadratic

Cross-Sectional Area

SETTINGS

Description	Value
Cross-sectional area	1[m^2]

Electrolyte Charge Conservation

SETTINGS

Description	Value
Charge conservation model	Electroneutrality
From electroneutrality	cNa

Physics vs. Materials Reference Electrode Potential

SETTINGS

Description	Value
Physics vs. materials reference electrode potential	0 V

2.3.2 Variables

Name	Expression	Unit	Description	Selection	Details
tcd.mulstopcond	1	1	Multiplicative stop condition	Global	* operation
tcd.stopcond	tcd.mulstopcond	1	Solver stop condition	Global	

2.3.3 Electrolyte 1

Electrolyte 1

SELECTION

Geometric entity level	Domain
Selection	Geometry geom1: Dimension 1: All domains

EQUATIONS

$$\frac{\partial c_i}{\partial t} + \nabla \cdot \mathbf{J}_i + \mathbf{u} \cdot \nabla c_i = R_i$$

$$\nabla \cdot \mathbf{i}_l = F \sum_i z_i R_i + Q_l$$

$$\sum_i z_i c_i = 0$$

$$\mathbf{J}_i = -D_i \nabla c_i - z_i u_{m,i} F c_i \nabla \phi_l$$

$$\mathbf{i}_l = F \sum_i z_i \mathbf{J}_i$$

Convection

SETTINGS

Description	Value
Velocity field	User defined
Velocity field	{0, 0, 0}

Diffusion

SETTINGS

Description	Value
Material	None
Diffusion coefficient	User defined
Diffusion coefficient	{{9.3e-9[m^2/s], 0, 0}, {0, 9.3e-9[m^2/s], 0}, {0, 0, 9.3e-9[m^2/s]}}
Diffusion coefficient	User defined
Diffusion coefficient	{{5.3e-9[m^2/s], 0, 0}, {0, 5.3e-9[m^2/s], 0}, {0, 0, 5.3e-9[m^2/s]}}
Diffusion coefficient	User defined
Diffusion coefficient	{{1.3e-9[m^2/s], 0, 0}, {0, 1.3e-9[m^2/s], 0}, {0, 0, 1.3e-9[m^2/s]}}

Migration in Electric Field

SETTINGS

Description	Value
Mobility	Nernst - Einstein relation
Charge number	{1, -1, 1}

Coordinate System Selection

SETTINGS

Description	Value
Coordinate system	Global coordinate system

Model Input

SETTINGS

Description	Value
Temperature	Common model input

Shape functions

Name	Shape function	Unit	Description	Shape frame	Selection
cH	Lagrange (Quadratic)	mol/m³	Concentration	Spatial	No domains
cOH	Lagrange (Quadratic)	mol/m³	Concentration	Spatial	No domains
phil	Lagrange (Quadratic)	V	Electrolyte potential	Spatial	No domains

2.3.4 No Flux 1

No Flux 1

SELECTION

Geometric entity level	Boundary
Selection	Geometry geom1: Dimension 0: All boundaries

EQUATIONS

$$-\mathbf{n}\cdot\mathbf{J}_i = 0$$

Convection

SETTINGS

Description	Value
Include	Off

2.3.5 Insulation 1

SELECTION

Geometric entity level	Boundary

Selection	Geometry geom1: Dimension 0: All boundaries

EQUATIONS

$$-\mathbf{n}\cdot\mathbf{i}_l = 0, \quad -\mathbf{n}\cdot\mathbf{i}_s = 0$$

2.3.6 Initial Values 1

Initial Values 1

SELECTION

Geometric entity level	Domain
Selection	Geometry geom1: Dimension 1: All domains

Initial Values

SETTINGS

Description	Value
Concentration	{cinH, cinOH, 0}
Electrolyte potential	0
Electric potential	0

2.3.7 Electrode Surface 1

Electrode Surface 1

SELECTION

Geometric entity level	Boundary
Selection	Geometry geom1: Dimension 0: No boundaries

EQUATIONS

$$\int_{\partial\Omega} \mathbf{i}_l \cdot \mathbf{n}\,dl = i_{l,average} \int_{\partial\Omega} dl$$

$$\mathbf{n}\cdot\mathbf{i}_l = i_{total}$$

$$i_{total} = \sum_m i_{loc,m} + i_{dl}$$

$$-\mathbf{n}\cdot\mathbf{J}_i = R_{i,\mathrm{tot}}, \quad R_{i,\mathrm{tot}} = \sum_m R_{i,m} + R_{\mathrm{dl},i}$$

Dissolving-Depositing Species

SETTINGS

Description	Value
Species	
Solve for surface concentration variables	On

Film Resistance

SETTINGS

Description	Value
Film resistance	No film resistance

Harmonic Perturbation

SETTINGS

Description	Value
Perturbation amplitude	0[A/m^2]

Electrode Phase Potential Condition

SETTINGS

Description	Value
Electrode phase potential condition	Average current density
	Japp
Boundary electric potential initial value	1.23

Electrode Reaction 1

Electrode Reaction 1

SELECTION

Geometric entity level	Boundary
Selection	Geometry geom1: Dimension 0: All boundaries

EQUATIONS

$$\eta = E_{ct} - E_{eq}, \quad E_{ct} = \phi_{s,ext} - \phi_l$$
$$R_i = \frac{-\nu_i i_{loc}}{nF}$$

Stoichiometric Coefficients

SETTINGS

Description	Value
Number of participating electrons	1
Stoichiometric coefficient	{-1, 0, 0}

Equilibrium Potential

SETTINGS

Description	Value
Equilibrium potential	User defined
Equilibrium potential	Eeq_a_pH

Electrode Kinetics

SETTINGS

Description	Value
Local current density expression	From kinetics expression
Kinetics expression type	Butler - Volmer
Exchange current density	i0_a
Anodic transfer coefficient	1.9
Cathodic transfer coefficient	0.1
Limiting current density	Off

Heat of Reaction

SETTINGS

Description	Value
Specify	Temperature derivative
Temperature derivative of equilibrium potential	User defined
Temperature derivative of equilibrium potential	0

Model Input

SETTINGS

Description	Value
Temperature	Common model input

2.3.8 Electrode Surface 2

Electrode Surface 2

SELECTION

Geometric entity level	Boundary
Selection	Geometry geom1: Dimension 0: No boundaries

EQUATIONS

$$\mathbf{n} \cdot \mathbf{i}_l = i_{\text{total}}$$
$$i_{\text{total}} = \sum_m i_{\text{loc},m} + i_{\text{dl}}$$
$$-\mathbf{n} \cdot \mathbf{J}_i = R_{i,\text{tot}}, \quad R_{i,\text{tot}} = \sum_m R_{i,m} + R_{\text{dl},i}$$

Dissolving-Depositing Species

SETTINGS

Description	Value
Species	
Solve for surface concentration variables	On

Film Resistance

SETTINGS

Description	Value
Film resistance	No film resistance

Harmonic Perturbation

SETTINGS

Description	Value
Perturbation amplitude	0[V]

Electrode Phase Potential Condition

SETTINGS

Description	Value
Electrode phase potential condition	Electric potential

Description	Value
External electric potential	0[V]

Electrode Reaction 1

Electrode Reaction 1

SELECTION

Geometric entity level	Boundary
Selection	Geometry geom1: Dimension 0: All boundaries

EQUATIONS

$$\eta = E_{ct} - E_{eq}, \quad E_{ct} = \phi_{s,ext} - \phi_l$$

$$R_j = \frac{-\nu_j i_{loc}}{nF}$$

Stoichiometric Coefficients

SETTINGS

Description	Value
Number of participating electrons	1
Stoichiometric coefficient	{-1, 0, 0}

Equilibrium Potential

SETTINGS

Description	Value
Equilibrium potential	User defined
Equilibrium potential	Eeq_c_pH

Electrode Kinetics

SETTINGS

Description	Value
Local current density expression	From kinetics expression
Kinetics expression type	Butler - Volmer
Exchange current density	i0_c
Anodic transfer coefficient	0.5
Cathodic transfer coefficient	0.5
Limiting current density	Off

Heat of Reaction

SETTINGS

Description	Value
Specify	Temperature derivative
Temperature derivative of equilibrium potential	User defined
Temperature derivative of equilibrium potential	0

Model Input

SETTINGS

Description	Value
Temperature	Common model input

2.4 MESH 1

Mesh 1

MESH STATISTICS

Description	Value
Minimum element quality	0.0
Average element quality	0.0

2.4.1 Size (size)

SETTINGS

Description	Value
Maximum element size	0.01
Minimum element size	2.0E-5
Curvature factor	0.2
Predefined size	Extremely fine

2.4.2 Size 1 (size1)

SELECTION

Geometric entity level	Boundary

Selection	Geometry geom1: Dimension 0: No boundaries

Size 1

SETTINGS

Description	Value
Maximum element size	0.01
Minimum element size	2.0E-5
Curvature factor	0.2
Predefined size	Extremely fine

2.4.3 Edge 1 (edg1)

SELECTION

Geometric entity level	Remaining

Edge 1

Distribution 1 (dis1)

SELECTION

Geometric entity level	Domain
Selection	Geometry geom1: Dimension 1: No domains

Distribution 1

SETTINGS

Description	Value
Number of elements	1000

3 Study 1

COMPUTATION INFORMATION

Computation time	2 s

3.1 TIME DEPENDENT

Times	Unit
range(0,0.1,1)	s

STUDY SETTINGS

Description	Value
Include geometric nonlinearity	Off

STUDY SETTINGS

Description	Value
Output times	{0, 0.1, 0.2, 0.30000000000000004, 0.4, 0.5, 0.6000000000000001, 0.7000000000000001, 0.8, 0.9, 1}

PHYSICS AND VARIABLES SELECTION

Physics interface	Discretization
Tertiary Current Distribution, Nernst-Planck (tcd)	physics

MESH SELECTION

Geometry	Mesh
Geometry 1 (geom1)	mesh1

3.2 SOLVER CONFIGURATIONS

3.2.1 Solution 1

Compile Equations: Time Dependent (st1)

STUDY AND STEP

Description	Value
Use study	Study 1
Use study step	Time Dependent

LOG

References

[1] O. Gang and Y. Zhang, "Shaping phases by phasing shapes," *ACS nano*, vol. 5, no. 11, pp. 8459–8465, 2011.

[2] A. A. Shah, B. Schultz, W. Zhang, S. C. Glotzer, and M. J. Solomon, "Actuation of shape-memory colloidal fibres of janus ellipsoids," *Nature materials*, vol. 14, no. 1, pp. 117–124, 2015.

[3] M. Ganesan and M. J. Solomon, "High-density equilibrium phases of colloidal ellipsoids by application of optically enhanced, direct current electric fields," *Soft Matter*, vol. 13, no. 20, pp. 3768–3776, 2017.

[4] W. Ristenpart, P. Jiang, M. Slowik, C. Punckt, D. Saville, and I. A. Aksay, "Electrohydrodynamic flow and colloidal patterning near inhomogeneities on electrodes," *Langmuir*, vol. 24, no. 21, pp. 12172–12180, 2008.

[5] A. A. Shah, M. Ganesan, J. Jocz, and M. J. Solomon, "Direct current electric field assembly of colloidal crystals displaying reversible structural color.," *ACS Nano*, vol. 8, pp. 8095–103, 2014.

[6] H. Zhou, L. R. White, and R. D. Tilton, "Lateral separation of colloids or cells by dielectrophoresis augmented by ac electroosmosis," *Journal of colloid and interface science*, vol. 285, no. 1, pp. 179–191, 2005.

[7] M. M. Panczyk, J.-G. Park, N. J. Wagner, and E. M. Furst, "Two-dimensional directed assembly of dicolloids," *Langmuir*, vol. 29, no. 1, pp. 75–81, 2013.

[8] K. D. Hermanson, S. O. Lumsdon, J. P. Williams, E. W. Kaler, and O. D. Velev, "Dielectrophoretic assembly of electrically functional microwires from nanoparticle suspensions," *Science*, vol. 294, no. 5544, pp. 1082–1086, 2001.

[9] Y. Huang, S. Joo, M. Duhon, M. Heller, B. Wallace, and X. Xu, "Dielectrophoretic cell separation and gene expression profiling on microelectronic chip arrays," *Analytical chemistry*, vol. 74, no. 14, pp. 3362–3371, 2002.

[10] S. C. Bukosky, A. Hashemi, S. P. Rader, J. Mora, G. H. Miller, and W. D. Ristenpart, "Extreme levitation of colloidal particles in response to oscillatory electric fields," *Langmuir*, vol. 35, no. 21, pp. 6971–6980, 2019.

[11] W. Ristenpart, I. A. Aksay, and D. Saville, "Electrically guided assembly of planar superlattices in binary colloidal suspensions," *Physical review letters*, vol. 90, no. 12, p. 128303, 2003.

[12] A. F. Demirors and L. Alison, "Electric field assembly of colloidal superstructures," *The Journal of Physical Chemistry Letters*, vol. 9, no. 15, pp. 4437–4443, 2018.

[13] N. Sidelman, M. Cohen, A. Kolbe, Z. Zalevsky, A. Herrman, and S. Richter, "Rapid Particle Patterning in Surface Deposited Micro-Droplets of Low Ionic Content via Low-Voltage Electrochemistry and Electrokinetics," *Scientific Reports*, vol. 5, no. 1, p. 13095, 2015.

[14] C. A. Silvera Batista, H. Rezvantalab, R. G. Larson, and M. J. Solomon, "Controlled Levitation of Colloids through Direct Current Electric Fields," *Langmuir*, vol. 33, no. 41, pp. 10861 – 10867, 2017.

[15] S. C. Glotzer and M. J. Solomon, "Anisotropy of building blocks and their assembly into complex structures," *Nature materials*, vol. 6, no. 8, pp. 557–562, 2007.

[16] Z. Li, *Flat Optics for Light Steering and Spectrum Engineering at the Nanoscale*. PhD thesis, Northwestern University, 2017.

[17] C. A. Silvera Batista, R. G. Larson, and N. A. Kotov, "Nonadditivity of nanoparticle interactions," *Science*, vol. 350, no. 6257, p. 1242477, 2015.

[18] K. J. Bishop, C. E. Wilmer, S. Soh, and B. A. Grzybowski, "Nanoscale forces and their uses in self-assembly," *small*, vol. 5, no. 14, pp. 1600–1630, 2009.

[19] Q. Chen, S. C. Bae, and S. Granick, "Directed self-assembly of a colloidal kagome lattice," *Nature*, vol. 469, no. 7330, pp. 381–384, 2011.

[20] Q. Chen, J. K. Whitmer, S. Jiang, S. C. Bae, E. Luijten, and S. Granick, "Supracolloidal reaction kinetics of janus spheres," *Science*, vol. 331, no. 6014, pp. 199–202, 2011.

[21] H. Lin, S. Lee, L. Sun, M. Spellings, M. Engel, S. C. Glotzer, and C. A. Mirkin, "Clathrate colloidal crystals," *Science*, vol. 355, no. 6328, pp. 931–935, 2017.

[22] K. Schätzel and B. J. Ackerson, "Density fluctuations during crystallization of colloids," *Physical Review E*, vol. 48, no. 5, p. 3766, 1993.

[23] M. J. Solomon, "Tools and functions of reconfigurable colloidal assembly," *Langmuir*, vol. 34, no. 38, pp. 11205–11219, 2018.

[24] J. Palacci, S. Sacanna, A. P. Steinberg, D. J. Pine, and P. M. Chaikin, "Living Crystals of Light-Activated Colloidal Surfers," *Science*, vol. 339, p. 936 940, 2013.

[25] I. Theurkauff, C. Cottin-Bizonne, J. Palacci, C. Ybert, and L. Bocquet, "Dynamic clustering in active colloidal suspensions with chemical signaling," *Physical review letters*, vol. 108, no. 26, p. 268303, 2012.

[26] F. Ma, D. T. Wu, and N. Wu, "Formation of colloidal molecules induced by alternating-current electric fields," *Journal of the American Chemical Society*, vol. 135, no. 21, pp. 7839–7842, 2013.

[27] J. Yan, M. Han, J. Zhang, C. Xu, E. Luijten, and S. Granick, "Reconfiguring active particles by electrostatic imbalance," *Nature materials*, vol. 15, no. 10, pp. 1095–1099, 2016.

[28] A. Bricard, J.-B. Caussin, N. Desreumaux, O. Dauchot, and D. Bartolo, "Emergence of macroscopic directed motion in populations of motile colloids," *Nature*, vol. 503, no. 7474, pp. 95–98, 2013.

[29] E. M. Furst, "Directed self-assembly," *Soft Matter*, vol. 9, no. 38, pp. 9039–9045, 2013.

[30] J. H. Holtz and S. A. Asher, "Polymerized colloidal crystal hydrogel films as intelligent chemical sensing materials," *Nature*, vol. 389, no. 6653, pp. 829–832, 1997.

[31] J. M. Weissman, H. B. Sunkara, A. S. Tse, and S. A. Asher, "Thermally switchable periodicities and diffraction from mesoscopically ordered materials," *Science*, vol. 274, no. 5289, pp. 959–963, 1996.

[32] K. J. Lee, J. Yoon, S. Rahmani, S. Hwang, S. Bhaskar, S. Mitragotri, and J. Lahann, "Spontaneous shape reconfigurations in multicompartmental microcylinders," *Proceedings of the National Academy of Sciences*, vol. 109, no. 40, pp. 16057–16062, 2012.

[33] M. Youssef, T. Hueckel, G.-R. Yi, and S. Sacanna, "Shape-shifting colloids via stimulated dewetting," *Nature communications*, vol. 7, no. 1, p. 12216, 2016.

[34] W. B. Russel, W. Russel, D. A. Saville, and W. R. Schowalter, *Colloidal dispersions*. Cambridge university press, 1991.

[35] B. Bharti and O. D. Velev, "Assembly of reconfigurable colloidal structures by multidirectional field-induced interactions," *Langmuir*, vol. 31, no. 29, pp. 7897–7908, 2015.

[36] T. C. Halsey and W. Toor, "Structure of electrorheological fluids," *Physical review letters*, vol. 65, no. 22, p. 2820, 1990.

[37] A. Yethiraj, A. Wouterse, B. Groh, and A. van Blaaderen, "Nature of an electric-field-induced colloidal martensitic transition," *Physical review letters*, vol. 92, no. 5, p. 058301, 2004.

[38] A.-P. Hynninen and M. Dijkstra, "Phase diagram of dipolar hard and soft spheres: Manipulation of colloidal crystal structures by an external field," *Physical review letters*, vol. 94, no. 13, p. 138303, 2005.

[39] S. Gangwal, A. Pawar, I. Kretzschmar, and O. D. Velev, "Programmed assembly of metallodielectric patchy particles in external ac electric fields," *Soft Matter*, vol. 6, no. 7, pp. 1413–1418, 2010.

[40] A. A. Shah, B. Schultz, W. Zhang, S. C. Glotzer, and M. J. Solomon, "Actuation of shape-memory colloidal fibres of Janus ellipsoids.," *Nature Materials*, vol. 14, no. 1, pp. 117–124, 2015.

[41] M. Mittal and E. M. Furst, "Electric field-directed convective assembly of ellipsoidal colloidal particles to create optically and mechanically anisotropic thin films," *Advanced Functional Materials*, vol. 19, no. 20, pp. 3271–3278, 2009.

[42] J. J. Crassous, A. M. Mihut, E. Wernersson, P. Pfleiderer, J. Vermant, P. Linse, and P. Schurtenberger, "Field-induced assembly of colloidal ellipsoids into well-defined microtubules," *Nature communications*, vol. 5, no. 1, p. 5516, 2014.

[43] D. Velegol, A. Garg, R. Guha, A. Kar, and M. Kumar, "Origins of concentration gradients for diffusiophoresis," *Soft matter*, vol. 12, no. 21, pp. 4686–4703, 2016.

[44] M. E. Leunissen, M. T. Sullivan, P. M. Chaikin, and A. Van Blaaderen, "Concentrating colloids with electric field gradients. i. particle transport and growth mechanism of hard-sphere-like crystals in an electric bottle," *The Journal of chemical physics*, vol. 128, no. 16, 2008.

[45] S. C. Takatori, W. Yan, and J. F. Brady, "Swim pressure: stress generation in active matter," *Physical review letters*, vol. 113, no. 2, p. 028103, 2014.

[46] O. D. Velev and K. H. Bhatt, "On-chip micromanipulation and assembly of colloidal particles by electric fields," *Soft Matter*, vol. 2, no. 9, pp. 738–750, 2006.

[47] M. Trau, D. Saville, and I. A. Aksay, "Assembly of colloidal crystals at electrode interfaces," *Langmuir*, vol. 13, no. 24, pp. 6375–6381, 1997.

[48] Y. Solomentsev, M. Böhmer, and J. L. Anderson, "Particle clustering and pattern formation during electrophoretic deposition: a hydrodynamic model," *Langmuir*, vol. 13, no. 23, pp. 6058–6068, 1997.

[49] J. Kim, J. L. Anderson, S. Garoff, and P. J. Sides, "Effects of zeta potential and electrolyte on particle interactions on an electrode under ac polarization," *Langmuir*, vol. 18, no. 14, pp. 5387–5391, 2002.

[50] K. D. Barbee, A. P. Hsiao, M. J. Heller, and X. Huang, "Electric field directed assembly of high-density microbead arrays," *Lab on a Chip*, vol. 9, no. 22, pp. 3268–3274, 2009.

[51] M. Holgado, F. Garcia-Santamaria, A. Blanco, M. Ibisate, A. Cintas, H. Miguez, C. Serna, C. Molpeceres, J. Requena, A. Mifsud, *et al.*, "Electrophoretic deposition to control artificial opal growth," *Langmuir*, vol. 15, no. 14, pp. 4701–4704, 1999.

[52] K. H. Bhatt and O. D. Velev, "Control and modeling of the dielectrophoretic assembly of on-chip nanoparticle wires," *Langmuir*, vol. 20, no. 2, pp. 467–476, 2004.

[53] A. Hashemi, S. C. Bukosky, S. P. Rader, W. D. Ristenpart, and G. H. Miller, "Oscillating electric fields in liquids create a long-range steady field," *Physical review letters*, vol. 121, no. 18, p. 185504, 2018.

[54] S. C. Bukosky, S. M. H. H. Amrei, S. P. Rader, J. Mora, G. H. Miller, and W. D. Ristenpart, "Extreme Levitation of Colloidal Particles in Response to Oscillatory Electric Fields," *Langmuir*, vol. 35, no. 21, pp. 6971–6980, 2019.

[55] T. Yu, P. Chuphal, S. Thakur, S. Y. Reigh, D. P. Singh, and P. Fischer, "Chemical micromotors self-assemble and self-propel by spontaneous symmetry breaking," *Chemical Communications*, vol. 54, no. 84, pp. 11933–11936, 2018.

[56] I. Ziemecka, G. J. Koper, A. G. Olive, and J. H. van Esch, "Chemical-gradient directed self-assembly of hydrogel fibers," *Soft Matter*, vol. 9, no. 5, pp. 1556–1561, 2013.

[57] L. Cera, L. Chiappisi, C. Böttcher, A. Schulz, S. Schoder, M. Gradzielski, and C. A. Schalley, "Polywhips: Directional particle transport by gradient-directed growth and stiffening of supramolecular assemblies," *Advanced Materials*, vol. 29, no. 8, p. 1604430, 2017.

[58] F. Qi, Z. Meng, M. Xue, and L. Qiu, "Recent advances in self-assemblies and sensing applications of colloidal photonic crystals," *Analytica Chimica Acta*, vol. 1123, pp. 91–112, 2020.

[59] J. Zhu and M. C. Hersam, "Assembly and electronic applications of colloidal nanomaterials," *Advanced Materials*, vol. 29, no. 4, p. 1603895, 2017.

[60] T. J. Woehl, K. L. Heatley, C. S. Dutcher, N. H. Talken, and W. D. Ristenpart, "Electrolyte-Dependent Aggregation of Colloidal Particles near Electrodes in Oscillatory Electric Fields," *Langmuir*, vol. 30, pp. 4887 – 4894, 05 2014.

[61] S.-R. Yeh, M. Seul, and B. I. Shraiman, "Assembly of ordered colloidal aggregrates by electric-field-induced fluid flow," *Nature*, vol. 386, no. 6620, pp. 57–59, 1997.

[62] M. Ammam, "Electrophoretic deposition under modulated electric fields: a review," *Rsc Advances*, vol. 2, no. 20, pp. 7633–7646, 2012.

[63] R. A. Rica and M. Z. Bazant, "Electrodiffusiophoresis: Particle motion in electrolytes under direct current," *Physics of Fluids*, vol. 22, no. 11, 2010.

[64] J. S. Newman and K. E. Thomas-Alyea, *Electrochemical systems*. Hoboken, N.J.: John Wiley & Sons, 3rd ed., 2004.

[65] M. von Smoluchowski, *Elektrische Endosmose und Strömungsströme*, vol. II. Leipzig: J.A. Barth, 1921.

[66] D. C. Henry, "The Cataphoresis of Suspended Particles. Part I. The Equation of Cataphoresis," *Proceedings of the Royal Society A: Mathematical, Physical and Engineering Sciences*, vol. 133, pp. 106–129, 1931.

[67] D. C. Prieve, J. L. Anderson, J. P. Ebel, and M. E. Lowell, "Motion of a particle generated by chemical gradients. part 2. electrolytes," *Journal of Fluid Mechanics*, vol. 148, p. 247–269, 1984.

[68] J. L. Anderson, "Colloid Transport by Interfacial Forces," *Annual Review of Fluid Mechanics*, vol. 21, p. 61 99, 1989.

[69] R. A. Rica and M. Z. Bazant, "Electrodiffusiophoresis: Particle motion in electrolytes under direct current," *Physics of Fluids*, vol. 22, p. 112109, 2010.

[70] E. Yariv, "Communication: The phoretic drift of a charged particle animated by a direct ionic current.," *The Journal of Chemical Physics*, vol. 133, p. 121102, 2010.

[71] Z. R. Ulberg and A. S. Dukhin, "Electrodiffusiophoresis - film formation in ac and dc electrical fields and its application for bactericidal coatings," *Progress in Organic Coatings*, vol. 18, no. 1, pp. 1–41, 1990.

[72] V. Tricoli and G. Orsini, "Electrodiffusiophoresis of a large-zeta-potential particle in weak fields," *Journal of Physics: Condensed Matter*, vol. 27, p. 415102, 2015.

[73] C. D. Davies, E. Yoon, and R. M. Crooks, "Continuous Redirection and Separation of Microbeads by Faradaic Ion Concentration Polarization," *ChemElectroChem*, vol. 5, no. 6, pp. 877–884, 2018.

[74] J. Yoon, Y. Cho, J. H. Lee, and S. Chung, "Tunable sheathless microfluidic focusing using ion concentration polarization," *Applied Physics Letters*, vol. 107, no. 8, p. 083507, 2015.

[75] N. Cevheri and M. Yoda, "Electrokinetically driven reversible banding of colloidal particles near the wall," *Lab on a Chip*, vol. 14, no. 8, pp. 1391–1394, 2014.

[76] H. Jeon, H. Lee, K. H. Kang, and G. Lim, "Ion concentration polarization-based continuous separation device using electrical repulsion in the depletion region," *Scientific Reports*, vol. 3, no. 1, p. 3483, 2013.

[77] C. D. Davies and R. M. Crooks, "Focusing, sorting, and separating microplastics by serial faradaic ion concentration polarization," *Chemical Science*, vol. 11, no. 21, pp. 5547–5558, 2020.

[78] M. M. Gong, R. Nosrati, M. C. S. Gabriel, A. Zini, and D. Sinton, "Direct DNA Analysis with Paper-Based Ion Concentration Polarization," *Journal of the American Chemical Society*, vol. 137, no. 43, pp. 13913–13919, 2015.

[79] Z.-Y. Wu, B. Ma, S.-F. Xie, K. Liu, and F. Fang, "Simultaneous electrokinetic concentration and separation of proteins on a paper-based analytical device," *RSC Advances*, vol. 7, no. 7, pp. 4011–4016, 2017.

[80] S. Gangwal, O. J. Cayre, M. Z. Bazant, and O. D. Velev, "Induced-Charge Electrophoresis of Metallodielectric Particles," *Physical Review Letters*, vol. 100, p. 058302, 2008.

[81] F. Ma, X. Yang, H. Zhao, and N. Wu, "Inducing Propulsion of Colloidal Dimers by Breaking the Symmetry in Electrohydrodynamic Flow," *Physical Review Letters*, vol. 115, no. 20, p. 208302, 2015.

[82] A. M. Boymelgreen, T. Balli, T. Miloh, and G. Yossifon, "Active colloids as mobile microelectrodes for unified label-free selective cargo transport," *Nature Communications*, vol. 9, no. 1, p. 760, 2018.

[83] J. Yan, M. Han, J. Zhang, C. Xu, E. Luijten, and S. Granick, "Reconfiguring active particles by electrostatic imbalance," *Nature Materials*, vol. 15, no. 10, pp. 1095–1099, 2016.

[84] A. A. Shah, H. Kang, K. L. Kohlstedt, K. H. Ahn, S. C. Glotzer, C. W. Monroe, and M. J. Solomon, "Liquid crystal order in colloidal suspensions of spheroidal particles by direct current electric field assembly.," *Small*, vol. 8, pp. 1551 – 1562, 05 2012.

[85] U. M. Córdova-Figueroa and J. F. Brady, "Osmotic propulsion: The osmotic motor," *Physical Review Letters*, vol. 100, p. 158303, 2008.

[86] J. R. Howse, R. A. L. Jones, A. J. Ryan, T. Gough, R. Vafabakhsh, and R. Golestanian, "Self-Motile Colloidal Particles: From Directed Propulsion to Random Walk," *Physical Review Letters*, vol. 99, no. 4, p. 048102, 2007.

[87] A. Aubret, M. Youssef, S. Sacanna, and J. Palacci, "Targeted assembly and synchronization of self-spinning microgears," *Nature Physics*, vol. 14, no. 11, pp. 1114–1118, 2018.

[88] A. Aubret and J. Palacci, "Diffusiophoretic design of self-spinning microgears from colloidal microswimmers," *Soft Matter*, vol. 14, pp. 9577–9588, 2018.

[89] F. Ginot, I. Theurkauff, F. Detcheverry, C. Ybert, and C. Cottin-Bizonne, "Aggregation-fragmentation and individual dynamics of active clusters," *Nature Communications*, vol. 9, no. 1, p. 696, 2018.

[90] C. P. Goodrich and M. P. Brenner, "Using active colloids as machines to weave and braid on the micrometer scale," *Proceedings of the National Academy of Sciences*, vol. 114, no. 2, pp. 257 – 262, 2017.

[91] A. Straub, A. Deshmukh, and M. Elimelech, "Pressure-retarded osmosis for power generation from salinity gradients: is it viable?," *Energy & Environmental Science*, vol. 9, pp. 31–48, 2016.

[92] S. Shin, O. Shardt, P. B. Warren, and H. A. Stone, "Membraneless water filtration using CO2," *Nature Communications*, vol. 8, p. ncomms15181, 2017.

[93] B. Abécassis, C. Cottin-Bizonne, C. Ybert, A. Ajdari, and L. Bocquet, "Boosting migration of large particles by solute contrasts," *Nature Materials*, vol. 7, no. 10, pp. 785–789, 2008.

[94] A. Joseph, C. Contini, D. Cecchin, S. Nyberg, L. Ruiz-Perez, J. Gaitzsch, G. Fullstone, X. Tian, J. Azizi, J. Preston, G. Volpe, and G. Battaglia, "Chemotactic synthetic vesicles: Design and applications in blood-brain barrier crossing.," *Science advances*, vol. 3, no. 8, p. e1700362, 2017.

[95] S. Shin, E. Um, B. Sabass, J. T. Ault, M. Rahimi, P. B. Warren, and H. A. Stone, "Size-dependent control of colloid transport via solute gradients in dead-end channels," *Proceedings of the National Academy of Sciences*, vol. 113, pp. 257–261, 2016.

[96] A. Kar, T.-Y. Chiang, I. O. Rivera, A. Sen, and D. Velegol, "Enhanced transport into and out of dead-end pores.," *ACS Nano*, vol. 9, pp. 746–53, 2015.

[97] C. Monast, C. Furcht, and M. Lazzara, "Computational Analysis of the Regulation of EGFR by Protein Tyrosine Phosphatases," *Biophysical journal*, vol. 102, pp. 2012–21, 2012.

[98] I. Pinilla-Macua, S. C. Watkins, and A. Sorkin, "Endocytosis separates EGF receptors from endogenous fluorescently labeled HRas and diminishes receptor signaling to MAP kinases in endosomes," *Proceedings of the National Academy of Sciences*, vol. 113, pp. 2122–2127, 2016.

[99] T. Danino, O. Mondragón-Palomino, L. Tsimring, and J. Hasty, "A synchronized quorum of genetic clocks," *Nature*, vol. 463, p. 326, 2010.

[100] S. Basu, Y. Gerchman, C. H. Collins, F. H. Arnold, and R. Weiss, "A synthetic multicellular system for programmed pattern formation," *Nature*, vol. 434, p. 1130, 2005.

[101] T. Doneux, L. Bouffier, B. Goudeau, and S. Arbault, "Coupling Electrochemistry with Fluorescence Confocal Microscopy To Investigate Electrochemical Reactivity: A Case Study with the Resazurin-Resorufin Fluorogenic Couple," *Analytical Chemistry*, vol. 88, pp. 6292 – 6300, 06 2016.

[102] F. Miomandre, E. Lépicier, S. Munteanu, O. Galangau, J. F. Audibert, R. Méallet-Renault, P. Audebert, and R. B. Pansu, "Electrochemical Monitoring of the Fluorescence Emission of Tetrazine and Bodipy Dyes Using Total Internal Reflection Fluorescence Microscopy Coupled to Electrochemistry," *ACS Applied Materials & Interfaces*, vol. 3, pp. 690 – 696, 03 2011.

[103] N. C. Rudd, S. Cannan, E. Bitziou, I. Ciani, A. L. Whitworth, and P. R. Unwin, "Fluorescence Confocal Laser Scanning Microscopy as a Probe of pH Gradients in Electrode Reactions and Surface Activity," *Analytical Chemistry*, vol. 77, no. 19, pp. 6205 – 6217, 2005-10.

[104] A. J. Leenheer and H. A. Atwater, "Imaging Water-Splitting Electrocatalysts with pH-Sensing Confocal Fluorescence Microscopy," *Journal of The Electrochemical Society*, vol. 159, no. 9, pp. H752–H757, 2012.

[105] B. Fuladpanjeh-Hojaghan, M. M. Elsutohy, V. Kabanov, B. Heyne, M. Trifkovic, and E. P. L. Roberts, "In-Operando Mapping of pH Distribution in Electrochemical Processes," *Angewandte Chemie*, vol. 131, no. 47, pp. 16971–16975, 2019.

[106] T. López-León, A. B. Jódar-Reyes, D. Bastos-González, and J. L. Ortega-Vinuesa, "Hofmeister Effects in the Stability and Electrophoretic Mobility of Polystyrene Latex Particles," *The Journal of Physical Chemistry B*, vol. 107, no. 24, pp. 5696 – 5708, 2003.

[107] N. C. Rudd, S. Cannan, E. Bitziou, I. Ciani, A. L. Whitworth, and P. R. Unwin, "Fluorescence confocal laser scanning microscopy as a probe of ph gradients in electrode reactions and surface activity," *Analytical chemistry*, vol. 77, no. 19, pp. 6205–6217, 2005.

[108] J. Suzurikawa, M. Nakao, R. Kanzaki, and H. Takahashi, "Microscale ph gradient generation by electrolysis on a light-addressable planar electrode," *Sensors and Actuators B: Chemical*, vol. 149, no. 1, pp. 205–211, 2010.

[109] K. Obata, R. Van De Krol, M. Schwarze, R. Schomäcker, and F. F. Abdi, "In situ observation of ph change during water splitting in neutral ph conditions: impact of natural convection driven by buoyancy effects," *Energy & Environmental Science*, vol. 13, no. 12, pp. 5104–5116, 2020.

[110] T. Jones, *Electromechanics of Particles*. Cambridge, UK: Cambridge University Press, 2005.

[111] V. Murtsovkin, "Nonlinear flows near polarized disperse particles," *Colloid Journal*, vol. 58, pp. 341–349, MAY-JUN 1996.

[112] A. A. Harraq, B. D. Choudhury, and B. Bharti, "Field-Induced Assembly and Propulsion of Colloids," *Langmuir*, vol. 38, no. 10, pp. 3001–3016, 2022.

[113] T. M. Squires and M. Z. Bazant, "Breaking symmetries in induced-charge electro-osmosis and electrophoresis," *Journal of Fluid Mechanics*, vol. 560, pp. 65–101, 2006.

[114] T. Salafi, K. K. Zeming, and Y. Zhang, "Advancements in microfluidics for nanoparticle separation," *Lab on a Chip*, vol. 17, no. 1, pp. 11–33, 2016.

[115] Y. Wang, L. Zhao, Y. Zhao, W. Y. Wang, Y. Liu, C. Gu, J. Li, G. Zhang, T. J. Huang, and S. Yang, "Electrocarving during Electrodeposition Growth," *Advanced Materials*, vol. 30, no. 51, p. 1870395, 2018.

[116] J. R. Maestas, F. Ma, N. Wu, and D. T. Wu, "Electric-Field-Driven Assembly of Dipolar Spheres Asymmetrically Confined between Two Electrodes," *ACS Nano*, vol. 15, no. 2, pp. 2399–2412, 2021. This paper by Ning Wu shows the rich behavior of simple colloids under electric fields. In this case, particles form many different phases in 2D lattices.

[117] J. J. Crassous, A. M. Mihut, E. Wernersson, P. Pfleiderer, J. Vermant, P. Linse, and P. Schurtenberger, "Field-induced assembly of colloidal ellipsoids into well-defined microtubules," *Nature Communications*, vol. 5, no. 1, p. 5516, 2014.

[118] J. Zhang, J. Yang, Y. Zhang, and M. A. Bevan, "Controlling colloidal crystals via morphing energy landscapes and reinforcement learning," *Science Advances*, vol. 6, no. 48, p. eabd6716, 2020.

[119] Z. Wang, Z. Wang, J. Li, C. Tian, and Y. Wang, "Active colloidal molecules assembled via selective and directional bonds," *Nature Communications*, vol. 11, no. 1, p. 2670, 2020.

[120] F. Ma, S. Wang, D. T. Wu, and N. Wu, "Electric-field-induced assembly and propulsion of chiral colloidal clusters.," *Proceedings of the National Academy of Sciences*, vol. 112, no. 20, pp. 6307–6312, 2015.

[121] J. G. Lee, A. M. Brooks, W. A. Shelton, K. J. M. Bishop, and B. Bharti, "Directed propulsion of spherical particles along three dimensional helical trajectories," *Nature Communications*, vol. 10, pp. 31 – 8, 06 2019.

[122] Y. Wu, A. Fu, and G. Yossifon, "Active particles as mobile microelectrodes for selective bacteria electroporation and transport," *Science Advances*, vol. 6, no. 5, p. eaay4412, 2020.

[123] P. J. Beltramo, D. Schneider, G. Fytas, and E. M. Furst, "Anisotropic Hypersonic Phonon Propagation in Films of Aligned Ellipsoids," *Physical Review Letters*, vol. 113, p. 205503, 11 2014.

[124] X. Tang, B. Rupp, Y. Yang, T. D. Edwards, M. A. Grover, and M. A. Bevan, "Optimal Feedback Controlled Assembly of Perfect Crystals," *ACS Nano*, vol. 10, no. 7, pp. 6791–6798, 2016.

[125] T. D. Edwards, Y. Yang, D. J. Beltran-Villegas, and M. A. Bevan, "Colloidal crystal grain boundary formation and motion," *Scientific Reports*, vol. 4, p. 6132, 08 2014.

[126] Z. M. Sherman and J. W. Swan, "Dynamic, Directed Self-Assembly of Nanoparticles viaToggled Interactions," *ACS Nano*, vol. 10, no. 5, pp. 5260–5271, 2016.

[127] Z. M. Sherman and J. W. Swan, "Transmutable Colloidal Crystals and Active Phase Separation via Dynamic, Directed Self-Assembly with Toggled External Fields," *ACS Nano*, vol. 13, no. 1, pp. 764–771, 2018.

[128] P.-K. Kao, B. J. VanSaders, M. D. Durkin, S. C. Glotzer, and M. J. Solomon, "Anisotropy effects on the kinetics of colloidal crystallization and melting: comparison of spheres and ellipsoids.," *Soft matter*, vol. 15, no. 37, pp. 7479–7489, 2019.

[129] W. D. Ristenpart, I. A. Aksay, and D. A. Saville, "Electrohydrodynamic flow around a colloidal particle near an electrode with an oscillating potential," *Journal of Fluid Mechanics*, vol. 575, pp. 83 – 109, 03 2007.

[130] C. L. Wirth, R. M. Rock, P. J. Sides, and D. C. Prieve, "Single and pairwise motion of particles near an ideally polarizable electrode.," *Langmuir*, vol. 27, pp. 9781 – 9791, 08 2011.

[131] C. L. Wirth, P. J. Sides, and D. C. Prieve, "Electrolyte dependence of particle motion near an electrode during ac polarization," *Physical Review E*, vol. 87, no. 3, p. 254, 2013.

[132] R. An, K. Massa, D. O. Wipf, and A. R. Minerick, "Solution pH change in non-uniform alternating current electric fields at frequencies above the electrode charging frequency," *Biomicrofluidics*, vol. 8, no. 6, p. 064126, 2014.

[133] W. Y. Ng, Y. C. Lam, and I. Rodríguez, "Experimental verification of Faradaic charging in ac electrokinetics," *Biomicrofluidics*, vol. 3, no. 2, p. 022405, 2009.

[134] M. Rath, J. Weaver, M. Wang, and T. Woehl, "pH-Mediated Aggregation-to-Separation Transition for Colloids Near Electrodes in Oscillatory Electric Fields," *Langmuir*, vol. 37, no. 31, pp. 9346–9355, 2021.

[135] S. M. H. H. Amrei, S. C. Bukosky, S. P. Rader, W. D. Ristenpart, and G. H. Miller, "Oscillating Electric Fields in Liquids Create a Long-Range Steady Field," *Physical Review Letters*, vol. 121, p. 185504, 11 2018.

[136] S. M. H. H. Amrei, G. H. Miller, K. J. M. Bishop, and W. D. Ristenpart, "A perturbation solution to the full Poisson–Nernst–Planck equations yields an asymmetric rectified electric field," *Soft Matter*, vol. 16, no. 30, pp. 7052–7062, 2020.

[137] V. S. Doan and S. Shin, "Formation of a colloidal band via pH-dependent electrokinetics," *ELECTROPHORESIS*, vol. 42, no. 21-22, pp. 2356–2364, 2021.

[138] K. Wang, B. Behdani, and C. A. Silvera Batista, "Visualization of Concentration Gradients and Colloidal Dynamics under Electrodiffusiophoresis," *Langmuir*, vol. 38, no. 18, pp. 5663–5673, 2022.

[139] E. S. Malkin and A. S. Dukhin, "Deposition of Colloidal Particles on an Electrode in an Alternating Electric-Field," *Colloid Journal of the USSR*, vol. 42, no. 3, pp. 396 – 401, 1982.

[140] E. S. Malkin and A. S. Dukhin, "Aperiodic Electrodiffusiophoresis," *Colloid Journal of the USSR*, vol. 44, no. 2, pp. 225 – 233, 1982.

[141] E. S. Malkin and A. S. Dukhin, "Microscopic Investigation of the Aperiodic Electrodiffusiophoresis," *Kolloidnyi Zhurnal*, vol. 44, no. 3, pp. 523 – 528, 1982.

[142] K. Obata, R. v. d. Krol, M. Schwarze, R. Schomäcker, and F. F. Abdi, "In situ observation of pH change during water splitting in neutral pH conditions: impact of natural convection driven by buoyancy effects," *Energy & Environmental Science*, vol. 13, no. 12, pp. 5104–5116, 2020.

[143] T. M. Żurawik, A. Pomorski, A. Belczyk-Ciesielska, G. Goch, K. Niedźwiedzka, R. Kucharczyk, A. Krężel, and W. Bal, "Revisiting mitochondrial ph with an improved algorithm for calibration of the ratiometric 5 (6)-carboxy-snarf-1 probe reveals anticooperative reaction with h+ ions and warrants further studies of organellar ph," *PloS one*, vol. 11, no. 8, p. e0161353, 2016.

[144] J. A. Fagan, Sides, and Paul J, and D. C. Prieve, "Vertical Motion of a Charged Colloidal Particle near an AC Polarized Electrode with a Nonuniform Potential Distribution: Theory and Experimental Evidence," *Langmuir*, vol. 20, pp. 4823 – 4834, 05 2004.

[145] N. Shi, R. Nery-Azevedo, A. I. Abdel-Fattah, and T. M. Squires, "Diffusiophoretic Focusing of Suspended Colloids," *Physical Review Letters*, vol. 117, p. 258001, 12 2016.

[146] J. A. Ferrar and M. J. Solomon, "Kinetics of colloidal deposition, assembly, and crystallization in steady electric fields," *Soft Matter*, vol. 11, pp. 3599–3611, 2015.

[147] K. E. Davis, W. B. Russel, and W. J. Glantschnig, "Settling suspensions of colloidal silica: observations and X-ray measurements," *Journal of the Chemical Society, Faraday Transactions*, vol. 87, no. 3, pp. 411–424, 1991.

[148] K. E. Davis and W. B. Russel, "An asymptotic description of transient settling and ultrafiltration of colloidal dispersions," *Physics of Fluids A: Fluid Dynamics*, vol. 1, no. 1, pp. 82–100, 1989.

[149] B. G. Prevo and O. D. Velev, "Controlled, Rapid Deposition of Structured Coatings from Micro- and Nanoparticle Suspensions," *Langmuir*, vol. 20, no. 6, pp. 2099–2107, 2004.

[150] J. D. Forster, J.-G. Park, M. Mittal, H. Noh, C. F. Schreck, C. S. O'Hern, H. Cao, E. M. Furst, and E. R. Dufresne, "Assembly of Optical-Scale Dumbbells into Dense Photonic Crystals," *ACS Nano*, vol. 5, pp. 6695 – 6700, 08 2011.

[151] J. Zhang, Y. Zhang, and M. A. Bevan, "Spatially varying colloidal phase behavior on multi-dimensional energy landscapes," *The Journal of Chemical Physics*, vol. 152, no. 5, p. 054905, 2020.

[152] J. J. Juárez, S. E. Feicht, and M. A. Bevan, "Electric field mediated assembly of three dimensional equilibrium colloidal crystals," *Soft Matter*, vol. 8, no. 1, pp. 94–103, 2012.

[153] P. N. Pusey and W. v. Megen, "Phase behaviour of concentrated suspensions of nearly hard colloidal spheres," *Nature*, vol. 320, pp. 340 – 342, 03 1986.

[154] P. N. Pusey, W. v. Megen, P. Bartlett, B. J. Ackerson, J. G. Rarity, and S. M. Underwood, "Structure of crystals of hard colloidal spheres," *Physical Review Letters*, vol. 63, pp. 2753 – 2756, 12 1989.

[155] R. W. O'Brien and L. R. White, "Electrophoretic mobility of a spherical colloidal particle," *Journal of the Chemical Society, Faraday Transactions 2: Molecular and Chemical Physics*, vol. 74, pp. 1607–1626, 1978.

[156] J. P. Ebel, J. L. Anderson, and D. C. Prieve, "Diffusiophoresis of latex particles in electrolyte gradients," *Langmuir*, vol. 4, pp. 396–406, 1988.

[157] P. O. Staffeld and J. A. Quinn, "Diffusion-induced banding of colloid particles via diffusiophoresis 1. Electrolytes," *Journal of Colloid and Interface Science*, vol. 130, pp. 69–87, 1989.

[158] P. B. Warren, "Non-Faradaic Electric Currents in the Nernst-Planck Equations and Nonlocal Diffusiophoresis of Suspended Colloids in Crossed Salt Gradients.," *Physical review letters*, vol. 124, no. 24, p. 248004, 2020.

[159] C.-Y. Lin, P.-H. Wong, P.-H. Wang, Z. S. Siwy, and L.-H. Yeh, "Electrodiffusioosmosis-induced negative differential resistance in ph-regulated mesopores containing purely monovalent solutions," *ACS Applied Materials & Interfaces*, vol. 12, no. 2, pp. 3198–3204, 2020. PMID: 31846283.

[160] S. E. Yalcin, S. Y. Lee, S. W. Joo, O. Baysal, and S. Qian, "Electrodiffusiophoretic Motion of a Charged Spherical Particle in a Nanopore," *The Journal of Physical Chemistry B*, vol. 114, no. 11, pp. 4082–4093, 2010.

[161] K. Wang, S. Leville, B. Behdani, and C. A. Silvera Batista, "Long-range transport and directed assembly of charged colloids under aperiodic electrodiffusiophoresis.," *Soft matter*, vol. 18, no. 32, pp. 5949–5959, 2022.

[162] J. A. Fagan, Sides, and Paul J, and D. C. Prieve, "Vertical Oscillatory Motion of a Single Colloidal Particle Adjacent to an Electrode in an ac Electric Field," *Langmuir*, vol. 18, pp. 7810 – 7820, 09 2002.

[163] B. Rupp, I. Torres-Díaz, X. Hua, and M. A. Bevan, "Measurement of Anisotropic Particle Interactions with Nonuniform ac Electric Fields," *Langmuir*, vol. 34, pp. 2497 – 2504, 02 2018.

[164] P. Attard, *Thermodynamics and Statistical Mechanics*. Amsterdam: Academic Press, 2002.

[165] J.-P. Hansen and I. R. McDonald, *Theory of simple liquids: with applications to soft matter*. Academic press, 2013.

[166] J. D. Hoggard, P. J. Sides, and D. C. Prieve, "Electrolyte-Dependent Pairwise Particle Motion near Electrodes at Frequencies below 1 kHz," *Langmuir*, vol. 23, no. 13, pp. 6983 – 6990, 2007.

[167] C. S. Dutcher, T. J. Woehl, N. H. Talken, and W. D. Ristenpart, "Hexatic-to-Disorder Transition in Colloidal Crystals Near Electrodes: Rapid Annealing of Polycrystalline Domains," *Physical Review Letters*, vol. 111, no. 12, 2013.

[168] X. Yang, S. Johnson, and N. Wu, "The Impact of Stern-Layer Conductivity on the Electrohydrodynamic Flow Around Colloidal Motors under an Alternating Current Electric Field," *Advanced Intelligent Systems*, vol. 1, no. 8, p. 1900096, 2019.

[169] W. D. Ristenpart, I. A. Aksay, and D. A. Saville, "Assembly of colloidal aggregates by electrohydrodynamic flow: Kinetic experiments and scaling analysis," *Physical Review E*, vol. 69, p. 021405, 02 2004.

[170] J. Suzurikawa, M. Nakao, R. Kanzaki, and H. Takahashi, "Microscale pH gradient generation by electrolysis on a light-addressable planar electrode," *Sensors and Actuators B: Chemical*, vol. 149, no. 1, pp. 205–211, 2010.

[171] R. Welden, M. J. Schöning, P. H. Wagner, and T. Wagner, "Light-addressable Electrodes for Dynamic and Flexible Addressing of Biological Systems and Electrochemical Reactions," *Sensors*, vol. 20, no. 6, p. 1680, 2020.

[172] R. Welden, C. Gottschalk, I. Madarevic, M. J. V. Bael, H. Iken, J. Schubert, M. J. Schöning, P. H. Wagner, and T. Wagner, "Formation of controllable pH gradients inside microchannels by using light-addressable electrodes," *Sensors and Actuators B: Chemical*, vol. 346, p. 130422, 2021.